Advanced Signal and Receiver Design for Next Generation OFDM Systems

Stefano Rosati

March 15, 2011

Alma Mater Studiorum - University of Bologna

DEIS - DEPARTMENT OF ELECTRONICS, COMPUTER SCIENCE AND SYSTEMS

PHD COURSE IN ELECTRONICS, COMPUTER SCIENCE AND TELECOMMUNICATIONS

XXIII Cycle ING-INF/03

Advanced signal and receiver design for next generation OFDM systems

Candidate:
Stefano Rosati

Supervisor:
Prof. **Giovanni Emanuele Corazza**

PhD Course Coordinator:
Prof. **Paola Mello**

Advisor:
Prof. **Alessandro Vanelli-Coralli**

March 2011

This page intentionally contains only this sentence.

This page intentionally contains only this sentence.

A Sara, Antonietta e Gigi

This page intentionally contains only this sentence.

Gutta cavat lapidem.
A drop of water hollows a stone.

This page intentionally contains only this sentence.

Acknowledgments

This thesis is the outcome of three years of hard work, deep and enthusiastic love for my job, research and innovation. It is also the outcome of the collaboration, the support, and the help of many teachers, colleagues, and friends which I had the privilege to meet during this adventure. I would never have accomplished writing this thesis as you can read it today just on my own. How can I find the appropriate way to thank all the people who have given their contribution to this thesis as well as to my personal and profession growth? I know, it is almost impossible. I will try anyway even though and I am pretty sure it is not going to be enough.

First of all, I thank my family: **Sara**, **Antonietta**, and **Gigi**, to whom this thesis is dedicated, for their uncountable support and their infinite Love.

I would like to express my deepest and most sincere gratefulness to my Professor, Supervisor, and Friend Prof. **Giovanni Emanuele Corazza** for his inspiring and far-sighted guidance during the course of my studies. As my Father did before, Giovanni taught me the importance of working really hard to reach my goals. He guided my wild and unconscious creativity and scientific curiosity, giving me the tools n' rules to think, create, and innovate in a effective way. *He lit up a candle and he showed me the way*. Giovanni is also a terrific leader, the best leader I ever met. I want to thank him for having created the **Amazing Digicomm Group** and for having given me the opportunity to be part of it. In a few words, Giovanni is and will be for me the best example to follow in my professional and personal life. I like to spend some special words to thank my advisor Prof. **Alessandro Vanelli-Coralli**. His precious advices have been crucial for my personal and professional growth. In these years, I have tried to capture and store every single technical tip and pearl of wisdom given out by Alessandro. Giovanni and Alessandro have been, and are for me much more than teachers. I will be forever grateful to them.

Special thanks to my awesome colleagues at the Digicomm group, for their friendship and their support. In particular I would like to thank my Ph.D. fel-

lows: **Enzo Alberto *Can Drive* Candreva**, **Claudio *The Boss* Palestini**, and **Marco Papaleo**. They shared with me this amazing adventure. I will never forget the long afternoons passed in our open space discussing about technical and not-so-technical things, as well as the great trips around the world. *Now guys, let's conquer the world!* I also thank all the Digicomm Seniors: **Stefano Cioni**, **Rosario Firincelli**, **Massimo *Max* Neri**, **Raffaelle *Lella* Pedone**, and last but not least **Marco Villanti**, for their precious suggestions and for sharing their experience. Many thanks to my past colleagues and the new Digicommers: **Ricardo Baroni**, **Cecilia *Ceci* Bersani**, **Francesco *Chicco* Bastia**, **Lina *Coinquilina* Deambrogio**, **Giulio G^2 Gabelli**, **Alessandro Guidotti**, **Francesco Lombardo**, **Valeria Petrini**, **Valentina Pullano**, **Rosalba Suffritti**, **Daniele Tarchi**, and **Ilaria Thibault**. Actually Lina deserves a double thanks for help me in the proof reading of the thesis. It was great to work with all you guys! Keep rocking!

I would like to thank **Juan Montojo** and **Peter Gaal** for hosting me in Qualcomm. They helped me to be part and to give my contribute in such a great company. In Qualcomm I have learnt much more than equations and telecommunication standards, I have learnt the Qualcomm's attitude: *What if...* A special thanks goes to **Stefan Geirhofer** for unveiling all the secrets of system level evaluations. It was a great fortune for me to work everyday, shoulder to shoulder, with such a great engineer as Stefan. Many thanks to all the guys in the **LTE MIMO Group** in Qualcomm! It was great pleasure to meet and to work with all of you! A great thanks goes to my colleagues, office mates, and friends in San Diego: **Alan Barbieri**, **Amin Jafarian**, **Simone Merlin**, **Roberto Rimini**, and **Sheng Yi**; for their friendship. We had a very good time over there in La Jolla. It was great to hang out with you guys! I hope to see you soon!

Finally, I want to thank the city of **Bologna**, which adopted me as a foster son. I had a tremendous time in Bologna. This city has been my home for almost ten years, and it was the witness and the accomplice of my growth. In a few weeks from now I will leave towards new and fascinating adventures, but I will never forget this place.

So guys, wherever you are, let's have a drink on me!

Stefano

TABLE OF CONTENTS

Acknowledgments **ix**

List of Figures **xv**

List of Tables **xix**

Acronyms **xxi**

Original Contributions **xxv**

Introduction **1**

1 OFDM Principles **5**
1.1 Why Parallel is Smarter Than Serial 6
1.2 Orthogonality 7
1.3 Using the Fast Fourier Transform 9
1.4 Guard Interval and Cyclic Prefix 10
1.5 Basic system model 13

2 Nonlinear Distortion: Analysis and Countermeasures **17**
2.1 Nonlinear Distortion Analysis 19
2.1.1 HPA Modelling 20
2.1.2 Memoryless HPA Models 21
2.1.2.1 Ideal Clipping 22
2.1.2.2 Saleh Model 23
2.1.2.3 Rapp Model 23
2.1.3 Effects of Nonlinear Distortion on the OFDM Signal 25

2.2 Countermeasures to Nonlinear Distortion . . . 27
2.2.1 Predistortion . . . 27
2.2.2 PAPR Reduction . . . 27
2.2.2.1 Active Constellation Extension . . . 27
2.2.2.2 Tone Reservation . . . 28
2.2.2.3 Selected Mapping . . . 29
2.2.2.4 Quasi-Constant Envelope OFDM . . . 29
2.3 Rotation-Invariant Subcarrier Mapping . . . 30
2.3.1 RISM Mapping Schemes . . . 30
2.3.1.1 Two-Level RISM Mapping . . . 30
2.3.1.2 Four-Level RISM Mapping . . . 31
2.3.2 RISM Iterative Optimization . . . 32
2.3.3 RISM Detectors . . . 35
2.3.4 Hybrid RISM . . . 36
2.3.4.1 Practical Case: RISM over DVB-T2 Reserved Tones . 37
2.4 Numerical Results . . . 39
2.4.1 PAPR Reduction Performance . . . 39
2.4.2 Bit Error Rate over Nonlinear Channels . . . 40
2.4.3 Total Degradation . . . 41
2.4.3.1 A further thought about TD in OFDM systems . . . 46

3 Time and Frequency Synchronization 57
3.1 Effects of time and frequency offsets and phase noise . . . 58
3.2 OFDM Synchronization strategy . . . 61
3.3 PRE-FFT Synchronization . . . 62
3.3.1 Existing algorithms for CTE and FFE . . . 62
3.3.2 Low-complexity PRE-FFT algorithms . . . 64
3.3.3 EEWS algorithm . . . 64
3.3.4 EEWS Optimization . . . 65
3.3.5 Complexity and Performance Comparison . . . 67
3.3.6 Considerations . . . 72
3.3.7 Preamble based PRE-FFT Synchronization . . . 72
3.4 POST-FFT Synchronization . . . 73
3.4.1 Pilot Pattern Design . . . 74
3.4.2 Detector Definitions . . . 78
3.4.2.1 Silent Detector . . . 78

3.4.2.1.1 Analytical Analysis 79
3.4.2.2 Differential Detector 80
3.4.3 Performance Comparison 80
3.4.4 Considerations 82

4 Channel Estimation **83**
4.1 Existing Channel Estimation Methods 84
4.1.1 LS Channel Estimation 84
4.2 Most Significant Samples Selection 87
4.3 MSE Lower Bounds 88
4.4 Novel Algorithms 94
4.4.1 Threshold Crossing Selection 94
4.4.1.1 TCS MSE: Analytical Expression 95
4.4.1.2 Sub-Optimal Threshold 96
4.4.2 Energy-based MSS Selection Strategies 97
4.4.2.1 Instantaneous Energy Selection 97
4.4.2.2 Average Energy Selection 97
4.5 Numerical Results and Discussions 101
4.5.1 MSE performance 102
4.5.2 BER performance 105

5 SC-FDMA in Broadband Satellite Return Channel **113**
5.1 SC-FDMA in Return Satellite Channel 114
5.1.1 SC-FDMA System Model 115
5.2 Joint Multi-User Estimation 118
5.2.1 Pilot Pattern 118
5.2.2 Timing Offset Estimation 119
5.2.3 CPE Estimation 119
5.3 Numerical Results 121

Bibliography **127**

This page intentionally contains only this sentence.

List of Figures

1.1 Block diagram of a generic multicarrier transmitter. 10
1.2 PSD of a OFDM signal with $N = 8$ subcarriers. 11
1.3 Block diagram OFDM transmitter using Discrete Fourier Transform. 11
1.4 Cyclic Prefix. 12
1.5 OFDM signal over time dispersive channel. 12

2.1 PAPR CCDF for several values of subcarriers number, N 18
2.2 Saleh Model 24
2.3 Rapp model: AM/AM characteristic for several values of p 25
2.4 Output Back-Off as a function of the Input Back-Off considering a complex Gaussian input signal. 26
2.5 2-level RISM Mapping. 31
2.6 4-level RISM Mapping. 32
2.7 Block Diagram of the RISM Iterative Optimization 33
2.8 Block Diagram of the Low-Complex RISM Iterative Optimization . . 34
2.9 Decision regions for 2-level RISM. 36
2.10 Decision Regions for 4-level Mapping. 37
2.11 BER Performance in linear channel 38
2.12 PAPR performance for 2-level RISM using different clip level values. 40
2.13 PAPR performance for 4-level RISM using different clip level values. 41
2.14 PAPR Comparison between OFDM-QPSK, 2-level and 4-level RISM. 42
2.15 PAPR performance for 2-level Hybrid-RISM for different values of the RISM tone density. 43

2.16 PAPR performance for 4-level Hybrid-RISM for different values of the RISM tone density. 44
2.17 BER Performance using Saleh model with IBO $= 0\ dB$. 45
2.18 BER Performance in case of Ideal Clipping IBO $= 0\ dB$. 46
2.19 Total degradation performance using Saleh model. 47
2.20 Signal-to-Distortion Ratio using Hybrid RISM for different values of the RISM tone density, with Ideal Clipping HPA model. 49
2.21 Signal-to-Distortion Ratio using Hybrid RISM for different values of the RISM tone density, with Rapp HPA model. 49
2.22 Signal-to-Distortion Ratio using Hybrid RISM for different values of the RISM tone density, with Saleh HPA model. 50
2.23 δ_{SNR}, The power boosting needed to compensate the effect of the nonlinear distortion with IC HPA model, $SNR_{req} = 8$ dB. 50
2.24 δ_{SNR}, The power boosting needed to compensate the effect of the nonlinear distortion with Saleh HPA model, $SNR_{req} = 8$ dB. 51
2.25 Hybrid RISM Total Degradation performance using Ideal Clipping model, $SNR_{req} = 0$ dB. 51
2.26 Hybrid RISM Total Degradation performance using Rapp model, $SNR_{req} = 0$ dB. 52
2.27 Hybrid RISM Total Degradation performance using Saleh model, $SNR_{req} = 0$ dB. 52
2.28 Hybrid RISM Total Degradation performance using Ideal Clipping model, $SNR_{req} = 4$ dB. 53
2.29 Hybrid RISM Total Degradation performance using Rapp model, $SNR_{req} = 4$ dB. 53
2.30 Hybrid RISM Total Degradation performance using Saleh model, $SNR_{req} = 4$ dB. 54
2.31 Hybrid RISM Total Degradation performance using Ideal Clipping model, $SNR_{req} = 8$ dB. 54
2.32 Hybrid RISM Total Degradation performance using Rapp model, $SNR_{req} = 8$ dB. 55
2.33 Hybrid RISM Total Degradation performance using Saleh model, $SNR_{req} = 8$ dB. 55

3.1 DVB-RCS Phase Noise Mask 59
3.2 Generic synchronization steps for OFDM systems. 61

3.3 Block diagram of the proposed EEWS algorithm. 65
3.4 Several shapes of EWS weighting windows for different values of M. 66
3.5 The plot of $\Upsilon(M,0) - \Upsilon(M,-1)$ and $\Upsilon(M,0) - \Upsilon(M,1)$ as a function of M, with several N_g values. 68
3.6 CTE error standard deviation, using DVB-SH 4K, $T_g = T_u/4, QPSK$ 70
3.7 FFE error standard deviation, using DVB-SH 4K, $T_g = T_u/4, QPSK$. 71
3.8 Overlapping position function of DVB pattern illustrated in 3.4(a) . . 77
3.9 Overlapping position function of minimum overlap pattern illustrated in 3.4(d) 77
3.10 Numerical results in AWGN channel 81
3.11 Numerical results in multipath fading channel 82

4.1 Block diagram of Channel Estimator based on DFT interpolation. . . 85
4.2 Block diagram of Channel Estimator based on Most Significant Sample selection. 85
4.3 $\mathrm{MSE}(avg)$ normalized to the MMSE as a function of the ratio between number of pilots over number of taps, for several values of SNR. Using uniform channel and $\beta^2 = 1$. 92
4.4 Comparison between analytical, obtained from eq. (4.36), and simulated performance of several TCS selection strategies with uniform channel with $N_t = 6$. 103
4.5 Comparison between the performance of several threshold based MSS selection strategies with TU6 and uniform channel. 104
4.6 Comparison between TCS with Sub-Optimal threshold and state-of-the-art alternatives. Different mismatch levels between the actual and the assumed number of taps. 105
4.7 Comparison between the proposed MMS selection strategies based on energy estimation, using TU6, 50 km/h. 107
4.8 Channel estimation performance of the proposed algorithms, SOT and AES with $W = 10$, compared with the state-of-art alternatives, considering both the cases of uniform and non-uniform pilot pattern with the same number of pilots, $N_p = 71$. 108
4.9 Channel estimation performance of the proposed algorithms, IES and AES with several values of W, considering both the cases of uniform and non-uniform pilot pattern with the same number of pilots, $N_p = 71$. 109

4.10 Coded DVB-SH BER performance, QPSK,turbo code rate 1/4, considering both the cases of uniform and non-uniform pilot pattern with the same number of pilots, TU6, 50 km/h. 110
4.11 Coded DVB-SH BER performance, QPSK,turbo code rate 1/2, considering both the cases of uniform and non-uniform pilot pattern with the same number of pilots, using TU6 , 50 km/h. 111
4.12 Coded DVB-SH BER performance, 16QAM, turbo code rate 1/2, considering both the cases of uniform and non-uniform pilot pattern with the same number of pilots, using TU6, 50 km/h. 112

5.1 Block diagram of the SC-FDMA transmitter 116
5.2 Block diagram of the proposed system 117
5.3 Single user estimator 118
5.4 Block diagram of the proposed multi user estimator 120
5.5 Timing Estimation performance 123
5.6 CPE Estimation performance 124
5.7 QPSK BER performance 125
5.8 16QAM BER performance 126

LIST OF TABLES

3.1 Several values of M_{op} for DVB-SH value of N_g 68
3.2 Required shift register and adder in case of $N_g = 256$ 69
3.3 Power delay profile of multipath channel 69
3.4 Presented Pilot patterns. 76

4.1 Normalized power delay profile of the considered multipath channels 102

5.1 Considered SC-FDMA configuration parameters 122

This page intentionally contains only this sentence.

Acronyms

4G	Forth Generation
ACE	Active Constellation Extensions
ADC	Analogue to Digital Conversion
AES	Average Energy Selection
AWGN	Additive White Gaussian Noise
CCDF	Complementary Cumulative Distribution Function
CDF	Cumulative Distribution Function
CIR	Channel Impulse Response
CP	Cyclic Prefix
CPE	Common Phase Error
CTE	Coarse Timing Estimation
CTF	Channel Transfer Function
DA	Data-Aided
DAC	Digital to Analogue Conversion
DC	Double Correlator
DFT	Discrete Fourier Transform
DVB	Digital Video Broadcasting
DVB-H	DVB-Handheld

DVB-SH	DVB-Satellite to Handheld
DVB-SSP	DVB-Satellite Services to Portables
DVB-RCS	DVB-Return Channel via Satellite
DVB-T	DVB-Terrestrial, version 1
DVB-T2	DVB-Terrestrial, version 2
EWS	Exponential Weighted Sum
EEWS	Enhanced Exponential Weighted Sum
FFE	Fractional Frequency Estimation
FFT	Fast Fourier Transform
GI	Guard Interval
HPA	High Power Amplifier
ICI	Inter Carriers Interference
IDFT	Inverse Discrete Fourier Transform
IES	Instantaneous Energy Selection
IFE	Integer Frequency Estimation
IFFT	Inverse Fast Fourier Transform
ISI	Inter Symbol Interference
IUI	Inter User Interference
JMU	Joint Multi-User
KCS	Knowledge of the Channel Statistics
LTE	Long Term Evolution
MC	Maximum Correlation
ML	Maximum Likelihood
MMSE	Minimum Mean Square Error
MOD-COD	modulation and coding
MSSs	Most Significant Samples
NDA	Non-Data-Aided
OFDM	Orthogonal Frequency Division Multiplexing
OFDMA	Orthogonal Frequency Division Multiple Access
PAPR	Peak to Average Power Ratio
PDP	Power Delay Profile
PNM	Phase Noise Mask
SC-FDMA	Single Carrier Frequency Division Multiple Access
SDR	Signal-to-Distortion Ratio

SFN	Single Frequency Networks
SLM	Selected Mapping
SNR	Signal-to-Noise Ratio
SoF	Start of Frame
SSPA	Solid-State Power Amplifiers
TCS	Threshold Crossing Selection
TD	Total Degradation
TDM	Time Division Multiplex
T-DMB	Terrestrial Digital Multimedia Broadcasting
TDS-OFDM	Time-Domain Synchronous OFDM
TPS	Transmission Parameter Signalling
TR	Tone Reservation
TWTA	Travelling-Wave Tube Amplifiers
WF	Wiener Filtering
ZP-OFDM	Zero-Padded OFDM

This page intentionally contains only this sentence.

ORIGINAL CONTRIBUTIONS

In this Section, the original contributions contained in the Thesis are listed by topic:

- Peak-to-Average Power Ratio Reduction
  - A novel method that considerably reduces the PAPR is proposed in Section 2.3. This technique yields a quasi constant OFDM signal envelope. Both analytical and numerical results are provided. Part of the results have also been presented in [C2, C9], and disclosed in [Pat1] and [Pat2].
  - A modified version of RISM, identified as Hybrid RISM, is presented in Section 2.3.4.1. This technique has been disclosed in [Pat1], [Pat2], and [Pr1].
- Time and Frequency Synchronization
  - A novel joint symbol timing and carrier frequency synchronization algorithm characterized by a very low hardware complexity is presented in Section 3.3. Part of the results have also been presented in [C7].
  - A novel approach to the POST-FFT synchronization, including both pilot structure and receiver design, is presented in Section 3.4. Both analytical and numerical results are provided. Part of the results have also been presented in [C6].
- Channel Estimation
  - Novel lower bounds on the estimation MSE performance for any MSS selection strategy are presented in Section 4.3. Part of the results have also been included [J1].
  - The analytical derivation of the MSE of a TCS based channel estimation, as well as, the derivation of the optimum threshold value in minimum MSE sense are presented in Section 4.4.1.1. Part of the results have also been included in [C3] and [J1].

  - A sub-optimal approach for threshold setting, which yields comparable performance to the optimal case is proposed in Section 4.4.1.2. Part of the results have also been included in [J1].
  - Two novel MSS selection strategies, identified as Instantaneous Energy Selection and Average Energy Selection are presented in Sections 4.4.2.1 and 4.4.2.2 respectively. Part of the results have also been included in [J1].

- Single Carrier Frequency Division Multiple Access
  - The using of SC-FDMA in the Broadband Satellite Return Channel has been assessed in Section 5. Part of the results have also been presented in [C1].
  - A novel Joint Multi-User (JMU) estimation method for the SC-FDMA suitable to the addressed scenario is proposed in Section 5.2. Part of the results have also been presented in [C1].

Scientific Publications

Journal Articles

[J1] S. Rosati, G. E. Corazza, A. Vanelli-Coralli, "OFDM Channel Estimation based on Impulse Response Decimation: Analysis and Novel Algorithms", *IEEE Transaction on Communications*, vol.60, no.7, pp.1996-2008, July 2012.

[J2] F. Bastia, C. Bersani, E. A. Candreva, S. Cioni, G. E. Corazza, M. Neri, C. Palestini, M. Papaleo, S. Rosati, A. Vanelli-Coralli "LTE Adaptation for Mobile Broadband Satellite Networks", *EURASIP Journal on Wireless Communications and Networking*, March 2009.

Conference Proceedings

[C1] S. Rosati, S. Cioni A. Vanelli-Coralli, , G. E. Corazza, G. Gallinaro, A. Ginesi, "A Joint Multi-User Synchronization Method for SC-FDMA in Broadband Satellite Return Channel", *IEEE Global Telecommun. Conf. (GLOBECOM 10)*, Miami, USA, Dec. 2010.

[C2] S. Rosati, E. A. Candreva, G. E. Corazza, "Rotation-Invariant Sub-Carrier Mapping: A Novel Technique Enabling Quasi-Constant OFDM Envelope", *IEEE 5th Advanced Satellite Multimedia Systems Conference (ASMS 2010)*, Cagliari, Italy, Sep. 2010.

[C3] S. Rosati, G. E. Corazza, A. Vanelli-Coralli, "OFDM Channel Estimation with Optimal Threshold-Based Selection of CIR Samples", *IEEE Global Telecommun. Conf. (GLOBECOM 09)*, Honolulu, USA, Dec. 2009.

[C4] S. Rosati, A.B. Awoseyila, A. Vanelli-Coralli, C. Kasparis, G.E. Corazza and B.G. Evans, "Threshold Detection Analysis for OFDM Timing and Frequency Recovery", *IEEE Global Telecommun. Conf. (GLOBECOM 09)*, Honolulu, USA, Dec. 2009.

[C5] F. Bastia, G. E. Corazza, C. Palestini, S. Rosati, A. Vanelli-Coralli, "Preamble Insertion in Future Satellite-Terrestrial OFDM Broadcasting Standards", *Proc. of International Communications Satellite Systems Conference* (ICSSC) 2009, Edinburgh, 1-4 Jun. 2009.

[C6] S. Rosati, M. Villanti, A. Vanelli-Coralli, G.E. Corazza, "OFDM Post-FFT Frequency Recovery based on Silent Sub-Carriers", *Proc. of IEEE 10th International Symposium on Spread Spectrum Techniques and Applications*, (ISSSTA) 2008, Bologna, Italy, 25-28 Aug. 2008.

[C7] S. Rosati, S. Cioni, M. Neri, A. Vanelli-Coralli, and G.E. Corazza, "Joint Symbol Timing and Carrier Frequency Recovery for DVB-SH System", *Proc. of International Workshop on Satellite and Space Communications* (IWSSC) 2007, Salzburg, Austria, 13-14 Sep. 2007.

[C8] R. Suffritti, E.A. Candreva, F. Lombardo, S. Rosati, A. Vanelli-Coralli, G.E. Corazza, and G. Gallinaro, "A Mesh Network over a Semi-Transparent Satellite" accepted to *IEEE Global Telecommun. Conf. (GLOBECOM-11)*, Houston, USA, Dec. 2011.

[C9] S. Rosati, E. A. Candreva, Y. Nasser, Sung-Ryul Yun, G. E. Corazza, R. Mounzer, J.F. Hélard, and A. Mourad, "PAPR Reduction Techniques for the Next Generation of Mobile Broadcasting", submitted to *19th International Conference on Telecommunications (ICT 2012)*.

Patents

[Pat1] S. Rosati, E. A. Candreva, G. E. Corazza, "Metodo per la riduzione del rapporto tra la potenza di picco e la potenza media di un segnale modulato in divisione di frequenza ortogonale mediante mappatura di simboli in luoghi geometrici, e relativo sistema", filed to Italian Patent Office, Feb. 2010

[Pat2] S. Rosati, E. A. Candreva, G. E. Corazza, "Method for reducing the Peak-to-Average Power Ratio of an orthogonal frequency division multiplexing modulated signal by mapping symbols in geometric loci, and relevant system", filed to Patent Cooperation Treaty, Feb. 2011

International Projects

[Pr3] 2010 - present: DVB-TM-H standardization group (developing the next generation handheld and mobile broadcasting system DVB-NGH) with several contributions on the PAPR reduction techniques.

[Pr4] 2010 - present: the ESA/ESTEC funded project "Cost Effective Satellite Terminals for MESH Overlay Networking" aimed to promote the market penetration of satellite networks based on the mesh topology, allowing direct connectivity among remote satellite terminals without having to double-hop via a Hub station (performed in cooperation with Mavigex s.r.l.); in charged of Physical layer investigations and analysis.

[Pr5] 2008 - present: the funded EC FP7 IST Network of Excellence "Network of Excellence in Wireless Communications (NEWCOM++)" aimed at creating a trans-European virtual research centre linking a proper number of leading European research groups in a highly integrated, carefully harmonized, cooperative fashion.

[Pr6] 2008 - 2010: the ESA/ESTEC funded project "Enhanced Multicarrier OFDM Digital Transmission Techniques for Broadband Satellites" aimed at the enhancement of OFDM Digital Transmission Techniques for mobile and fixed Broadband Satellites (performed in cooperation with Mavigex s.r.l.); in charge of the analysis of: hybrid network channel modeling; channel estimation; signal detection; time and frequency synchronization;

[Pr7] 2009 - 2010: the ESA/ESTEC funded project "2nd Generation of DVB-RCS Standardization Support" - aimed at supporting the standardization activities of the DVB-RCS group; in charge of the analysis of: Time and frequency Synchronization, and SC-FDMA assessment;

[Pr8] 2007 - 2009: the funded EC FP6 IST Network of Excellence "SatNEx-II" - aimed at establishing a long-lasting, durable integration of European research in satellite communications and to advance European research in satellite

communications through a joint programme of activities addressing the research, as well as the integration and training needs of the European Union.

[Pr9] 2007 - 2008: the ESA/ESTEC funded project “Study of Satellite Role in 4G Mobile Networks” - aimed at the definition of the satellite role in 3G and beyond mobile networks; in charge of the analysis of: Channel Estimation; Time and frequency Synchronization;

INTRODUCTION

Once you do know what the question actually is,
you'll know what the answer means.

The Hitchhiker's Guide to the Galaxy, Douglas Adams

N NOWADAYS SOCIETY there is an increasing demand for access to information and services anytime and everywhere. Differently from the past this demand is not driven by few business users, but by larger community of users which expects to access a large amount of data for either entertainment or social networking reasons. As a consequence, an increasing number of people are asking for rich multimedia contents (TV-streaming, Youtube, etc...) which require a high data rate connections. Therefore, broadband access is considered in Europe and the rest of the World as a fundamental element of economic and social growth. In particular, The European Digital Agenda set forth challenging objectives for the future years for digital inclusions and internet access for everyone. One of the objectives set for 2020 is to provide each European Citizen 30 Gbps access and 100 Gbps for at least the 50 % of households.

The challenge of the next generation wireless communication systems is to enable these services providing an enormous and increasing amount of data at anytime and everywhere through high speed data links. In order to fulfill this requirements the 4G network candidate systems must rely on the most advanced signal and receive designs based on the concept of orthogonal transmission.

As a matter of fact, Orthogonal Frequency Division Multiplexing (OFDM)[1] [2] and its counterparts for multiple access: Orthogonal Frequency Division Multiple Access (OFDMA) and Single Carrier Frequency Division Multiple Access (SC-

FDMA) are increasingly used in new generation wireless communication standard. This trend is testified by the adoption of OFDMA and SC-FDMA in all next Fourth-Generation network candidates, such as 3GPP Long Term Evolution Advanced (LTE-Advanced) and WiMAX. OFDM has been also chosen in the most recent standards for digital broadcasting: DVB-NGH (Digital Video Broadcasting Next Generation Handheld), DVB-T2 (Digital Video Broadcasting-Terrestrial, version 2), T-DMB (Terrestrial Digital Multimedia Broadcasting), MediaFLO. Furthermore OFDM is also adopted in those standard that foresee hybrid satellite terrestrial network as DVB-SH (Digital Video Broadcasting-Satellite to Handheld).

The principle characteristic of wireless communications is the presence multi-path propagation which leads to frequency selective fading [3]. OFDM brilliantly solves the problem of frequency selective fading using low-complexity equalizers, with a single tap per subcarrier. This is due to the fact that propagation channels which are frequency selective over the entire bandwidth may appear non-selective on each narrowband subcarrier. In particular, this is crucial for the case of Single-Frequency Networks (SFN) characterized by a strongly time dispersive and then highly frequency-selective channels [4]. Evidently, the demodulation of the signal will perform successfully if and only if the receiver if fully synchronized with the transmitter and the channel is accurately estimated. Furthermore, we must take into account that the OFDM modulation is particularly vulnerable to the effect of nonlinear distortions. Hence, channel Estimation, time and frequency synchronization, and countermeasures to nonlinear distortions, are *the* crucial problems to be faced during the design of the advanced OFDM systems.

Motivation and goals

This thesis is the outcome of the work performed within my Ph.D. research activities at the University of Bologna. During my Ph.D. I dealt with the aforementioned fundamental design problems, proposing novel solutions and ideas which have contributed to an advanced design of the OFDM waveform and receivers. These new ideas and technical solutions have been proposed and assessed during several international projects in which I have been involved [Pr1-Pr7] providing the proof of their feasibility in practical systems. In particular, the novel techniques, which we proposed to reduce the envelope fluctuations of the signal and then and improves the OFDM resilience to the nonlinear distortion, have been the subject

of technical contributions to the DVB-NGH standard and also of an Italian and an International patent [Pat1-Pat2] owned by the University of Bologna. Last but not least, during my Ph.D. I had the privilege of spending more than six months working at the Corporate R&D division of Qualcomm, in San Diego, CA, USA. The activity I accomplished in Qualcomm was focused on enhanced MIMO techniques for 3GPP LTE-Advanced (Rel. 10). During this activity, several 3GPP technical contributions and a patent application (pending) have been carried out. The scientific outcomes of this experience are not included in this Thesis.

This page intentionally contains only this sentence.

Chapter 1

OFDM Principles

The word "Orthogonal" comes from the Greek *orthos*, meaning "straight", and *gonia*, meaning "angle".

N THE INTRODUCTION we have seen how the OFDM modulation has become the most attractive modulation scheme in broadband wireless systems. In this section we focus on the basic principles of this advantageous modulation, highlighting the reasons behind its success. In brief, the main strengths of OFDM are:

- **its ability to cope with strongly dispersive channels** using an efficient and low-complex frequency-domain equalization. In fact, propagation channels which are frequency selective over the entire bandwidth may appear non-selective on each narrowband subcarrier. By introducing a guard interval containing a cyclic prefix between two adjacent OFDM symbols it is possible to maintain the orthogonality between the subcarriers, and then, avoid both Inter Carrier Interference (ICI) and Inter Symbol Interference (ISI). Clearly, this holds true if and only if accurate frequency and timing synchronization and channel estimation are performed at the receiver.

- **its efficient and flexible spectrum resource management**. In OFDMA each subcarrier can be allocated to a different user. This way, it is possible to obtain a very high spectral efficiency avoiding inter user interference (IUI). This feature enables a smart and flexible scheduling that can take advantages on the fine discretization of the spectrum resources.

These properties justify the success of the OFDM modulation. In particular, they becomes crucial for Single Frequency Networks (SFN), where, in order to achieve seamless radio coverage, identical signals are transmitted from widely separated sites. In this case, signal replicas may be received with very large differential delays, giving rise to very sparse channel profiles, which are very hard to equalize using a single carrier modulation.

On the other hand, the main disadvantages of OFDM are:

- **its high sensitivity to frequency offsets**. This vulnerability stems from the very limited subcarrier spacing. In fact if the frequency misalignment at the receiver is in the order of tenth of the subcarrier spacing a severe ICI occurs. For this reason an accurate frequency synchronization must be performed.

- **its low resilience to non-linear distortion**, which is considerably inferior with respect to that offered by single carrier systems. This is because the OFDM signal is characterized by large amplitude fluctuations caused by the summation of a large number of complex sinusoids. Considering the Central Limit Theorem, if N is large enough the signal envelope can be modelled as Rayleigh distributed.

- **its high sensitivity to Doppler spread**. This drawback arise again from the very small subcarrier spacing. If the Doppler spread is comparable to the subcarrier spacing severe ICI occurs.

The main scope of this thesis is to study, create, and propose, countermeasures against the aforementioned drawbacks. In particular: in Chapter 2 we present a method which aim to reduce the envelope fluctuations of the OFDM signal and and improves the OFDM resilience against the non-linearities; in Chapter 3 we discuss both timing and frequency synchronization aspects; in Chapter 4 we face the channel estimation problem, proposing novel estimation methods which can nearly reach the best theoretical performance.

1.1 Why Parallel is Smarter Than Serial

In the traditional single carrier systems the entire bandwidth B is devoted for T_s seconds to send just one information symbols. In other words, information symbols are transmitted serially, using a wideband for a short symbol time, T_s. Evidently, the higher the throughput, the shorter the symbol time, and thus, the larger the

bandwidth needed. Let us assume a simple 2-path channel, (i.e. we are assuming to receive two replicas of the signal having different time of arrival), where the relative delay is larger than the symbol time. In this case the delayed signal replica acts as interference, yielding ISI. This reduces the capability to properly demodulate the transmitted signal. Therefore, it is straightforward to note that the higher the throughput the smaller the maximum tolerable relative delay. For this reason, single carrier systems are considered vulnerable to multipath channels.

Let us now assume to transmit simultaneously N sequential streams of information symbols, where each stream occupies only a small part of the entire bandwidth. If the orthogonality between the streams is preserved, it is possible to reach the same throughput of the serial case having a symbol duration N times larger. Therefore the maximum tolerable relative delay becomes N times larger. In other words each information symbols are transmitted over a narrowband which can be assumed to be frequency-flat. This simple multicarrier scheme has been, however, limited by its complexity. Indeed, a bank of filters, N modulators, and N demodulators, are needed. Furthermore the local oscillators must to be extremely precise in order to maintain the orthogonality between the subcarriers. This is the reason why the multicarrier systems, which have been theorized around 1960 were not practically implemented for a long time.

1.2 Orthogonality

An early problem of the multicarrier systems was to identify a set of orthogonal basis functions having an acceptable spectral efficiency. Let us consider a generic multicarrier system using a set of N generic basis functions, $\bar{\phi}(t) = \{\phi_0(t), \ldots, \phi_{N-1}(t)\}$. The multicarrier transmitted signal is given by:

$$s(t) = \sum_{\ell=0}^{\infty} \sum_{k=0}^{N-1} x_{k,\ell} \phi_k(t - \ell T_u) \tag{1.1}$$

where T_u is the symbol duration and $x_{0,\ell}$ is the complex information symbol corresponding to the ℓ-th multicarrier symbol and to the k-th subcarrier. In figure 1.1 the block diagram of a generic multicarrier system is illustrated.

In order to avoid both ICI, and ISI the set of basis functions must verify the

following conditions:

$$\int_{-\infty}^{\infty} \phi_k(t - vT_u)\phi_k^*(t - uT_u)dt = \begin{cases} 1 & \text{if } u = v \\ 0 & \text{otherwise} \end{cases} \tag{1.2}$$

to eliminate ISI, and,

$$\int_{-\infty}^{\infty} \phi_u(t - \ell T_u)\phi_v^*(t - \ell T_u)dt = \begin{cases} 1 & \text{if } u = v \\ 0 & \text{otherwise} \end{cases} \tag{1.3}$$

to eliminate ICI.

Let us suppose $\bar{\phi}(t)$ being:

$$\phi_k(t - \ell T_u) = \frac{1}{\sqrt{T_u}} \,\text{rect}\left(\frac{t - \ell T_u}{T_u}\right) \mathrm{e}^{\jmath 2\pi f_k t} \tag{1.4}$$

a set of rectangular-shaped basis[1] having a time duration of T_u seconds. Substituting (1.4) in (1.2), we obtain:

$$\begin{aligned} &\int_{-\infty}^{\infty} \phi_k(t - vT_u)\phi_k^*(t - uT_u)dt = \\ &= \frac{1}{T_u}\int_{-\infty}^{\infty} \text{rect}\left(\frac{t - uT_u}{T_u}\right) \text{rect}\left(\frac{t - vT_u}{T_u}\right) dt = \begin{cases} 1 & \text{if } u = v \\ 0 & \text{otherwise} \end{cases} \end{aligned} \tag{1.5}$$

therefore ISI is avoided. Similarly we substitute (1.4) in (1.3) obtaining:

$$\begin{aligned} &\int_{-\infty}^{\infty} \phi_k(t)\phi_{k'}^*(t)dt = \\ &= \int_{\ell T_u}^{(\ell+1)T_u} \left[\text{rect}\left(\frac{t - \ell T_u}{T_u}\right)\right]^2 \mathrm{e}^{\jmath 2\pi(f_k - f_{k'})(t - \ell T_u)} dt = \\ &= \frac{\mathrm{e}^{\jmath 2\pi(f_k - f_{k'})T_u} - 1}{\jmath 2\pi(f_k - f_{k'})T_u} = \begin{cases} 1 & \text{if } T_u\delta_{k,k'} = 0 \\ 0 & \text{if } T_u\delta_{k,k'} \in \mathbb{Z} \end{cases} \end{aligned} \tag{1.6}$$

where $\delta_{k,k'} = f_k - f_{k'}$ represents the frequency spacing between f_k and $f_{k'}$. Therefore, the condition (1.3) is satisfied if and only if the frequency spacing between two generic subcarriers is an integer value of $1/T_u$. Hence, we infer that the subcarrier spacing, f_u, which maximize the spectral efficiency maintaining the orthogonality between the subcarriers is:

$$f_u = \frac{1}{T_u} \tag{1.7}$$

[1] where: $\text{rect}\,(t) = \begin{cases} 0 & \text{if } |t| > \frac{1}{2} \\ 1 & \text{if } |t| \leq \frac{1}{2} \end{cases}$

We have just showed that using a set rectangular-shaped basis having time duration T_u, and subcarrier spacing $f_u = 1/T_u$, it is possible to eliminate both ISI and ICI, maximizing the spectral efficiency. Now we can rewrite Eq. (1.1) considering (1.4) and (1.7), obtaining the OFDM transmitted signal:

$$s(t) = \frac{1}{\sqrt{T_u}} \sum_{\ell=0}^{\infty} \sum_{k=0}^{N-1} a_{k,\ell} \, \text{rect}\left(\frac{t - \ell T_u}{T_u}\right) \mathrm{e}^{\jmath 2\pi k/T_u} \, \mathrm{e}^{\jmath 2\pi f_0 t} \tag{1.8}$$

In Figure 1.2 the spectrum of OFDM signal is reported. The OFDM spectrum results being a summation of N Sinc functions[2] It is approximately flat in the central part of the band, while decaying rapidly out of band. Note that the higher N the flatter is the in-band OFDM spectrum. Clearly the OFDM signal is not bandlimited, however we can define the net bandwidth as $B_{OFDM} \doteq N/T_u = 1/T$. Let us consider a generic OFDM system with N subcarriers where the constellation cardinality is equal to 2^M. This system can convey NM bits, every each T_u seconds. Thus, the resulting spectral efficiency is equal to $M \; bit/sec/Hz$. Clearly, in the actual systems the is spectral efficiency decrease because of the guard interval and the frequency bands insertions.

1.3 Using the Fast Fourier Transform

A OFDM system can be implemented in practice employing banks of shaping filters, however this design requires fine local oscillators in order to satisfy the condition in (1.7). Unfortunately such a precise and expensive devices may make the implementation of OFDM not feasible in practice. The crucial hardware simplification that made the OFDM implementation feasible is the employment of the Fast Fourier Transform (FFT) [5]. Indeed, the baseband transmitted signal corresponding to the ℓ-th multicarrier symbol, sampled every $T = T_u/N$ seconds,

$$s_{i,\ell} = \frac{1}{\sqrt{N}} \sum_{k=0}^{N-1} x_{k,\ell} \, \mathrm{e}^{\jmath 2\pi k i/N} \qquad i = 0, \ldots, N-1 \tag{1.9}$$

can ne write as the N-point Inverse Discrete Fourier Transfer (IDFT) of the vector of complex information symbols $\bar{x}_\ell = (x_{0,\ell}, \ldots, x_{N-1})$ as follows:

$$\bar{s}_\ell = IDFT(\bar{x}_\ell) \tag{1.10}$$

[2] where: $\text{sinc}(x) = \begin{cases} 1 & \text{if } x = 0 \\ \frac{\sin(\pi x)}{\pi x} & \text{otherwise} \end{cases}$

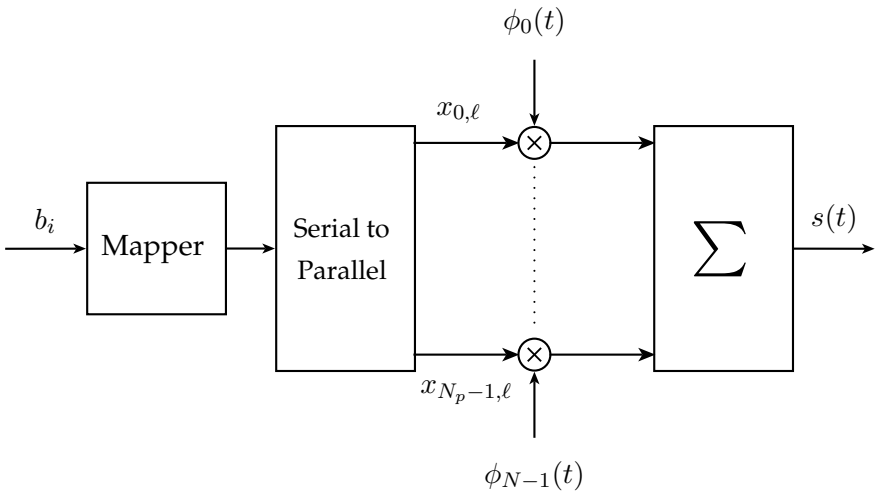

Figure 1.1: Block diagram of a generic multicarrier transmitter.

Similarly at the receiver, the demodulation can be performed through a Discrete Fourier Transfer (DFT). Furthermore, if N is a power of two DFT can be implement in a very efficient way using the FFT implementation which is widely available in integrated circuits. The block diagram of the OFDM transmitter is using IDFT is illustrated in Figure 1.3.

1.4 Guard Interval and Cyclic Prefix

As anticipated in before, one of the main reasons behind the success of the OFDM modulation is its ability to cope with multipath fading channels. Nevertheless, a time dispersive channel having delay spread larger than T will destroy the orthogonality of the signal causing both ISI and ICI. The strength of the OFDM modulation lies in the fact that we can efficiently preserve the orthogonality by taking a simple precaution.

The ISI can be easily avoided inserting a Guard Interval (GI), having time duration T_g, at the beginning of every OFDM symbol, as illustrated in Fig 1.4. In this manner, if the maximum delay τ_{max} is smaller than T_g, ISI is eliminated but at the expense of the capacity. Now, the overall OFDM time symbols, including the GI durations, becomes $T_L = T_u + T_g$, hence this translates in a capacity loss of T_g/T_u.

In literature several ways to fill GI have been proposed. In the Zero-Padded

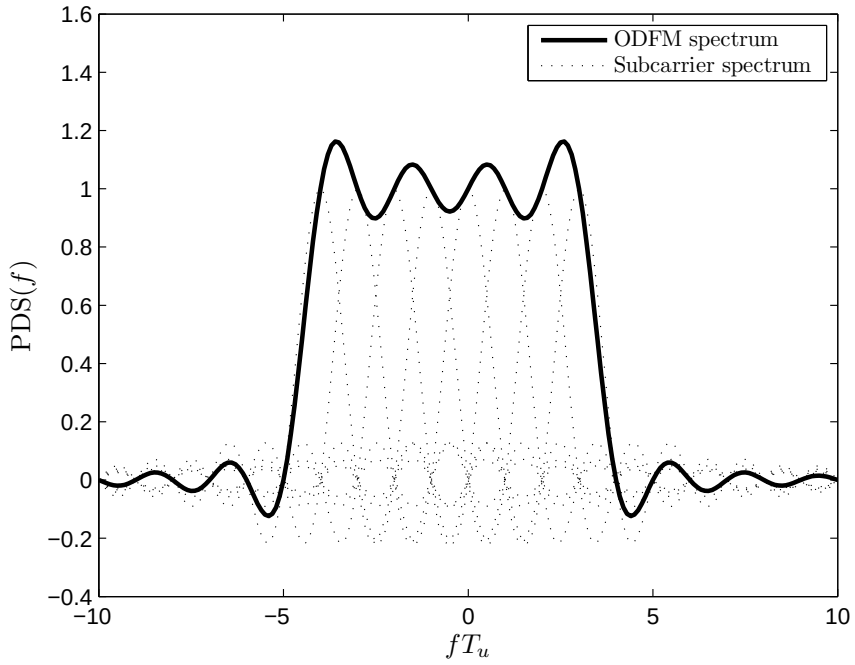

Figure 1.2: PSD of a OFDM signal with $N = 8$ subcarriers.

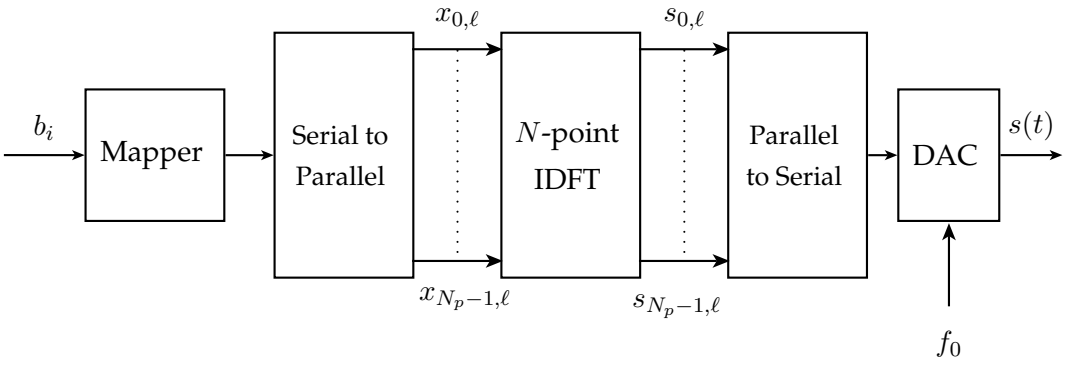

Figure 1.3: Block diagram OFDM transmitter using Discrete Fourier Transform.

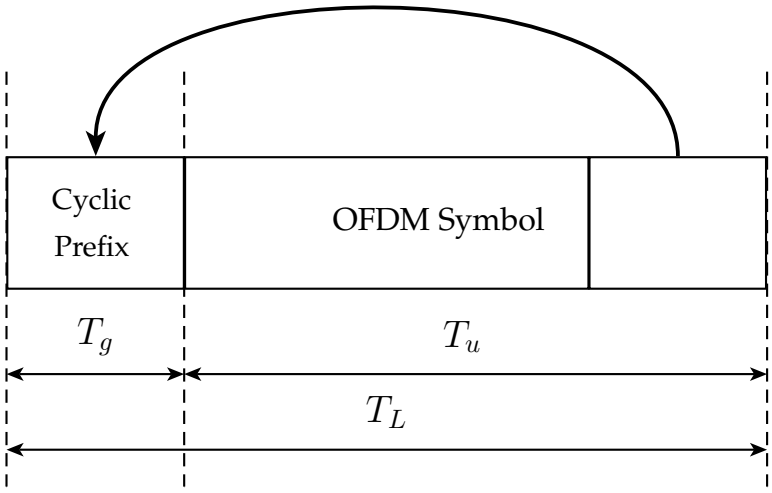

Figure 1.4: Cyclic Prefix.

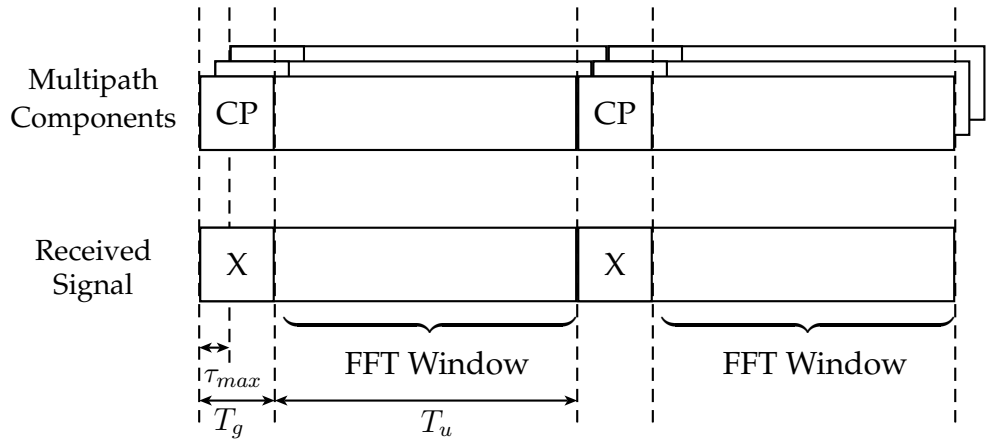

Figure 1.5: OFDM signal over time dispersive channel.

OFDM (ZP-OFDM) the transmitter is muted during the GI[6], in other words the GI is filled with zeros. Another approach is Time-Domain Synchronous OFDM (TDS-OFDM), where a known training sequence is transmitted during the GI in order to facilitate the synchronization tasks. Unfortunately both of these solutions do not avoid ICI.

On the other hand, an efficient and easy method to eliminate both ISI and ICI is to transmit a Cyclic Prefix (CP) within the GI. As illustrated in Figure 1.4, the CP consists in a copy of the final part of the following OFDM symbol. Note that, if the maximum delay τ_{max} is shorter than T_g, the receiver, in performing the OFDM demodulation through FFT, will integrate over an integer number of sinusoid cycles for each of the received multipaths. As a consequence, both ISI and ICI are eliminated. Figure 1.5 illustrates how the CP acts to maintain the orthogonality between subcarriers.

Also some other alternatives that do not make use of GI have been proposed in literature. These solutions such as: Offset Quadrature Amplitude Modulation OFDM (OQAM-OFDM) [7], [8]; Isotropic Orthogonal Transform Algorithm (IOTA) OFDM [9], [10]; or more in general Filter Banks based Multicarrier (FBMC) systems; are based on the employment of not-rectangular pulse shapes that can reduce both ICI and ISI, but at the expense of additional complexity.

1.5 Basic system model

The aim of this Section is to provide a common OFDM system model which will be considered in the analysis addressed in following chapters. We consider an OFDM signal using N subcarriers, where the ℓ-th OFDM symbol, $\bar{s}_\ell = (s_{0,\ell}, \ldots, s_{N-1,\ell})$, is obtained as the N-point IDFT of the vector of complex symbols $\bar{x}_\ell = (x_{0,\ell}, \ldots, x_{N-1,\ell})$, as follows

$$s_{i,\ell} = \frac{1}{\sqrt{N}} \sum_{k=0}^{N-1} x_{k,\ell}\, \mathrm{e}^{\jmath 2\pi k i/N} \qquad i = 0, \ldots, N-1 \tag{1.11}$$

The complex symbols $x_{k,\ell}$ carry either data information, $a_{k,\ell}$, or pilot reference symbols, $p_{k,\ell}$, used for data-aided channel estimation and synchronization. Let N_p be the number of pilot subcarriers, the ratio $\eta_d = (N - N_p)/N$ is defined as the *data carrier efficiency*, so that $1 - \eta_d$ corresponds to the *pilot density*, which represents an important design parameter. We assume to have uniformly scattered pilot tones in each OFDM symbol, in other words the pilot spacing is considered constant. Furthermore, to improve channel estimation performance, pilots can be transmitted

with an energy boost factor β^2 with respect to data symbols (i.e. $E[p_{k,\ell}^2] = \beta^2 E_s$, where $E[a_{k,\ell}^2] = E_s$). Let $P(\ell)$ be the set of pilot subcarrier indices in the ℓ-th OFDM symbol, identified as *pilot pattern*, of size N_p. We can write

$$x_{k,\ell} = \begin{cases} p_{k,\ell} & \text{if } k \in P(\ell) \\ a_{k,\ell} & \text{if } k \notin P(\ell) \end{cases} \tag{1.12}$$

As illustrated in Section 1.4, in order to maintain the subcarrier orthogonality and then avoid both ISI and ICI, a CP composed by N_g samples is inserted at the beginning of each OFDM symbol. This is followed by Digital to Analogue Conversion (DAC) at sampling rate $R = 1/T$, and using an appropriate analog transmission filter, $g_T(\tau)$, so that the time continuous signal can be written as

$$s(t) = \frac{1}{\sqrt{T_u}} \sum_{\ell=-\infty}^{\infty} \sum_{k=0}^{N-1} \text{rect}\left(\frac{t}{T_L} - \frac{1}{2} - \ell\right) x_{k,\ell} \mathrm{e}^{j\,2\pi \frac{1}{T_u} k(t-T_g)} * g_T(\tau) \tag{1.13}$$

where $*$ denotes convolution, $T_u = NT$ and $T_g = N_g T$ represent respectively the OFDM useful symbol duration, and the guard interval. Therefore $T_L = T_u + T_g$ is the total OFDM symbol duration, and $f_u = 1/T_u$ is the subcarrier spacing. Notably, the normalization factor $\frac{1}{\sqrt{T_u}} = \frac{1}{\sqrt{N}} \cdot \frac{1}{\sqrt{T}}$ accounts for both the IDFT and the D/A normalization factors.

The OFDM signal is transmitted over a time-varying and frequency-selective fading channel. Under the assumption that the channel coherence time exceeds T_L, which is necessary for correct OFDM operation, the baseband equivalent CIR is modelled as a tapped delay line which comprised of CIR and the transmission filter:

$$h(t, \tau) = \sum_j h_j(t) \cdot \delta(\tau - \tau_j) \tag{1.14}$$

where $h_j(t)$ and τ_j are respectively the gain and delay of the j-th path, at time t. In Rayleigh fading condition, at any time instant $h_j(t)$ can be modelled as a complex Gaussian random variable with zero mean and variance $\gamma_j^2/2$ per branch. The total average channel energy is normalized to unity, i.e. $\sum_j E[h_j^2] = \sum_j \gamma_j^2 = 1$, and the maximum delay is assumed to be smaller than the guard interval duration [11], i.e. $\tau_{max} = \max_j \tau_j < T_g$. Again, this is always verified in normal OFDM operation. Thus, the received signal can be written as

$$r(t) = h(t) * s(t) + n(t) \tag{1.15}$$

where $n(t)$ represents a complex Additive White Gaussian Noise (AWGN) random process, with two-sided power spectral density equal to N_0. After matched filtering

and sampling the received signal every T seconds, assuming the receiver filter is flat within the transmitting bandwidth, yields

$$r(uT) = \sum_j h_j(uT)\ s(uT - \tau_j) + n(uT) \tag{1.16}$$

Removing the guard interval and re-arranging the vector at the input of the DFT, the samples belonging to the ℓ-th OFDM symbol can be collected into a vector $\bar{r}_\ell$ with components:

$$\begin{aligned} &r_{i,\ell} = r(((\ell-1)(N+N_g) + N_g + i)T) \\ &i = |u|_{N+N_g} - N_g \qquad \ell = \lceil u/(N+N_g) \rceil \end{aligned} \tag{1.17}$$

where $\lceil \cdot \rceil$ indicates the smallest integer larger than the argument. Having assumed that $h_j(t)$ remains constant over an OFDM symbol duration, at the output of the DFT, in the frequency domain, the observed samples are:

$$y_{k,\ell} = \frac{1}{\sqrt{N}} \sum_{i=0}^{N-1} r_{i,\ell}\ \mathrm{e}^{-\jmath\, 2\pi ki/N} = x_{k,\ell} H_{k,\ell} + n_{k,\ell} \qquad k = 0, \ldots, N-1 \tag{1.18}$$

where $n_{k,\ell}$ is the complex AWGN sample in the frequency domain with zero-mean and variance N_0, and $H_{k,\ell}$ is the CTF sample at the k-th subcarrier, in the ℓ-th symbol. The latter can be expressed as:

$$H_{k,\ell} = \sum_{i=0}^{L-1} h_{i,\ell} \mathrm{e}^{-\jmath\, 2\pi ki/N} \qquad k = 0, \ldots, N-1 \tag{1.19}$$

where L represents the length of the CIR, and $h_{i,\ell}$ the complex gain of the i-th tap during the ℓ-th OFDM symbol transmission.

This page intentionally contains only this sentence.

CHAPTER 2

NONLINEAR DISTORTION: ANALYSIS AND COUNTERMEASURES

In the mountains, the shortest way is from peak to peak:
but for that you must have long legs.

Thus Spoke Zarathustra: A Book for All and None, Friedrich Nietzsche

AS ANTICIPATED IN Chapter 1, one of the main drawbacks of OFDM systems is their vulnerability to nonlinear distortion. In fact, since the OFDM signal presents very high envelope fluctuations, its sensitivity to the nonlinear distortion appears to be considerably higher than that provided by single carrier systems. A fundamental parameter of the OFDM signal is the Peak-to-Average-Power Ratio (PAPR) which is defined as the ratio between the strongest time domain sample of a OFDM symbol and its average power:

$$\mathrm{PAPR}(\ell) = \frac{\max\limits_{i} s_{i,\ell}^2}{\frac{1}{N}\sum\limits_{i=0}^{N-1} s_{i,\ell}^2} \tag{2.1}$$

It is worthwhile to note that the higher is the subcarriers number N, the higher, in average, will be the resulting PAPR. This can be explained noting that, as illustrated in Eq. (1.8) and Eq. (1.13), OFDM signals are composed by the sum of N of complex sinusoids, therefore, considering the Central Limit Theorem, if N is large enough the transmitted signal can be modelled as a Gaussian variable. Thus, the

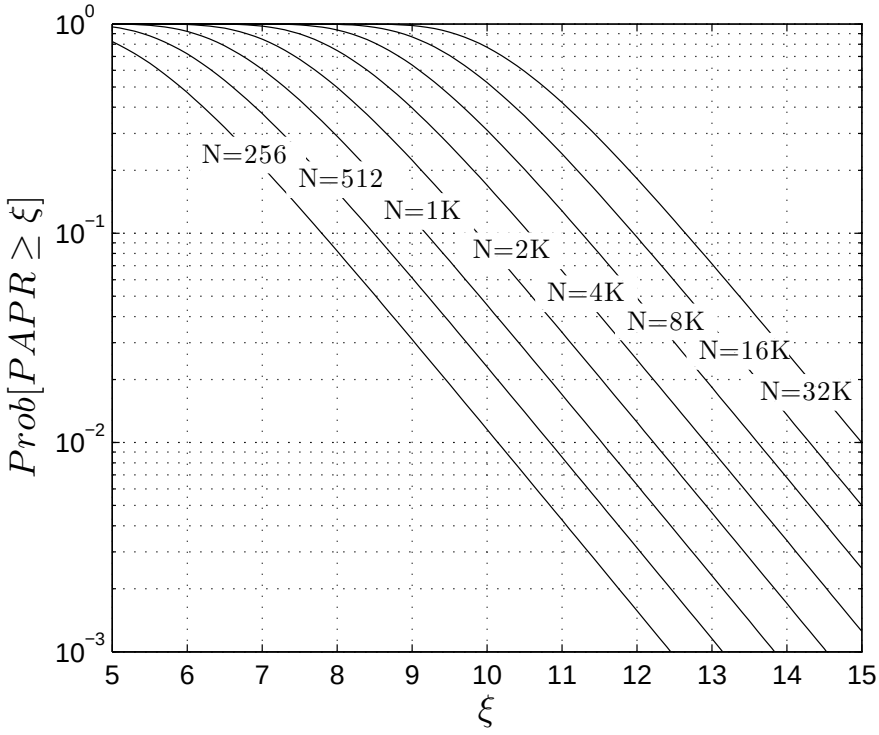

Figure 2.1: PAPR CCDF for several values of subcarriers number, N

probability that $\max_i s_{i,\ell}^2$ does not exceed a given value ξ is given by:

$$\text{Prob}\left[\max_i s_{i,\ell}^2 \leq \xi\right] = \left(1 - \mathrm{e}^{-\xi}\right)^N \tag{2.2}$$

if N is large enough we can write that:

$$\frac{1}{N}\sum_{i=0}^{N-1} s_{i,\ell}^2 \approx 1 \tag{2.3}$$

therefore, we can express the CCDF of the PAPR as:

$$\text{Prob}\left[\text{PAPR}(\ell) \geq \xi\right] \approx 1 - \left(1 - \mathrm{e}^{-\xi}\right)^N \tag{2.4}$$

In figure 2.1 the Complementary Cumulative Distribution Function (CCDF) of the PAPR is reported for several values of subcarriers number, N.

Several studies have been performed on the impact of nonlinearities on Gaussian signals. In particular [13] and [14] gave the basis to analyze the behavior of

OFDM systems in presence of nonlinearities. In [13] Bussgang stated that the output of a nonlinear system fed by a Gaussian signal can be expressed as a scaled replica of the input and a noise component uncorrelated to the input. In [14] Minkoff extended this work to complex signals, highlighting the so-called *AM-PM conversion* that is the phase distortion in output signal. Based on these early studies on Gaussian signals, when OFDM started to be applied, its performance on nonlinear channels has been assessed [15], [16], [17], [18]. As it can be clearly seen in these early works, the loss from linear channels to nonlinear channel is considerable, and prevented, for the first period, the application OFDM modulation on severely degraded channels such as the satellite links where nonlinearities cannot be avoided since the power efficiency is a critical requirements. This is why, for example the DVB-S2 [19] standard, differently from the other DVB standards, is based on a single carrier instead of multicarrier system. The first standardized system which makes use of OFDM in a satellite link is the DVB Satellite to Handheld (DVB-SH) standard released in June 2007 [20]. This standard is an extension of the DVB-H standard [21] to satellite networks. In particular, DVB-SH specifies two different physical layer configurations: the SH-A configuration refers to the use of the OFDM radio interface in both satellite and terrestrial links, while the SH-B configuration introduces the Time Division Multiplex (TDM) approach in the satellite link, maintaining the OFDM air interface for the terrestrial link.

More recently, the adoption of the SC-FDMA has been considered during the standardization of DVB Return Channel via Satellite (DVB-RCS) Standard [22]. As illustrated in [23] and in Chapter 5, the SC-FDMA solution appears suitable for satellites links, because of its lower PAPR compared to the OFDMA. On the other hand, it requires an accurate time and frequency synchronization. Furthermore, at the time of writing , the author is involved in the DVB-NGH standardization, where the adoption of the novel PAPR Reduction [24] presented in Section 2.3.4.1, is under consideration.

2.1 Nonlinear Distortion Analysis

In Section 1.5, we have considered the ideal case of linear transmission, however, in real-world systems, the effect of the nonlinearities introduced by the High Power Amplification (HPA) should be taken into account. In this Section, we firstly introduce a mathematical model describing a generic distorting HPA; secondly, we

review the most known memoryless HPA model, such as Ideal Clipping, Saleh model, and, Rapp model; and finally we highlight the nonlinear distortion effects on the OFDM signal using the introduced models.

2.1.1 HPA Modelling

We address the distortion owing to HPA acting on both the envelope (AM/AM) and phase (AM/PM) of the signal. Considering a generic complex nonlinear distortion function the output signal can be expressed as:

$$s_d(t) = F[\rho(t)]\mathrm{e}^{\jmath\{\angle s(t)+\Phi[\rho(t)]\}} \tag{2.5}$$

where $\rho(t)$ and $\angle s(t)$ represent respectively the envelope and the phase of $s(t)$, and $F[\cdot]$ and $\Phi[\cdot]$ represent respectively the AM/AM and AM/PM characteristics. Note that the nonlinear distortion function only depends on the envelope of the input signal.

In its original writing [13], Bussgang Theorem states: *"For two Gaussian signals, the cross-correlation function taken after one of them has undergone nonlinear amplitude distortion is identical, except for a factor of proportionality, to the cross-correlation function taken before the distortion"*. The mathematical expression of this stated theorem is:

$$< s'(t)s_d^*(t) >= \alpha < s'(t)s^*(t) > \tag{2.6}$$

where $<a(t)>= \lim_{T\to\infty} 1/T \int_{-T/2}^{T/2} a(t)\,dt$ and $s'(t)$ and $s(t)$ are Gaussian random processes. In the particular case of $s'(t) = x(t+\tau)$, Eq. (2.6) becomes:

$$< s(t+\tau)s_d^*(t) >= \alpha < s(t+\tau)s^*(t) > \quad \forall\tau \tag{2.7}$$

Therefore, the Bussgang theorem gives us the proof of the separability of a nonlinear output as the sum of a useful attenuated input replica and an uncorrelated nonlinear distortion, thus we can write the output as:

$$s_d(t) = \alpha s(t) + d(t) \tag{2.8}$$

where $s(t)$ and $d(t)$ are uncorrelated (i.e. $< s(t+\tau)d^*(t) >= 0\ \forall\tau$) and the complex attenuation coefficient α is given by:

$$\alpha = \frac{< s(t)s_d^*(t) >}{< s(t)s^*(t) >} \tag{2.9}$$

Assuming the ergodicity of $s(t)$, Equation (2.9) can be expressed as:

$$\alpha = \frac{1}{\sigma^2}\left(\int_0^\infty F[\rho(t)]\mathrm{e}^{-\jmath\Phi[\rho(t)]}\,\rho(t)\,p(\rho)\,d\rho\right)^* \tag{2.10}$$

where σ^2 represent the power of $s(t)$, $p(\rho)$ is the Rayleigh probability density function, which characterizes $\rho(t)$. Following the tractation in [25], it can be useful to define a scaling parameter β such as

$$E[s_d^2(t)] = \beta E[s^2] = |\alpha| E[s^2(t)] + E[d^2(t)] \tag{2.11}$$

and it can be written as

$$\beta = \frac{1}{E[s^2(t)]} \int_0^\infty |F[\rho(t)]|^2 p(\rho) d\rho \tag{2.12}$$

In this way, the power of the useful signal and the distortion noise are $|\alpha|^2$ and $(\beta - |\alpha|^2)$ respectively. Therefore [25]:

$$E[d^2(t)] = E[s^2(t)] \left(\beta - |\alpha|^2\right) \tag{2.13}$$

Now we can derive the expression of a Signal-to-Distortion Ratio (SDR) as:

$$\text{SDR} \doteq \frac{\alpha^2 E\left[s^2(t)\right]}{E\left[d^2(t)\right]} \tag{2.14}$$

Then, substituting Eq. (2.13) in Eq. (2.22) we obtain:

$$\text{SDR} = \frac{\alpha^2}{\beta - |\alpha|^2} \tag{2.15}$$

The Input Back-Off (IBO) is an important system parameter relating the saturation power of the HPA to the average power of the input signal. It is defined as:

$$\text{IBO} \doteq \frac{P_{in}^{sat}}{P_{in}} \tag{2.16}$$

where P_{in}^{sat} is the input saturation power, and $P_{in} = E[s^2]$ is the average input power.

The Output Back-Off (OBO) is defined in the same way of IBO, but referring to output parameters:

$$\text{OBO} \doteq \frac{P_{out}^{sat}}{P_{out}} \tag{2.17}$$

where P_{out}^{sat} is the output saturation power, and $P_{out} = E[s_d^2]$ is the average input power.

2.1.2 Memoryless HPA Models

In this work we consider memoryless HPA models. In these models the output signal depends only on the current input, then no energy storing is considered.

Moreover, the following models are frequency flat, in other words they do not depend on the frequency of the input signal. Even if, practical HPAs are not absolutely memoryless, these models represent an appropriate and very used approach to model the effect of a real-world HPAs.

2.1.2.1 Ideal Clipping

The Ideal Clipping (IC), also known as Soft Limiter, is the memoryless model corresponding to the ideal case of perfect predistortion. In other words, we assume that the predistortion is able to perfectly compensate the nonlinearities due to the HPA up to the saturation point. In this case we have a linear transfer function before the saturation zone and an ideal clipping inside the saturation zone, thus its AM/AM and AM/PM characteristics are given respectively by:

$$F(\rho) = \begin{cases} \sqrt{G}\rho & \text{if } \rho \leq A_{sat} \\ \sqrt{G}A_{sat} & \text{if } \rho > A_{sat} \end{cases} \tag{2.18}$$

$$\Phi(\rho) = 0 \tag{2.19}$$

where A_{sat} is the saturation amplitude and G is the gain in linear zone. For simplicity we consider $G = 1$. Considering a complex Gaussian input, it is also possible to derive in closed form the expression of α as a function on IBO [15], [25]. From (2.10) the coefficient α is given by:

$$\alpha = 1 - \mathrm{e}^{-\mathrm{IBO}} + \frac{\sqrt{\pi \mathrm{IBO}}}{2} \operatorname{erfc}\left(\sqrt{\mathrm{IBO}}\right) \tag{2.20}$$

Similarly, for β we have [15], [25]:

$$\beta = 1 - \mathrm{e}^{-\mathrm{IBO}} \tag{2.21}$$

Using Eq. (2.15), we can derived the closed from of the SDR as a function of IBO

$$\mathrm{SDR} = \left(\frac{\beta}{\alpha^2} - 1\right)^{-1} = \left(\frac{1 - \mathrm{e}^{-\mathrm{IBO}}}{\left(1 - \mathrm{e}^{-\mathrm{IBO}} + \frac{\sqrt{\pi \mathrm{IBO}}}{2} \operatorname{erfc}\left(\sqrt{\mathrm{IBO}}\right)\right)^2} - 1\right)^{-1} \tag{2.22}$$

Note that in case of IC $\alpha \in \mathbb{R}$.

Furthermore, in case of IC and complex Gaussian input it is possible to express in closed form relationship between the input and the output powers [18]:

$$P_{out} = \left(1 - \mathrm{e}^{-\mathrm{IBO}}\right) P_{in} \tag{2.23}$$

Then substituting Eq. (2.17) in Eq. (2.23) we obtain the relationship closed form between the input and the output Back-off:

$$\mathrm{OBO} = \frac{\mathrm{IBO}}{1 - \mathrm{e}^{-\mathrm{IBO}}} \tag{2.24}$$

In Figure 2.4, we report the OBO as a function of IBO considering a complex Gaussian input signal, and different models of HPA.

2.1.2.2 Saleh Model

The Saleh model [26] is a common model for TWTAs (Travelling-Wave Tube Amplifiers), obtained through best-fit of experimental data. The AM/AM and AM/PM characteristics reported below:

$$F(\rho) = \frac{\alpha_A \, \rho}{1 + \beta_A \, \rho^2} \tag{2.25}$$

$$\Phi(\rho) = \frac{\alpha_\phi \, \rho^2}{1 + \beta_\phi \, \rho^2} \tag{2.26}$$

With an accurate choice of the parameter, α_A, β_A,α_ϕ, and β_ϕ the Saleh model can fit every TWTA. In [27] the following parameter values has been proposed: $\alpha_A = 1$, $\beta_A = 0.25$,$\alpha_\phi = 0.26$, and $\beta_\phi = 0.25$. Another common choice of parameters which is widely used in analytical studies is $\alpha_A = 2$, $\beta_A = 1$,$\alpha_\phi = 0.26$, and $\beta_\phi = 0.25$, in this manner the Eq. (2.25) and Eq. (2.26) are normalized in order to have the saturation point in $\rho = 1$, i.e. $F(1) = 1$. In Figure 2.2 we have report the AM/AM and AM/PM characteristics for different sets of parameters.

2.1.2.3 Rapp Model

Another well known and widely used model is the Rapp model [27]. It has been developed for Solid-State Power Amplifiers (SSPAs). The AM/AM and AM/PM characteristics reported below:

$$F(\rho) = \frac{\rho}{\sqrt[2p]{1 + \rho^{2p}}} \tag{2.27}$$

$$\Phi(\rho) = 0 \tag{2.28}$$

In this expression we have normalized the saturation level to 1. It presents a smoother AM/AM characteristic, while AM/PM perfectly linear. The parameter p is a smoothness factor. Note that if $p \to \infty$ then the Rapp model coincides with the Ideal Clipping. In Figure 2.3 we have report the AM/AM characteristic for different values of p.

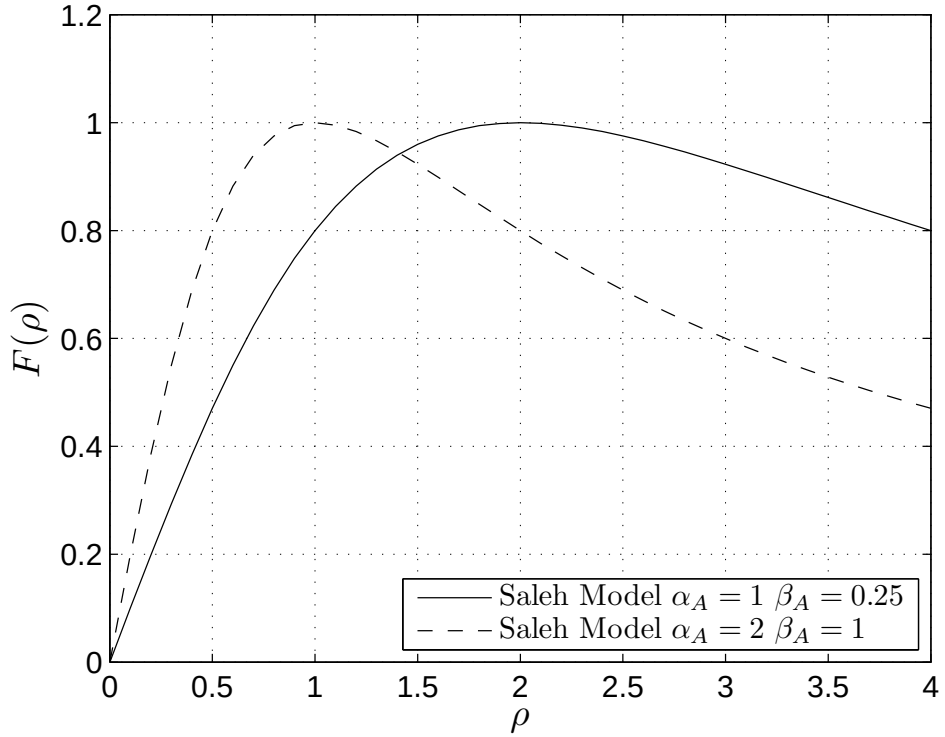

(a) AM/AM characteristic

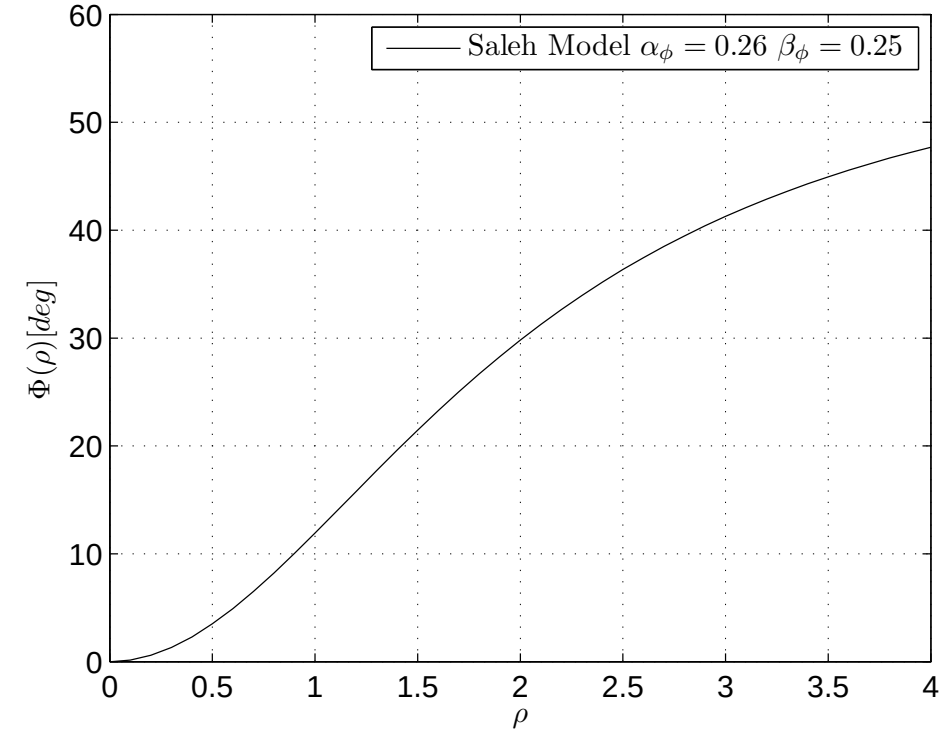

(b) AM/PM characteristic

Figure 2.2: Saleh Model

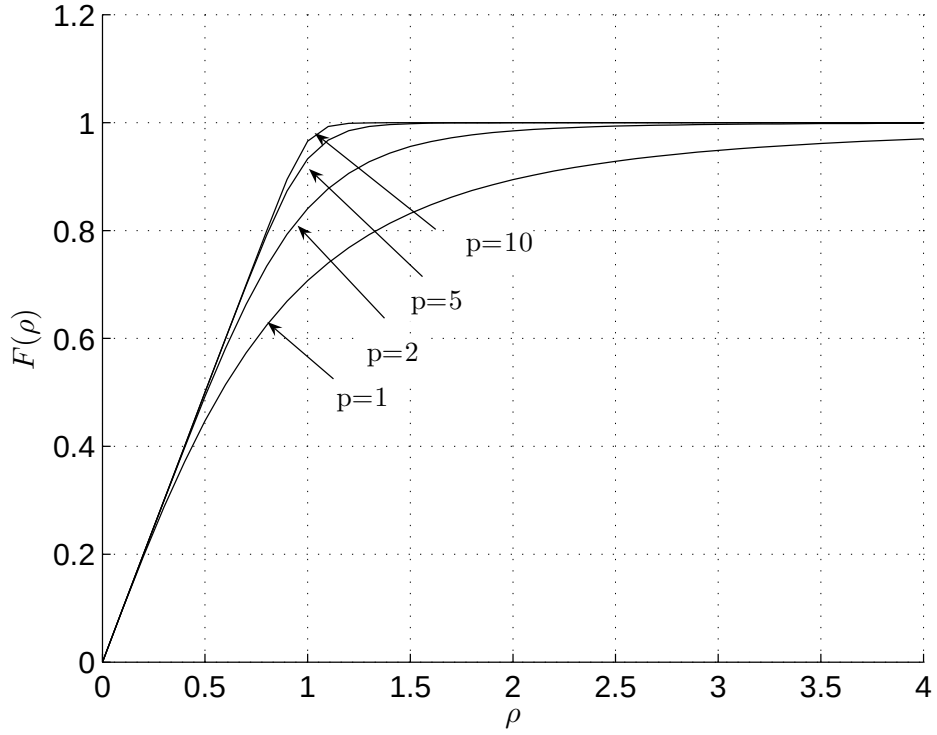

Figure 2.3: Rapp model: AM/AM characteristic for several values of p

It is worthwhile to note that, during the DVB-NGH standardization, the Rapp model with $p = 10$ as be used as a benchmark for the PAPR reduction techniques comparisons.

2.1.3 Effects of Nonlinear Distortion on the OFDM Signal

Since the low resilience to nonlinear distortion is a critical problem in OFDM systems, in the last years, the effects on nonlinearities on the OFDM signal has been thoroughly studied in literature, [15], [18], [16], [17]. If N is sufficiently large, the signal $s(t)$ expressed in Eq. (1.13) can be considerer as a Gaussian complex random process as a consequence of the central limit theorem. Bussgang's theorem guarantees that the signal s_d at the output of the nonlinear distortion, can be split in two terms: a linear term that is proportional to $s(t)$ according to a constant α, and a nonlinear distortion term, $d(t)$, that is a zero-mean (not Gaussian) process uncorrelated from $s(t)$:

$$s_d(t) = \alpha s(t) + d(t) \tag{2.29}$$

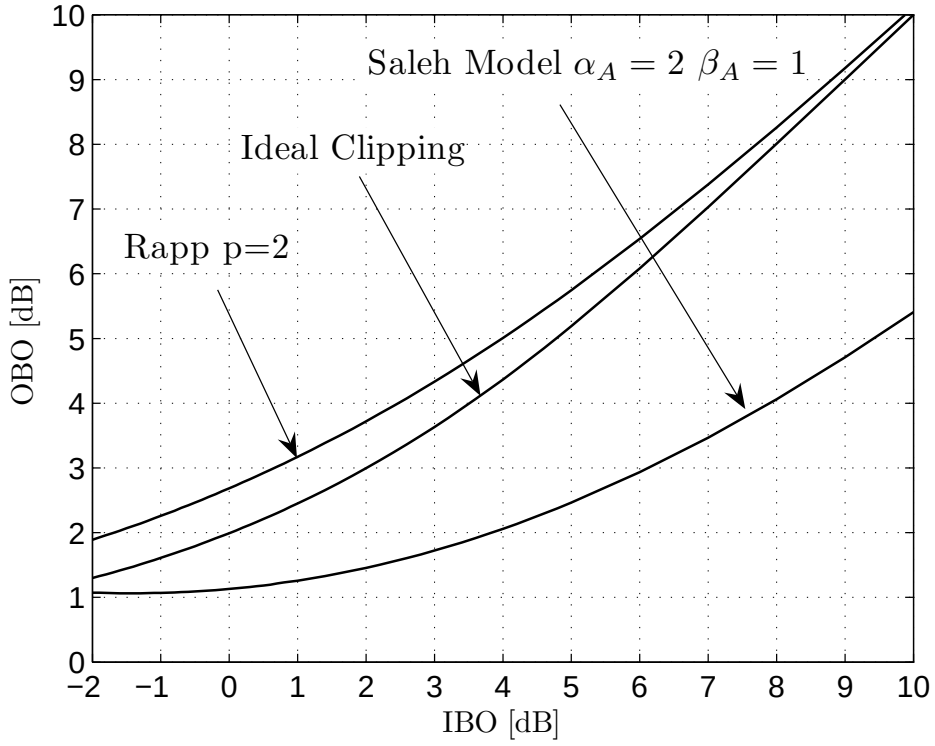

Figure 2.4: Output Back-Off as a function of the Input Back-Off considering a complex Gaussian input signal.

The signal $s_d(t)$ is transmitted over a time-varying frequency selective fading channel. The received signal expressed in Eq. (3.2) becomes:

$$r(t) = h(t) * (\alpha s(t) + d(t)) + n(t) \tag{2.30}$$

where $n(t)$ represents a Complex AWGN random process, with two-sided power spectral density equal to N_0. Filtering and sampling the received signal every T seconds yields:

$$r(uT) = \sum_j h_j(uT) \cdot \alpha s(uT - \tau_j) + d(uT - \tau_j) + n(uT) \tag{2.31}$$

Assuming that $h_j(t)$ remains constant over a OFDM symbol duration, the frequency domain OFDM symbol expressed in (3.2) becomes :

$$y_{k,\ell} = \frac{1}{\sqrt{N}} \sum_{i=0}^{N-1} r_{i,\ell} \cdot \mathrm{e}^{-\jmath\, 2\pi k i/N} \tag{2.32}$$

$$= H_{k,\ell}(\alpha x_{k,\ell} + D_{k,\ell}) + n_{k,\ell} \quad k = 0, \ldots, N-1 \tag{2.33}$$

2.2 Countermeasures to Nonlinear Distortion

Two approaches are usually considered to compensate the effects of nonlinear distortion: Predistortion and PAPR reduction. Note that these approaches are not mutually exclusive, and in the OFDM systems both of them are usually employed.

2.2.1 Predistortion

In the Predistortion techniques a block, named predistorter, which aim is to invert the HPA transfer function, is introduced before the HPA [28], [29], [30]. In other words, the cascade of predistorter and HPA should lead to a linear amplifier, at least in the signal dynamic range. This approach is commonly adopted, and its performances are quite interesting if the amplifier is conveniently driven far from its saturation point[1].

2.2.2 PAPR Reduction

The second approach, which is typically applied to OFDM systems, consists in reducing the fluctuations of the envelope of the signal, [32], [33]. In this way, the transmitted signal are not be excessively affected by the nonlinear distortion. The most common PAPR techniques presented in literature are Active Constellation Extensions (ACE), Tone Reservation (TR), and Selected Mapping (SLM), which are illustrate in Sections 2.2.2.1, 2.2.2.2, and 2.2.2.3 respectively. In Sections 2.3, we present a novel PAPR reduction technique named RISM yielding a quasi constant signal envelope in the time domain (PAPR close to 1 dB).

2.2.2.1 Active Constellation Extension

ACE method is based on the dynamically Extension of frequency domain constellation points [34]. This approach aim at reducing the time domain peaks of the signal without the insertion of overhead. The extended constellation points are moved from the borders of their Voronoi regions. The constellation extension is performed iteratively, according to the following procedure:

1. Start with the frequency domain representation of a OFDM symbol;

[1] A detailed analysis of predistortion techniques would be out of the scope of this manuscript. The interested reader is left to [31] and references therein.

2. Convert into the time-domain signal, and clip all samples exceeding a given magnitude V_{clip}. If no sample is clipped, then exit;

3. Re-convert into the frequency domain representation and restore all constellation points which have been moved towards the borders of their Voronoi regions;

4. Go back to 2 until a fixed number of iteration is reached;

This algorithm is applied to data carriers only, excluding thus pilots, preamble, signalling and guard bands. The effectiveness of ACE strongly depends of the cardinality of the constellations: In case of QPSK, ACE present the best PAPR performance becuase every point can be moved to the outer part of their Voronoi region. In case of 16QAM, only the most external point can be moved, hence the capability of the PAPR reduction method results limited.

2.2.2.2 Tone Reservation

TR technique operates in the time domain, trying to cancel the highest peak using a additive signal named Kernel [35], [36]. The kernel signal is a MMSE approximation of Dirac delta and its spectral content is present only in a certain number of given reserved subcarriers. The MMSE approach to construct a pulse close to the discrete Dirac delta is to have a flat spectrum only on the allowed carriers and zero otherwise. Once obtained this Kernel signal, it is shifted in time, in order to be centered on the peak of the time domain signal. While the Kernel amplitude and phase are computed in order to reduce the value of the peak to a chosen target value. This peak cancelation is performed iteratively as follows:

1. Start with the time domain representation of a OFDM symbol;

2. The kernel amplitude and phase are scaled in order to reduce the signal peak to the chosen target value V_{clip}.;

3. The kernel peak is aligned to the signal peak by a time shift.

4. the kernel is summed to the signal. This operation reduces the current signal peak to the target V_{clip}.

5. If there is another peak having amplitude greater than V_{clip} than go back to 2 else transmit the sum of signal and kernel;

Differently from ACE, the PAPR performance does not depend od the constellation order, because TR operates only on some reserved tones. However, this methods requires the insertion of additional overhead, and clearly the more the reserved tones used to create the Kernel signal the better the PAPR performance.

2.2.2.3 Selected Mapping

SLM technique represents a probabilistic approach to PAPR reduction: a certain number of equivalent data symbol vectors are generated, and the one with the lowest PAPR is chosen. The generation of these "candidates" is done by the multiplication of the original data symbol vector for different vectors composed of phase shifts. In order to simplify the signal processing, the phase shift considered will be multiples of $\pi/2$. This means that the signal will be multiplied for vector composed with the symbols $1, j, -1, -j$. Then the IFFT of all these equivalent representation is computed, and the sequence with the lowest PAPR is transmitted, joint with the number of the sequence used (in the scenario we have considered, 8 sequences have proved to reduce enough the PAPR. Although this approach, described in [37] requires only a few bits of overhead, in [38] the Authors propose the use of scrambling instead of multiplication for a pseudo-random sequence. The advantage of this method is that no side information is required, because a receiver with adequate processing capability could perform all the possible scramblings and recognize the correct one due to certain characteristics of the signal (the presence of pilots, preambles, etc.)

2.2.2.4 Quasi-Constant Envelope OFDM

Using the previously mentioned methods the PAPR can be kept moderately low, with a reduction of several dB with respect to the original signal. However a mild PAPR reduction could not be sufficient to guarantee a proper OFDM reception in presence of a severe nonlinear channel.

On the other hand, a OFDM signal having a very small dynamics can be efficiently employed in highly distorting scenarios, such as satellite links or in the presence of nonideal HPA driver circuits. Therefore all the advantages of the OFDM modulation will be preserved adding further resilience to nonlinear distortion. For this reason, our purpose here is to obtain a dramatic PAPR reduction, which yields to a quasi-constant OFDM envelope, in order to make the OFDM reception feasible even in those scenarios characterized by severe nonlinearities. In particular, we aim

at keeping the PAPR around $1-2$ dB which corresponds to a reduction of almost 10 dB with respect to the original signal. In order to achieve such an ambitious purpose, in Section 2.3 we introduce a novel PAPR reduction technique based on a *open* data mapping which, by exploiting some of its degrees of freedom and using an optimization process, leads to a quasi-constant envelope. Clearly, there is a trade off between the amount of flexibility that the *open* data mapping exploits to reduce the PAPR and robustness to Gaussian noise, as well as its spectral efficiency. For this reason, we also propose some different kind of open data mappings that represent different compromises between PAPR reduction and Gaussian noise robustness.

2.3 Rotation-Invariant Subcarrier Mapping

In this Section we introduce a PAPR Reduction method based on the novel concept of Rotation-Invariant Subcarrier Mapping. In the RISM tones the symbols alphabet is not anchored into a classic constellation, but it maintains some degrees of freedom. The final positions of the transmitted symbols are chosen by an optimization process aiming to decrease the overall OFDM symbol PAPR. If RISM is used over all the active subcarriers a massive PAPR reduction is obtained yielding a quasi-constant envelope OFDM signal. Alternately, as illustrated in details in Section 2.3.4.1, RISM can be also used only over a subset of the active subcarriers in order to enable an higher spectral efficiency.

In the following Sections 2.3.1.1 and 2.3.1.2, we describe RISM constellations which are able to convey respectively one and two information bits, then in Section 2.3.2 we illustrate the RISM iterative optimization algorithms which act on the signal in order to decrease the PAPR of the resulting OFDM symbol.

2.3.1 RISM Mapping Schemes

2.3.1.1 Two-Level RISM Mapping

The first RISM scheme we propose is a two-level data mapping, illustrated in Figure 2.5, where the bit '0' is mapped in zero and the bit '1' can be mapped in any point of the circle with radius $\sqrt{2E_s}$ and centered in zero, this yields:

$$x_{k,\ell} = \begin{cases} 0 & \text{if } b_{k,\ell} = 0 \\ \sqrt{2E_s}\mathrm{e}^{\jmath\phi_k} & \text{if } b_{k,\ell} = 1 \end{cases} \tag{2.34}$$

where $b_{k,\ell}$ is the k-th bit to be mapped, E_s is the symbol energy, and the values of

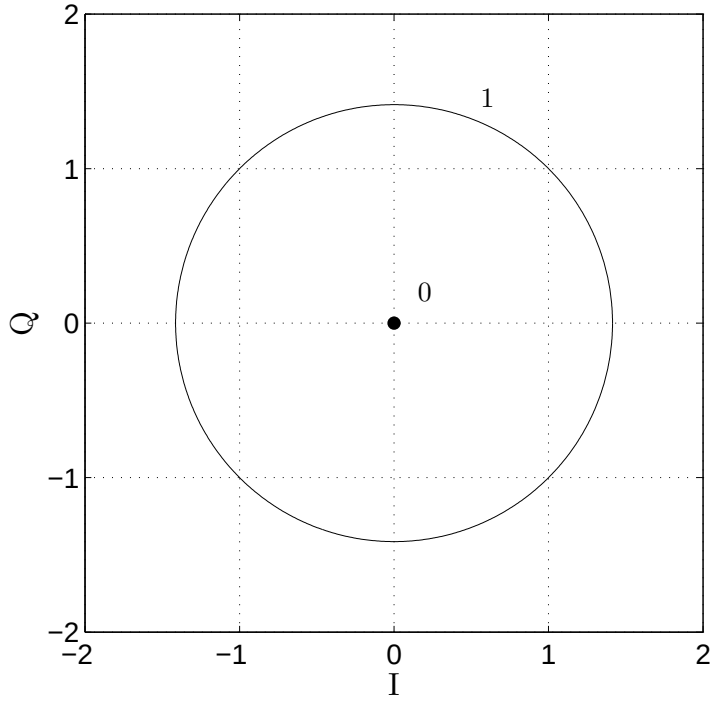

Figure 2.5: 2-level RISM Mapping.

$\phi_{k,\ell}$ will be optimized according to the algorithm described in the Section 2.3.2.

2.3.1.2 Four-Level RISM Mapping

A straightforward extension of the aforementioned mapping which convey 2 bit per symbol, it is composed by the origin and three rings. Using this scheme we can increase the spectral efficiency while keeping a very large flexibility to Reduce the PAPR. Unfortunately this scheme present a low resilience against thermal noise.

In order to overcome this problem, we propose another RISM scheme which can convey 2 bits per symbol and at the same time ensures an increased distance between points, is the so-called Clover mapping. This scheme represents a good trade off between the amount of flexibility that the RISM exploits to reduce the PAPR and its robustness to Gaussian noise, is represented by the solution depicted in Figure 2.6. As shown, the couple '00' is mapped the origin, while the remaining couples are mapped respectively onto the geometrical loci corresponding to the three equidistant circular arcs with radius $\sqrt{\frac{4}{3}E_s}$ centered in zero. Numerical results shows that this solution represents the best tradeoff between PAPR reduction

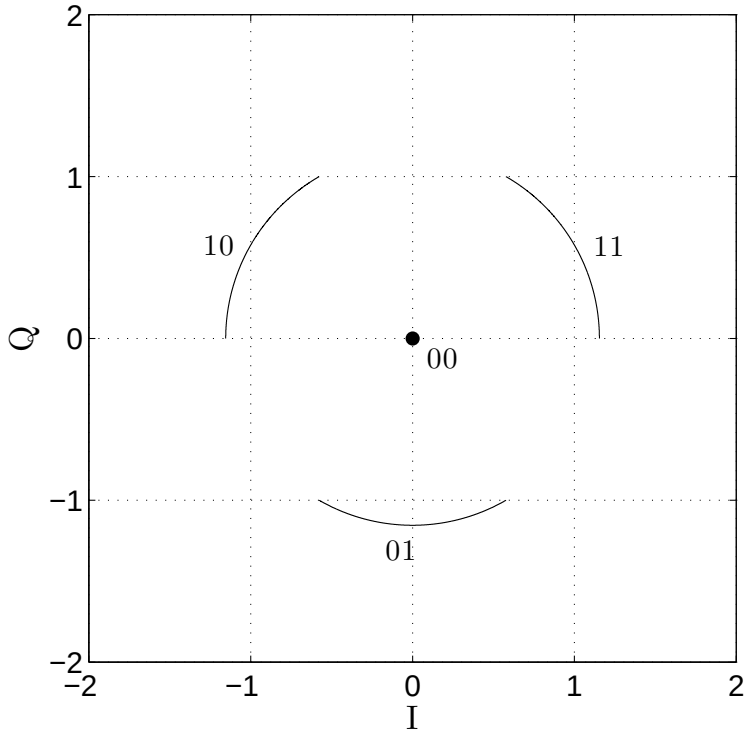

Figure 2.6: 4-level RISM Mapping.

and thermal noise resilience. Furthermore, it is also possible optimize the amplitude of the circular arcs, in order to achieve different trade-offs between Gaussian noise immunity and PAPR reduction.

2.3.2 RISM Iterative Optimization

In this Section we describe two different iterative optimization algorithms which arrange the phases ϕ_k in order to decrease the PAPR of the resulting OFDM symbol. Both of them work alternating time and frequency domain and converge to the same results. But the low-complex version of the algorithm is characterized by a(at least) ten-time faster convergence.

Therefore it is convenient to use the low-complex version of iterative optimization, nevertheless, for completeness we illustrate also the first version of the algorithm. The first version of the algorithm is characterized by the following parameters: the number of iterations,N_{iter}, and is the clipping level, ξ_{clip}. This iterative algorithm works alternately in time and frequency domain as follows:

1. RISM Data Mapping: The bits are mapped in RISM subcarriers, forming the vector $\bar{x}(0) = (x_{0,\ell}, \ldots, x_{N-1,\ell})$. The index in bracket indicates the current iteration number. The initial phases are chosen randomly.

2. The time domain OFDM signal, $\bar{s}(l)$ is obtained through an IFFT.

3. The time domain samples exceeding ξ_{clip} are clipped, obtaining the distorted signal $\bar{s}^d(l)$

4. The distorted signal in frequency domain, $\bar{x}^d(l)$, is obtained by an FFT

5. The RISM mapping is reinstalled: In this way we obtain the frequency domain OFDM signal at the $(l+1)$-th iteration, $\bar{x}(l+1)$.

6. If the OFDM signal has reached a given PAPR target or if the maximum number of iteration has been reached, the procedure exits, otherwise it returns to the step 2.

These operations are repeated N_{iter} times or alternately can be stopped when no time domain samples $s_{i,\ell}$ exceed, in absolute value, a threshold ξ. This algorithm can be seen as an extension of the ACE [34]. The main difference is that the RISM iterative optimization moves the complex data $x_{k,\ell}$ only acting on their phase. In this way the energy of each complex data $x_{k,\ell}$ remains constant, and the distance among the points of constellation is equal.

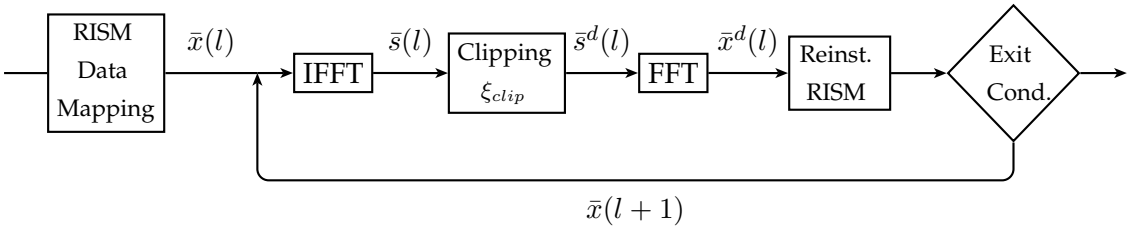

Figure 2.7: Block Diagram of the RISM Iterative Optimization

In order to maximize the benefits of the RISM a iterative optimization may have a slow convergence. For this reason we propose an alternative optimization procedure which is able to converge in a smaller number of iterations. In this way, we achieve PAPR reduction, and keep complexity well under control. The low-complexity iterative algorithm operate as follows:

1. RISM Data Mapping: The bits are mapped in RISM subcarriers, forming the vector $\bar{x}(0) = (x_{0,\ell}, \ldots, x_{N-1,\ell})$. The index in bracket indicates the current iteration number. The initial phases are chosen randomly.

2. The time domain OFDM signal, $\bar{s}(l)$ is obtained through an IFFT.

3. The time domain samples exceeding ξ_{clip} are clipped, obtaining the distorted signal $\bar{s}^d(l)$ and the difference signal $\bar{d}(l)$.

4. The difference signal in the frequency domain, $\bar{D}(l)$, is obtained using a FFT. Note that, being $\bar{d}(l)$ a sparse vector, $\bar{D}(l)$ may be obtained with lower complexity.

5. The frequency domain difference signal $\bar{D}(l)$ is multiplied by μ, and added to the original frequency domain signal, $\bar{x}(l)$.

6. The reinstalling process is starting from the signal $\bar{x}(l) + \mu\, \bar{D}(l)$. we obtain the frequency domain OFDM signal at the $(l+1)$-th iteration, $\bar{x}(l+1)$.

7. If the OFDM signal has reached a given PAPR target or if the maximum number of iteration has been reached, the procedure exits, otherwise it returns to the step 2.

It worthwhile to note that the parameter μ resembles the use of a step parameter in gradient based optimization.

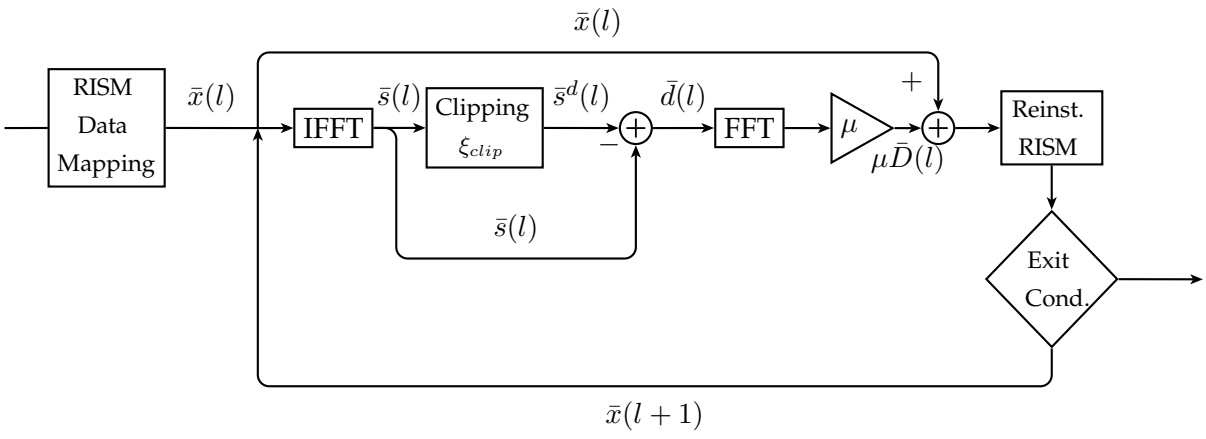

Figure 2.8: Block Diagram of the Low-Complex RISM Iterative Optimization

2.3.3 RISM Detectors

In this Section, first we propose the detection scheme for RISM, and secondly we analyze analytically the performance of the proposed mapping schemes. The analytical assessment hereby presented is based on a AWGN channel. This is convenient for analytical simplicity and does not affect the generality of the discussion, since the effect of the HPA distortion can be modelled as a scaling of the useful signal and an additional noise source. Under these assumptions Eq. (1.18) becomes

$$y_{k,l} = x_{k,l} + n_{k,l} \tag{2.35}$$

For the two-level RISM described by Eq. (2.34) the envelope of the received signal can be modelled as a Rayleigh random variable if $b_k = 0$ and a Rice r.v. if $b_k = 1$. Letting ρ_y be the envelope of the received signal, we have:

$$p_{\rho_y}(\rho_y) = \begin{cases} \frac{2\rho_y}{N_0} \mathrm{e}^{-\frac{2\rho_y^2}{N_0}} & \text{if } b_k = 0 \\ \frac{2\rho_y}{N_0} \mathrm{e}^{-\frac{\rho_y^2+2E_s}{N_0}} I_0\left(\frac{2\rho_y\sqrt{2E_s}}{N_0}\right) & \text{if } b_k = 1 \end{cases} \tag{2.36}$$

where we have dropped the subscript k, l for the sake of readability. The energy detector can be efficiently employed for this problem: the randomness of the phase due to RISM Iterative Optimization inhibits the use of a coherent detector, and the energy detector is both robust and simple. The threshold ζ on the received signal can thus be calculated by the ML criterion (equal symbol a priori probability and equal cost of the errors), leading to the following nonlinear equation

$$p_{\rho_y|b_k=1}(\zeta|b_k = 1) = p_{\rho_y|b_k=0}(\zeta|b_k = 0) \tag{2.37}$$

the corresponding solution can be found numerically. Once the value for the threshold ζ is obtained, the error probability can be written as

$$P_e = \frac{1}{2}\left[1 - Q_1\left(\sqrt{\frac{E_b}{N_0}}, \sqrt{\frac{2}{N_0}}\zeta\right) + \mathrm{e}^{-\frac{\zeta^2}{N_0}}\right] \tag{2.38}$$

where $Q_1(a, b)$ is the Marcum Q function [39]. In the case of a transmission impaired by a distorting HPA, the noise term must include also the effect of the HPA (the term $D_{k,l}$) in Eq. (2.32) The shape of the decision regions for 2-level RISM mapping are shown in Figure 2.9

Regarding the 4-level RISM case, the optimal detection problem is analytically involved. Practical sub-optimal detection can be performed in two steps: in the first

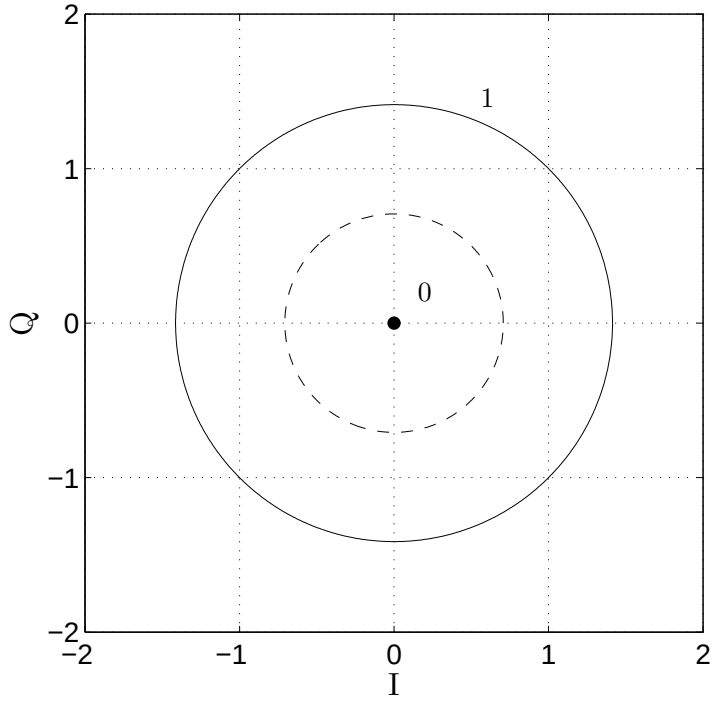

Figure 2.9: Decision regions for 2-level RISM.

step we establish whether the received symbol belongs to the external ring. In this stage an energy detector is again employed, using the ML criterion to compute the threshold. Once this first step has been performed, in case the signal does belong to the outer ring, a phase detector is employed. The decision regions obtained by the aforementioned method are shown in Figure 2.10 Summarizing, Figure 2.11 shows the AWGN performance of both 2-level and 4-level RISM.

2.3.4 Hybrid RISM

The key idea under the Hybrid RISM technique is basically to multiplex in the same OFDM symbols, both QAM and RISM subcarriers. In this way we can exploit the RISM tones in order to reduce the overall PAPR, and, at the same time, we can also achieving an higher spectral efficiency using higher modulation orders on the QAM subcarriers. Clearly the effectiveness of the Hybrid RISM technique in term of PAPR reduction depends on the number of RISM subcarriers inserted in the ODFM symbol. Let us assume to insert RISM tones in the OFDM symbols with a density, R_d. In other words, we are assuming that every OFDM symbol contains

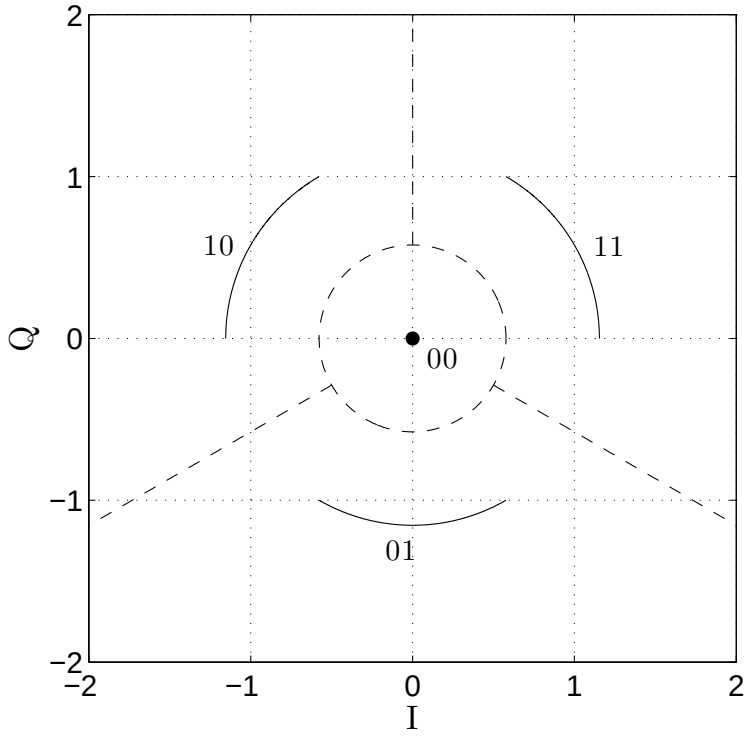

Figure 2.10: Decision Regions for 4-level Mapping.

$N_a R_d$ RISM tones, and $N_a(1-R_d)$ QAM tones. Clearly the higher the RISM density R_d, the more evident the PAPR reduction. This behavior is clearly illustrated in Figures 2.15 and 2.16, where Hybrid RISM performance are shown using 2-level and 4-level RISM respectively.

Numerical results show that similar performance is achieved using regular or random positioning of the RISM tones over the OFDM comb. On the other hand the optimum set of parameter of the iterative optimization (i.e μ, ξ_{clip}, N_{iter}) depends of R_d. In general the lower the density the higher the PAPR target and then the higher the ξ_{clip}.

2.3.4.1 Practical Case: RISM over DVB-T2 Reserved Tones

In the DVB-T2 standard the TR technique illustrated in Section 2.2.2.2 has been adopted as a PAPR technique. Consequently DVB-T2 provides a specific pattern of reserves subcarriers which are occupied by the tone composing the kernel signal. In particular, in DVB-T2 the percentage of the reserved tones over all the active

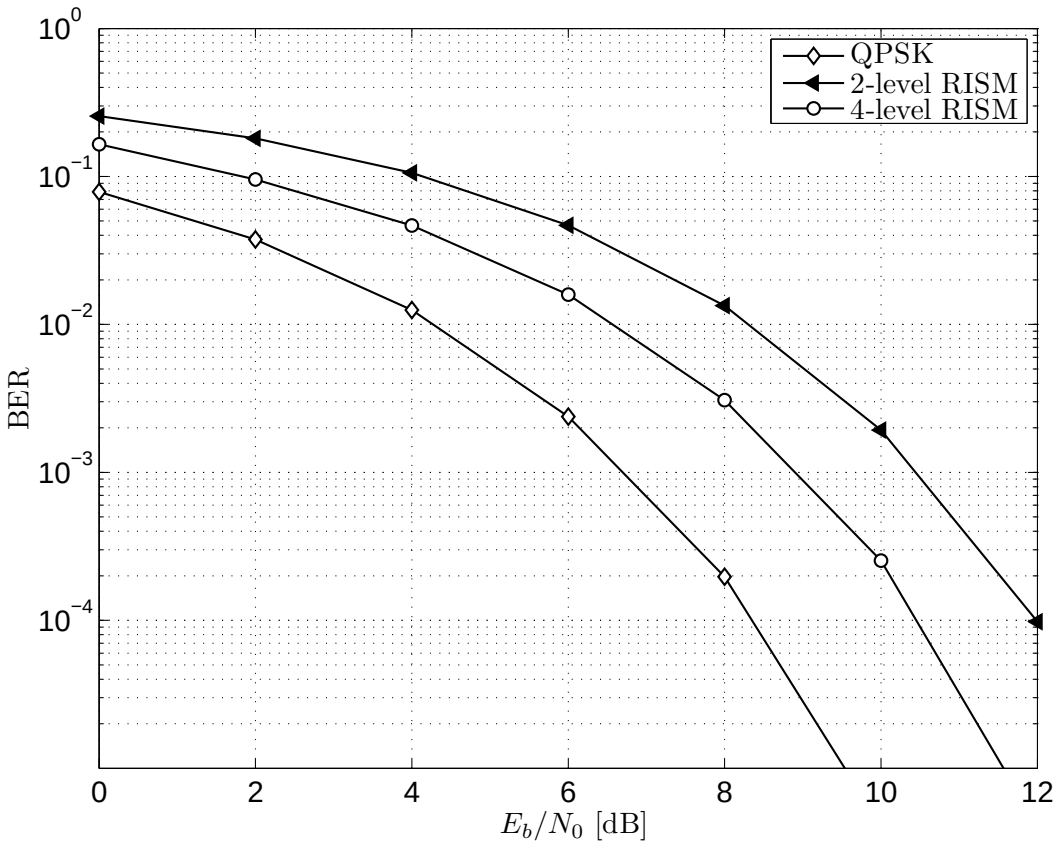

Figure 2.11: BER Performance in linear channel

subcarriers is about 1 %. Of course, at the receiver, the received reserved tones are discarded.

Let us assume to use RISM tones over the pattern of reserves subcarriers specified by DVB-T2. In other words, Hybrid RISM can be used as alternative to TR, which is also able to convey additional information on the reserved tones. This additional capacity can be used whether to convey data or signaling information.

For instance, the OFDM symbol indexing signals, which are not originally provided in the DVB-T2 frame structure could be carried using the RISM tones over reserved tones. In this manner, the OFDM symbol indexing will be provided to the receiver without altering the original DVB-T2 frame structure. Clearly this change is completely backward compatible. Older receivers which do not support this feature will see the RISM tones as normal reserved tones.

At the time of writing the author is involved in the standardization group of the DVB-NGH, where the adoption of the Hybrid RISM tones over reserved tones

specified by DVB-T2 is under consideration. From numerical analysis reported in [40] and in [41], it has been shown that Hybrid RISM reach about the same performance compared with the specified TR technique using the same toner reservation pattern.

2.4 Numerical Results

The purpose of this Section is threefold: first we assess the PAPR reduction performance showing that it is possible to obtain a quasi-constant OFDM envelope using RISM; second we present the system performance in terms of Bit Error Rate (BER) taking into account two different models of nonlinear HPA, i.e. Ideal Clipping and Saleh model; third we show the numerical results in terms of Total Degradation (TD) which is it defined as the sum of OBO and the SNR loss due to nonlinearity. We assess the performance of 2-level RISM, 4-level (Clover) RISM, and Hybrid RISM case with several values of RISM density R_d. We consider OFDM signal having $N = 2048$, and QPSK modulation as benchmark case, which is traditionally considered as the optimum compromise between robustness and spectral efficiency.

2.4.1 PAPR Reduction Performance

As a first result, we present the distribution of PAPR for RISM-OFDM and QPSK-OFDM. The statistical characterization is done by means of the Complementary Cumulative Density Function (CCDF), which represents the probability that the PAPR exceeds a given value. More specifically, Figures 2.12 and 2.13 show the impact of the clipping level used in the circular optimization procedure. We numerically derive that the best clipping level ξ_{clip} for 2-level and 4-level RISM are 1 dB and 2.2 dB respectively. Figure 2.14 reports the comparison between RISM and QPSK. As it is shown RISM approach enables a dramatic reduction in PAPR compared with the traditional QPSK-OFDM case. This dramatic PAPR reduction introduced by RISM, which yields PAPR values comparable with those obtained in single-carrier systems, guarantee high robustness of the signal even with an highly distorting HPA. Furthermore in Figure 2.15 we report the PAPR performance for 2-level Hybrid-RISM for different values of the RISM tone density. It is shown that, even using a very low density of RISM tones, such as, $R_d = 1/32$ and $R_d = 1/64$, a PAPR reduction of 2 and 1 dB respectively is achieved. Furthermore in Figure 2.16

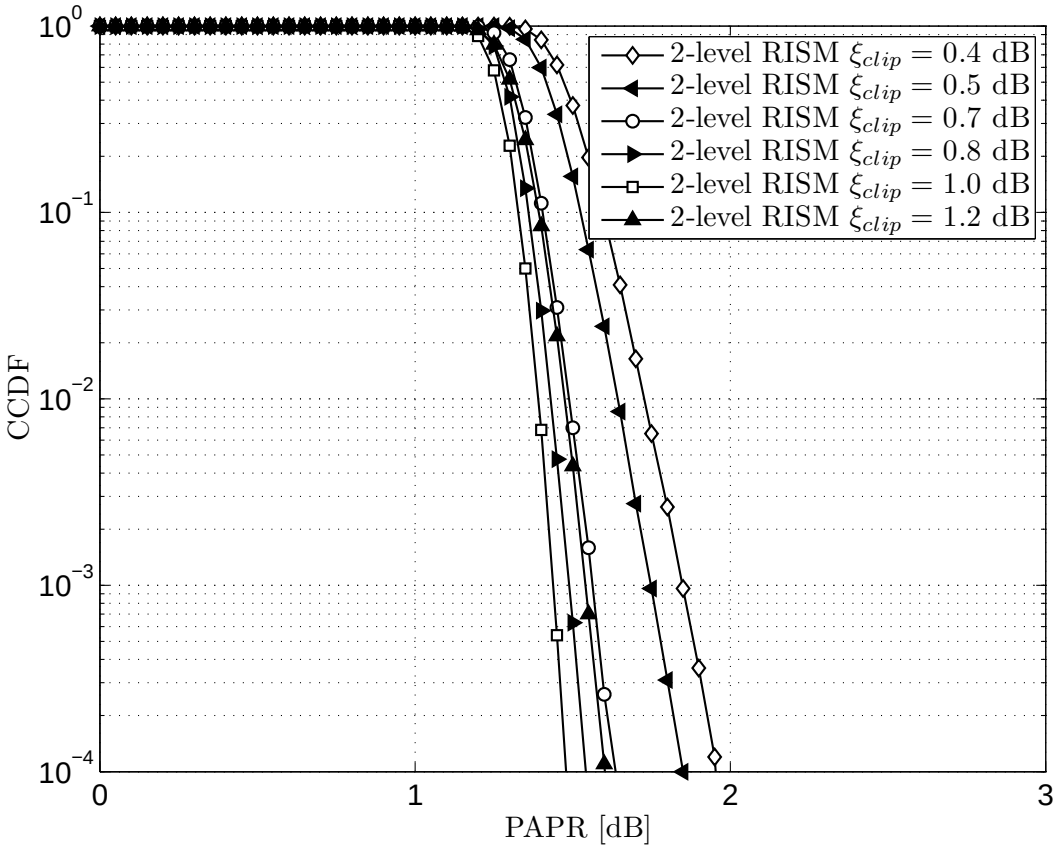

Figure 2.12: PAPR performance for 2-level RISM using different clip level values.

we report the PAPR performance for 4-level Hybrid-RISM for different values of the RISM tone density. In this case a RISM density higher that $R_d = 1/32$ must be used in order to ensure a PAPR reduction of at least 2 dB.

2.4.2 Bit Error Rate over Nonlinear Channels

The evaluation of the BER is performed considering two practical nonlinear channels. In particular we consider the case of an ideal predistortion which leads to the IC model, and the case of using a TWT amplifier without any predistortion, which is modelled by the Saleh model. In both cases, we assume IBO $= 0$ dB, and that the phase offset due to the nonlinear device is ideally recovered. Figure 2.17 shows that in case of TWTA, 2-level RISM approach guarantees better performance compared with the case of OFDM-QPSK, avoiding any error floor, while in the case of ideal predistortion, shown in Figure 2.18, 4-level RISM outperforms 2-level RISM for low SNR and QPSK for high SNR. Therefore we conclude that in case of heavy

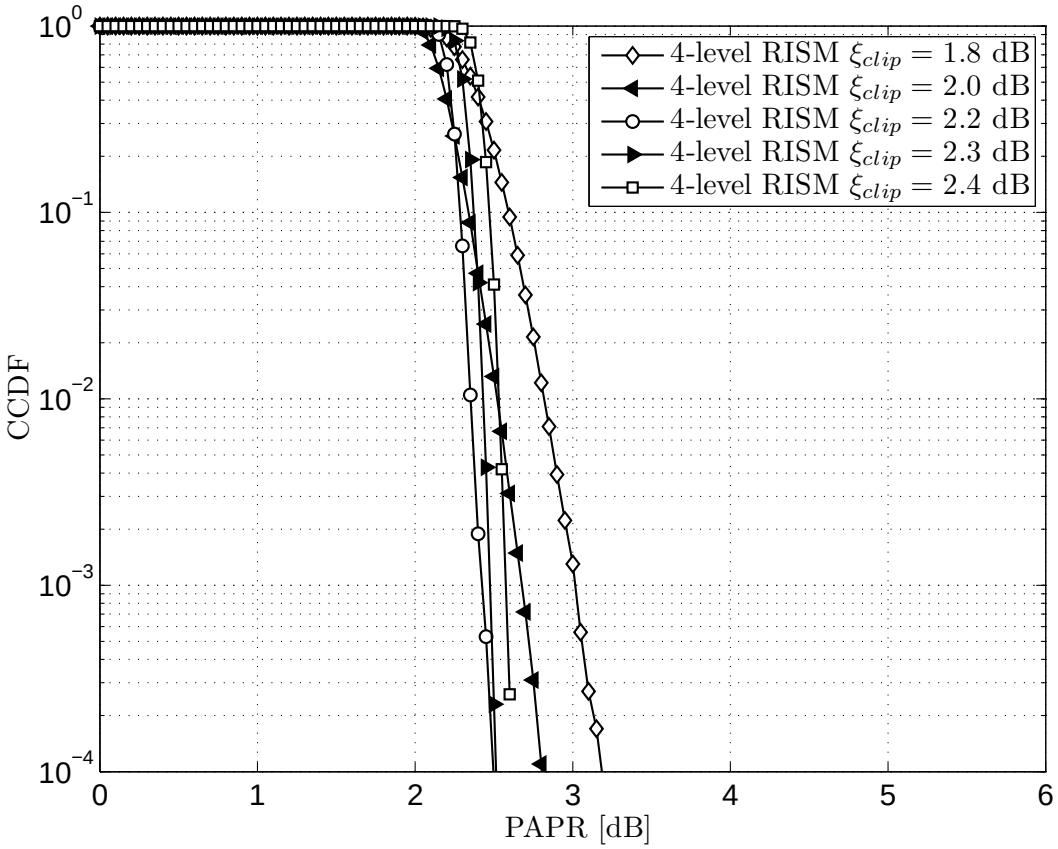

Figure 2.13: PAPR performance for 4-level RISM using different clip level values.

distorting conditions the 2-level RISM can allow a satisfactory reception, on the other hand 4-level RISM represents a good trade-off between nonlinear resilience, spectral efficiency and minimum Euclidian distance. In an intermediate case, i.e. in the case of a linearized amplifier (which behavior is still far from the case of ideal predistortion), we logically expect this novel method to perform in an intermediate way between the results shown in Figures 2.17 and 2.18.

2.4.3 Total Degradation

A figure of merit which has been proven to be very suitable to asses the overall system performance over nonlinear channels is the Total Degradation [42]. It is defined as:

$$\mathrm{TD} \doteq \mathrm{OBO}\ \delta_{\mathrm{SNR}} \tag{2.39}$$

where OBO is the Output Back-off defined in Eq. (2.17), and δ_{SNR} is the SNR loss due to the nonlinear distortion introduced by the HPA.

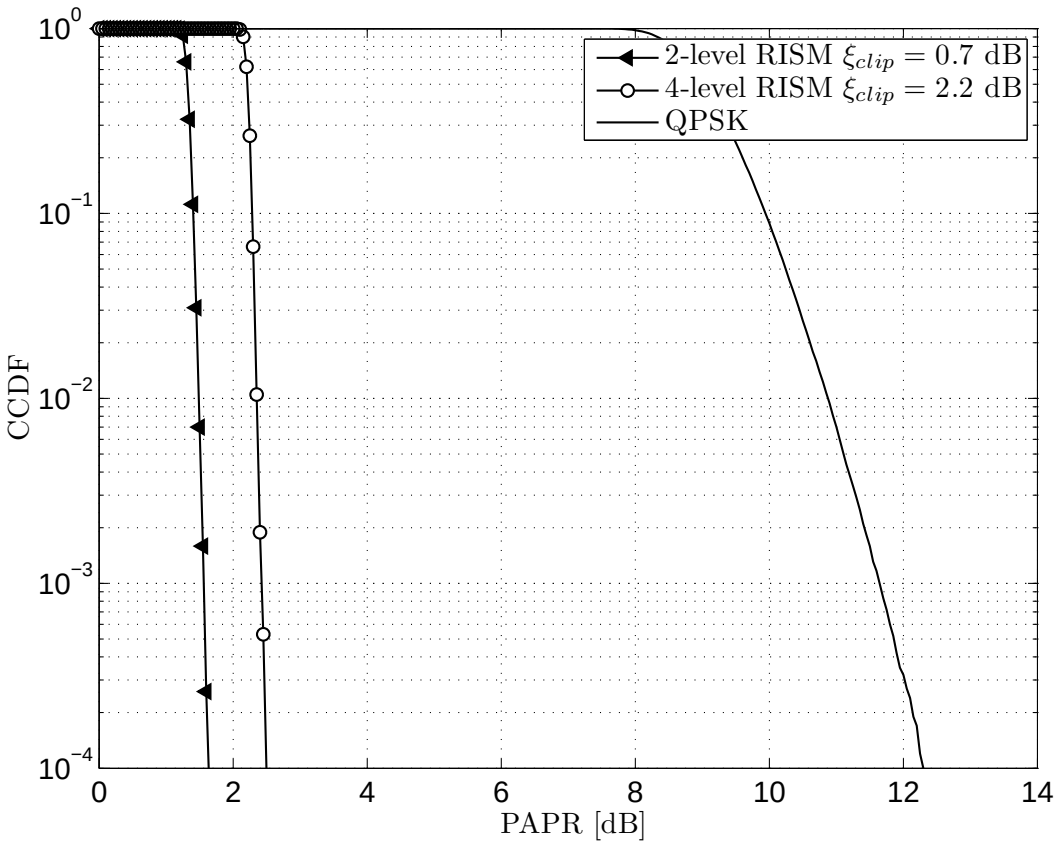

Figure 2.14: PAPR Comparison between OFDM-QPSK, 2-level and 4-level RISM.

In other words, δ_{SNR} can be seen as the power boosting of the signal which is needed to compensate the effects of nonlinear distortions and achieve target performance BER_{req}. Let us define SNR_{req} as the required SNR to achieve the target performance BER_{req} in linear conditions.

Figure 2.19 reports the performance in terms of TD, plotted in solid lines. As it is shown, both 2-level and 4-level RISM technique reach the total insensitivity to nonlinearity effects, which is represented by the line $\mathrm{TD} = \mathrm{OBO}$, even with low values of OBO. In order to provide a complete and fair comparison, we consider a new definition of Total Degradation, TD′ including a further term which takes into account the performance gap between RISM and QPSK over a linear channel.

$$\mathrm{TD}' \doteq \mathrm{OBO}\ \delta_{\mathrm{SNR}}\ \delta_{QPSK} \tag{2.40}$$

where the last term is the SNR loss, over a linear channel, of RISM with respect to QPSK at $\mathrm{BER} = \mathrm{BER}_{req}$. Note that, for all the RISM schemes we have $\delta_{\mathrm{SNR}} \approx 0\ dB$ and obviously $\delta_{QPSK} > 0\ dB$, thus the comparison in terms of TD′ is more fa-

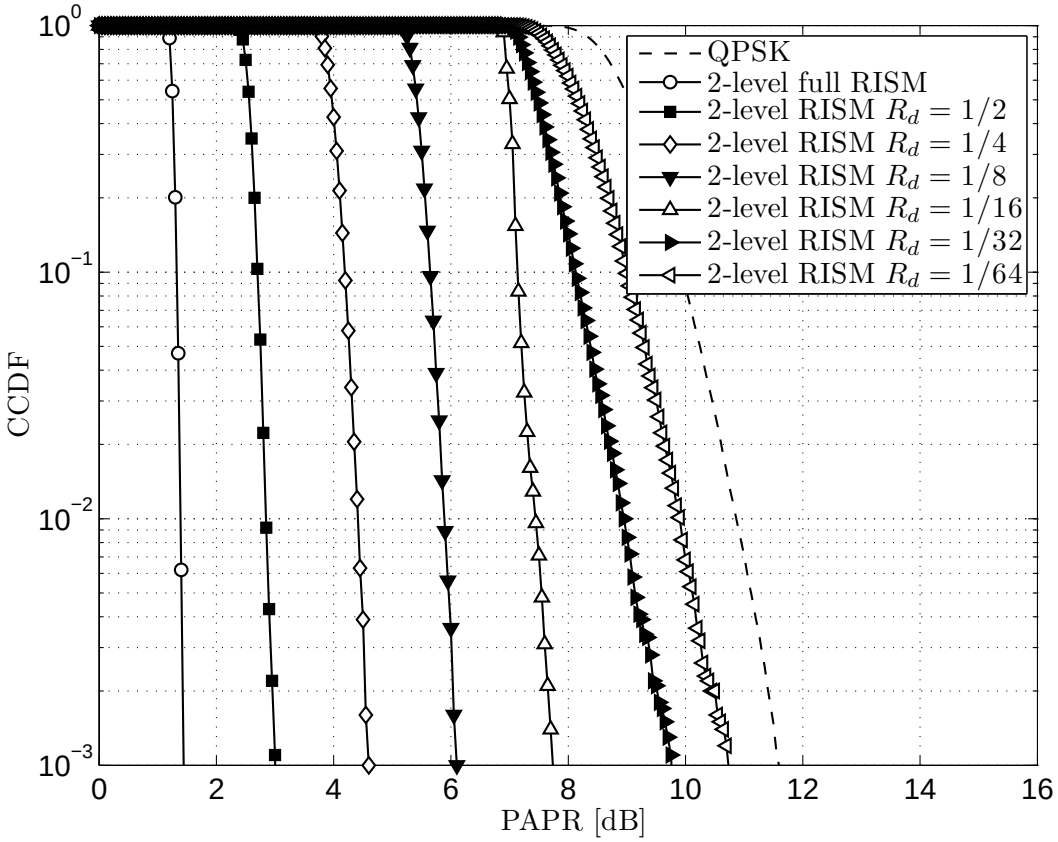

Figure 2.15: PAPR performance for 2-level Hybrid-RISM for different values of the RISM tone density.

vorable to QPSK case. In Figure 2.19, the performance in terms of TD and TD′ considering Saleh HPA model are plotted in solid and dotted lines respectively. Note that, all the considered schemes reach roughly the same minimum degradation, $\min_{OBO}$ TD′ $\approx 5dB$. However RISM schemes have two important advantages compared with QPSK:

- The minimum degradation is reached at much lower value of OBO compared with QPSK case;
- TD′ function is almost flat around its minimum.

These are significant advantages even if the amplifier is linearized: in a practical scenario, it is not possible to perfectly control the actual value of the operating point due to a non-ideality of the HPA driver circuits, and to amplifier instabilities. In fact, some studies carried out by manufacturers [43] show that that in practical

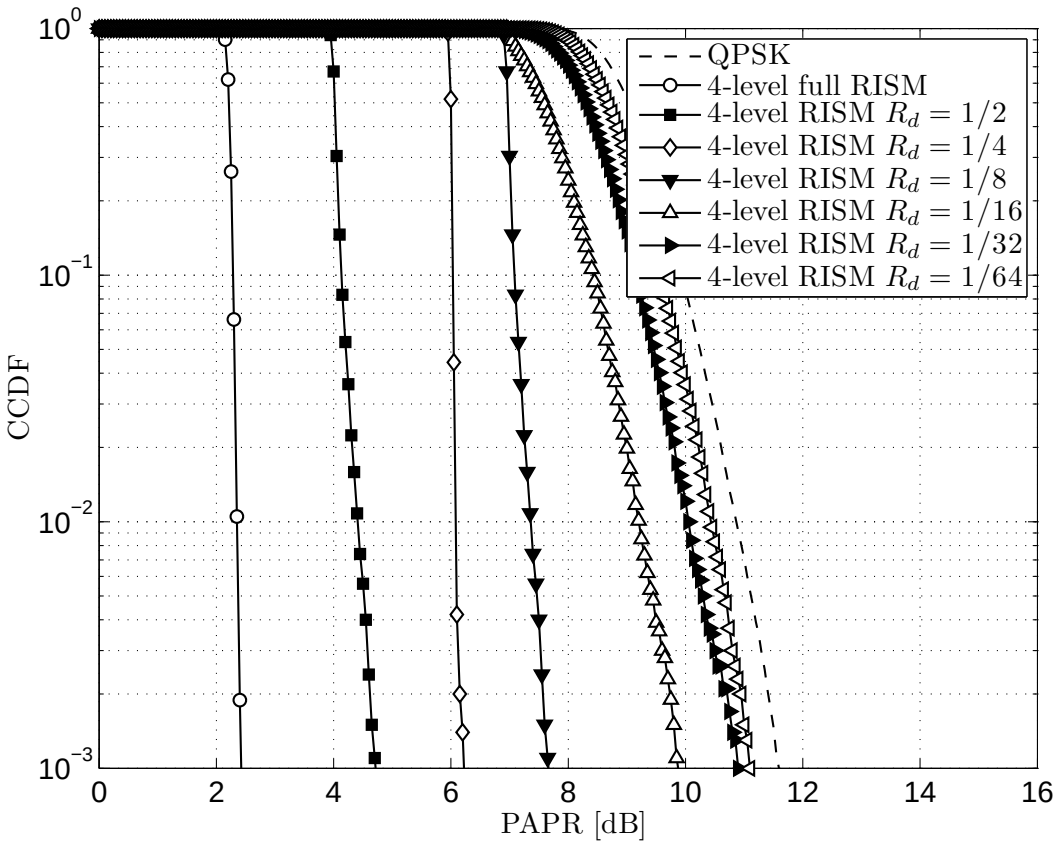

Figure 2.16: PAPR performance for 4-level Hybrid-RISM for different values of the RISM tone density.

cases OBO is not finely tunable, in fact can be controlled within a tolerance of 3 dB. For these reasons, it is crucial to keep the total degradation function low for all the possible range of OBO. As shown in Figure 2.19, by using RISM schemes we are able to fully satisfy this condition. Instead using QPSK we obtain low TD′ only for high value of OBO.

Regarding the Hybrid RISM technique, the TD performance are reported in Figures 2.25 - 2.33. We asses the TD with different SNR_{req} values: 0, 4, and 8 dB, respectively, in order to represent different modulation and coding (MOD-COD) configurations. In the following plots, the OBO and the TD values has been computing considering a IBO range that goes from -2 db to 10 dB. As we can see from figures 2.2 and 2.4, in case of Saleh model the relation between OBO and IBO is not strictly monotonic. Therefore, in the curves plotted in figures 2.27, 2.30, and 2.33, a value of OBO may be correspond with two different values of TD. Thus, the

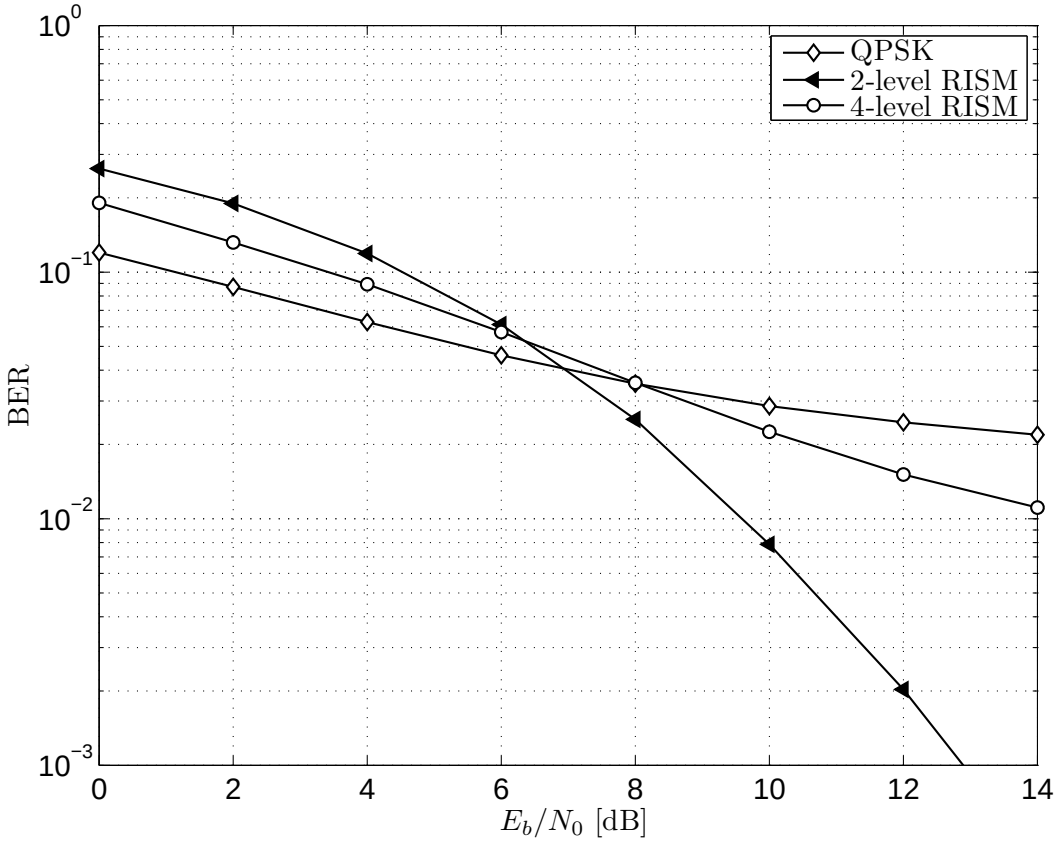

Figure 2.17: BER Performance using Saleh model with IBO $= 0\ dB$.

relation between OBO and TD is not a function. Obviously this happens because the same OBO value may corresponding to two different IBO conditions, which, nevertheless, lead to different TD values.

Comparing the plots in figures, 2.25,2.26, and 2.27, we can see how considered HPA models differently act to the degradation of the signal. As shown in figures 2.25 and 2.26, considering mildly distorting HPA model, such as IC or Rapp model, and a robust MOD-COD configuration yielding a low SNR_{req} value, the contribution given by the term δ_{SNR} is never dominating even for very low OBO values. Then in these cases, it is possible to transmit using low back-off and the advantages given by PAPR reduction techniques are, here, not remarkable.

On the other hand, as shown in Figures 2.22 and 2.27, considering Saleh HPA model, the term δ_{SNR} is dominating in the low OBO regions. In particular, in very low back-off conditions δ_{SNR} tends to infinity. It means that the considered nonlinear system can not reach the target performance, BER_{req}, regardless of the strength

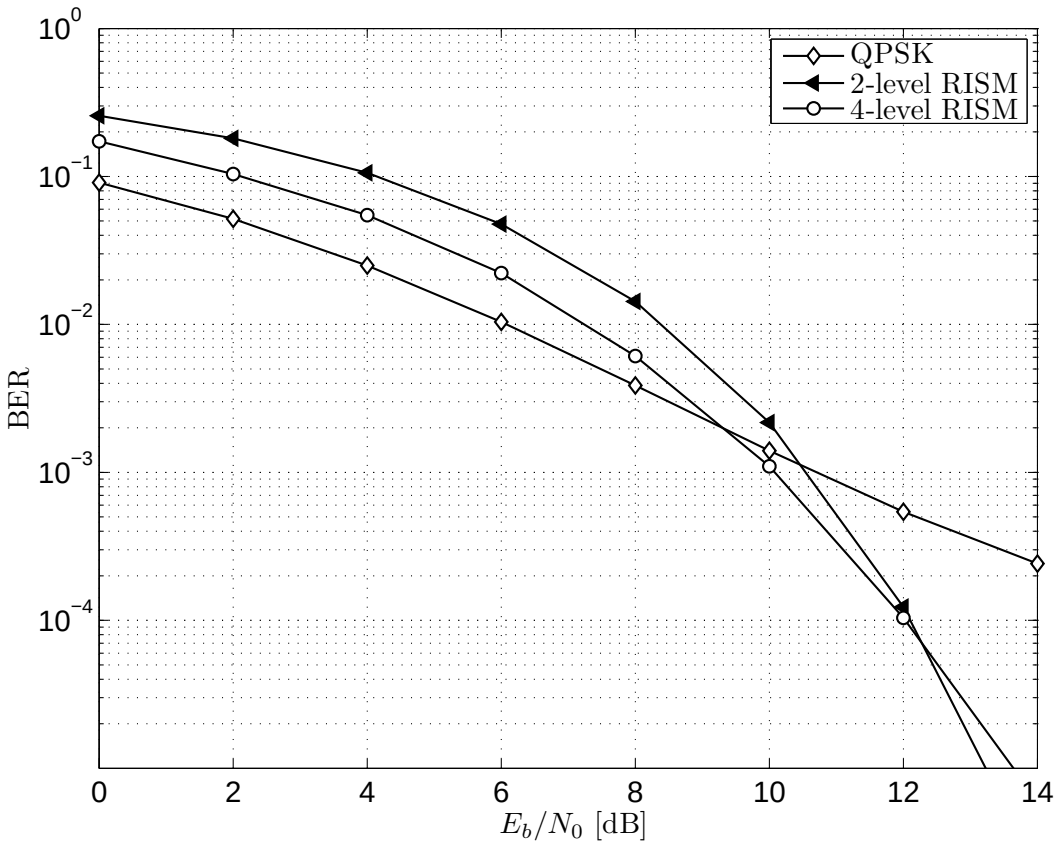

Figure 2.18: BER Performance in case of Ideal Clipping IBO $= 0\ dB$.

of the received signal. In these scenarios the improvements due to PAPR reduction technique become conspicuous. In the same way, as shown in Figures 2.31 and 2.32, considering less robust MOD-COD configurations yielding higher SNR_{req} values, the term δ_{SNR} becomes dominating even in cases of IC and Rapp HPA models. Also in these conditions the advantages bring by a lower PAPR are evident.

2.4.3.1 A further thought about TD in OFDM systems

Although TD, as shown above, is a valuable figure of merit to evaluate the system performance over nonlinear channels, its computation is usually a tedious and time-consuming task for the following reason:

- to compute a single value of $\delta_{\mathrm{SNR}}(\mathrm{IBO})$ a complete end-to-end coded and nonlinear simulation must to be carried out.

- the value of δ_{SNR} is graphically obtained (measuring the distance between the

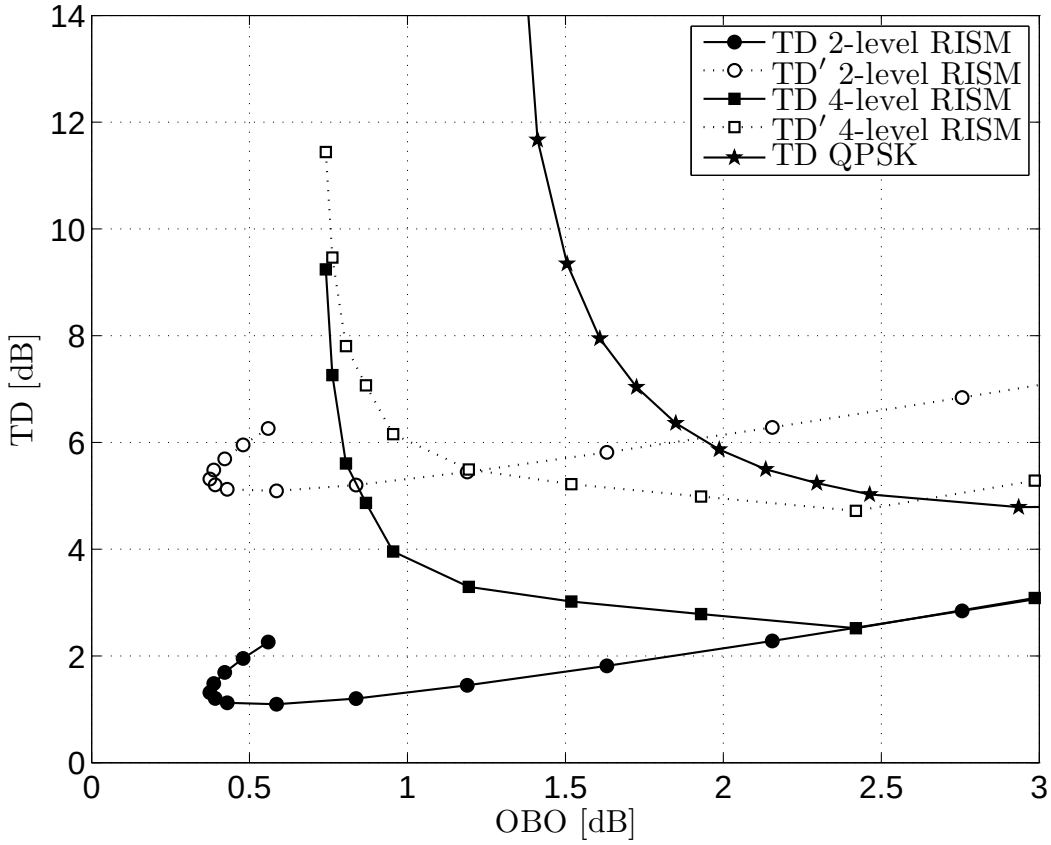

Figure 2.19: Total degradation performance using Saleh model.

linear and non-linear curves).

On the other hand, considering a multicarrier signal we can apply the Bussgang's Theorem in order to facilitate and speed up the computation of TD. If we consider N large enough the distortion term due to the non-linearities can be modelled as a Gaussian disturbance. Then we can express the SNR_{req} as:

$$\mathrm{SNR}_{req} = \frac{1}{\left(\frac{1}{\mathrm{SNR}_{req}}\frac{1}{\delta_{\mathrm{SNR}}}\right) + \left(\frac{1}{\mathrm{SDR}}\right)} \tag{2.41}$$

therefore:

$$\delta_{\mathrm{SNR}} = \left(1 - \frac{\mathrm{SNR}_{req}}{\mathrm{SDR}}\right)^{-1} \tag{2.42}$$

Where δ_{SNR} is defined only for $\mathrm{SNR}_{req} > \mathrm{SDR}$. Otherwise the system will never reach the target performance BER_{req}. Now we can easily compute the TD starting from the computation of SDR as a function of IBO, reported in Figures 2.20, 2.21, and 2.22, with the following advantages:

- No end-to-end coded simulations are needed.
- The computation of $\mathrm{SDR}(\mathrm{IBO})$ is extremely faster.
- A smaller step IBO can be used. Smoother plots are obtained using a minor computation effort.

Furthermore, considering IC HPA model it is also possible to express analytically the Total Degradation as a function of IBO. Substituting Eq. (2.22) in Eq. (2.42) we obtain:

$$\delta_{\mathrm{SNR}} = \left(1 - \mathrm{SNR}_{req}\left(\frac{1-\mathrm{e}^{-\mathrm{IBO}}}{\left(1-\mathrm{e}^{-\mathrm{IBO}}+\frac{\sqrt{\pi\mathrm{IBO}}}{2}\,\mathrm{erfc}\left(\sqrt{\mathrm{IBO}}\right)\right)^2}-1\right)\right)^{-1} \tag{2.43}$$

Finally, substituting Eq. (2.24), and Eq. (2.43) in Eq. (2.39) we obtain:

$$\mathrm{TD} = \frac{\mathrm{IBO}}{1-\mathrm{e}^{-\mathrm{IBO}}}\left(1 - \mathrm{SNR}_{req}\left(\frac{1-\mathrm{e}^{-\mathrm{IBO}}}{\left(1-\mathrm{e}^{-\mathrm{IBO}}+\frac{\sqrt{\pi\mathrm{IBO}}}{2}\,\mathrm{erfc}\left(\sqrt{\mathrm{IBO}}\right)\right)^2}-1\right)\right)^{-1} \tag{2.44}$$

This analytical results have been validate through numerical simulations results.

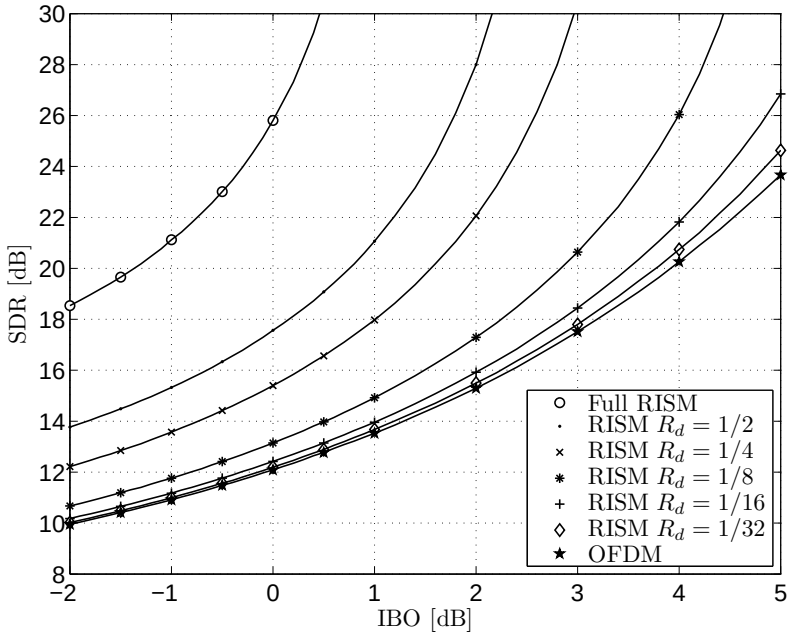

Figure 2.20: Signal-to-Distortion Ratio using Hybrid RISM for different values of the RISM tone density, with Ideal Clipping HPA model.

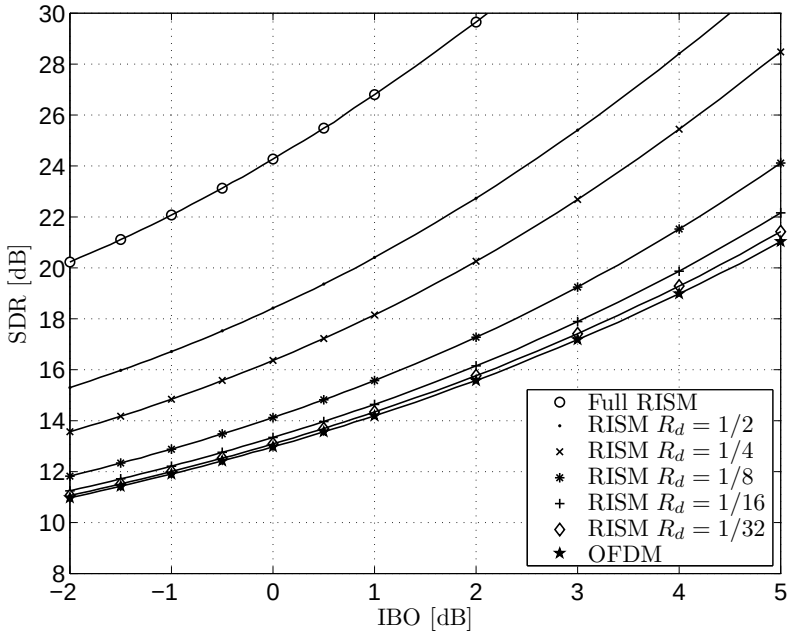

Figure 2.21: Signal-to-Distortion Ratio using Hybrid RISM for different values of the RISM tone density, with Rapp HPA model.

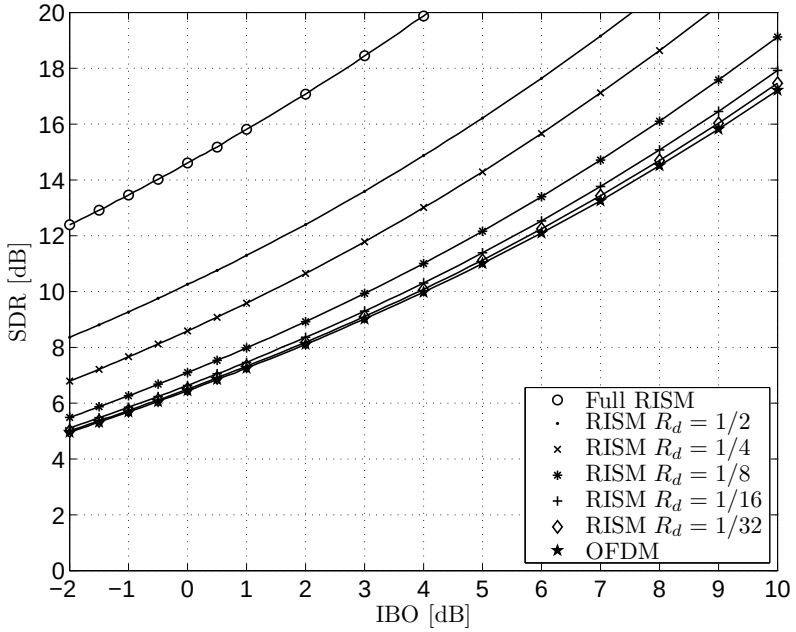

Figure 2.22: Signal-to-Distortion Ratio using Hybrid RISM for different values of the RISM tone density, with Saleh HPA model.

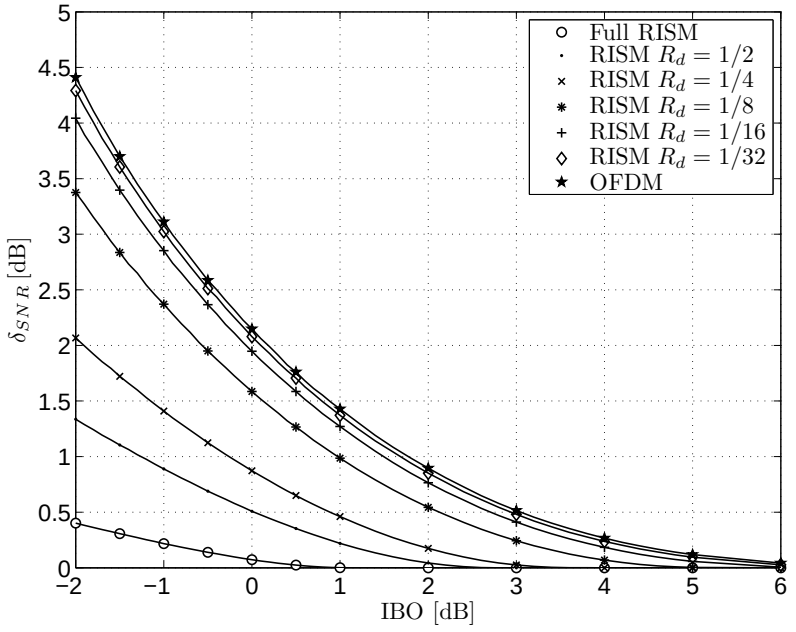

Figure 2.23: δ_{SNR}, The power boosting needed to compensate the effect of the nonlinear distortion with IC HPA model, $SNR_{req} = 8$ dB.

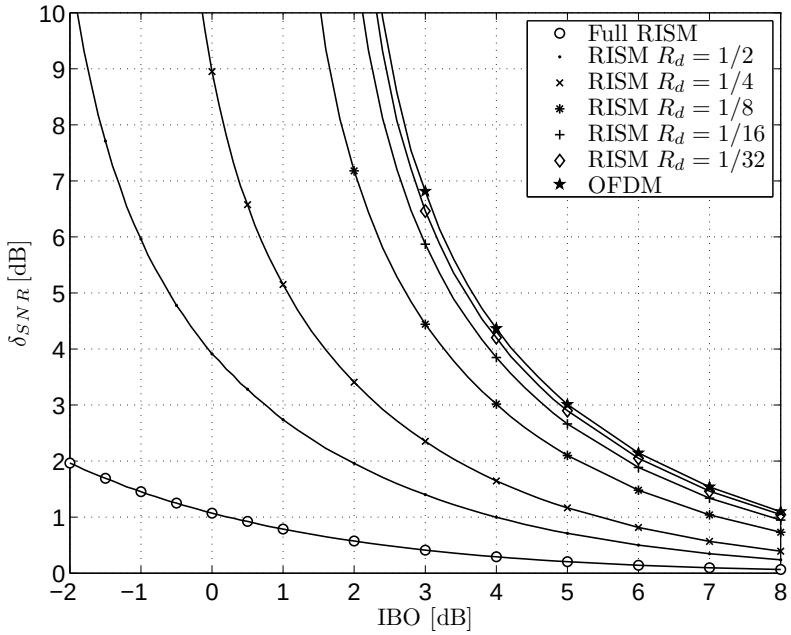

Figure 2.24: δ_{SNR}, The power boosting needed to compensate the effect of the nonlinear distortion with Saleh HPA model, $SNR_{req} = 8$ dB.

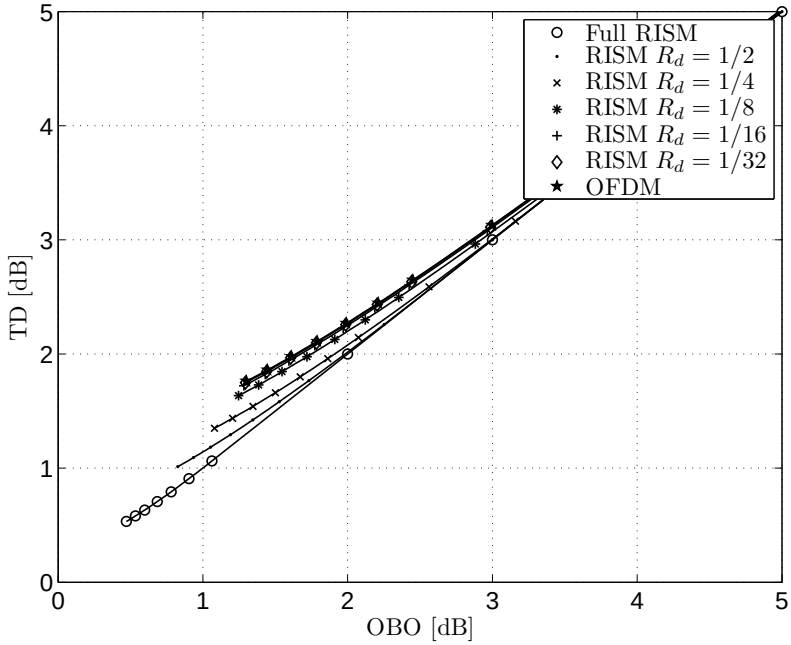

Figure 2.25: Hybrid RISM Total Degradation performance using Ideal Clipping model, $SNR_{req} = 0$ dB.

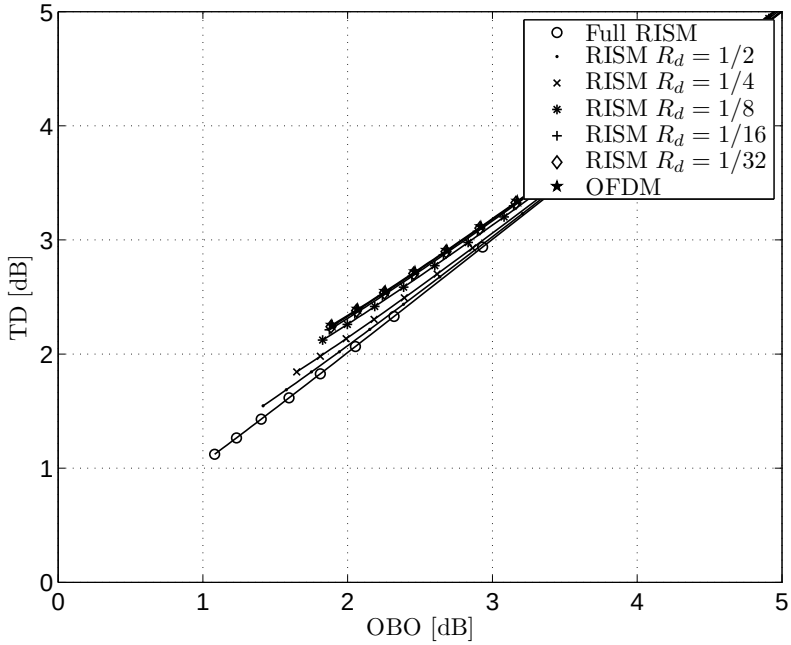

Figure 2.26: Hybrid RISM Total Degradation performance using Rapp model, $SNR_{req} = 0$ dB.

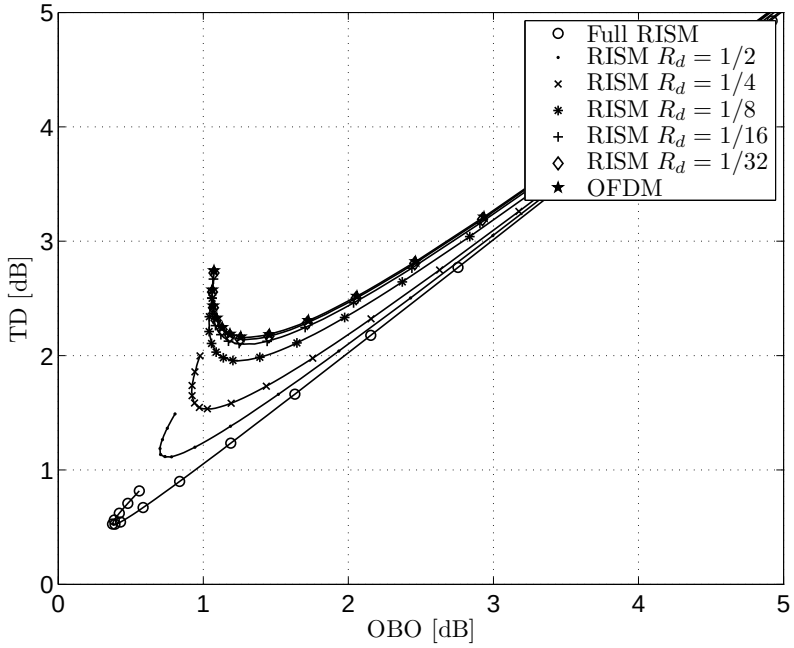

Figure 2.27: Hybrid RISM Total Degradation performance using Saleh model, $SNR_{req} = 0$ dB.

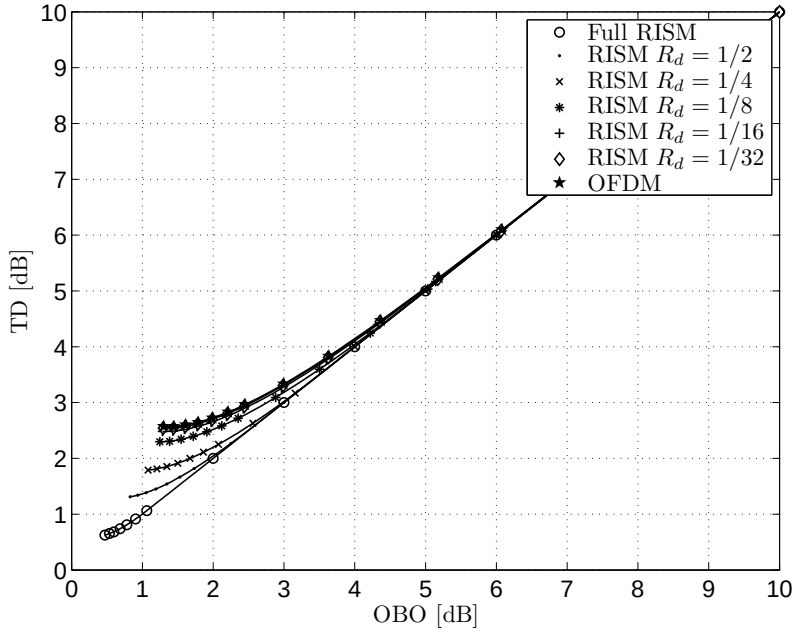

Figure 2.28: Hybrid RISM Total Degradation performance using Ideal Clipping model, $SNR_{req} = 4$ dB.

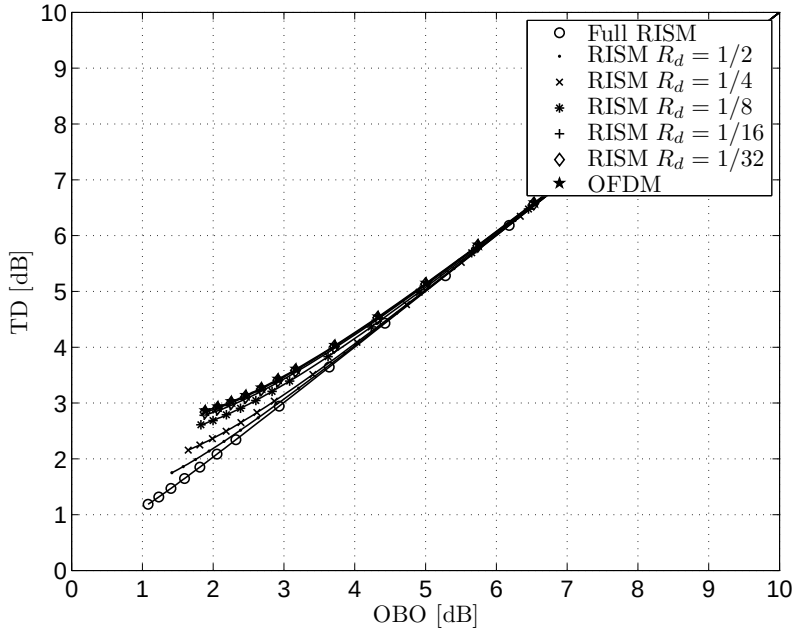

Figure 2.29: Hybrid RISM Total Degradation performance using Rapp model, $SNR_{req} = 4$ dB.

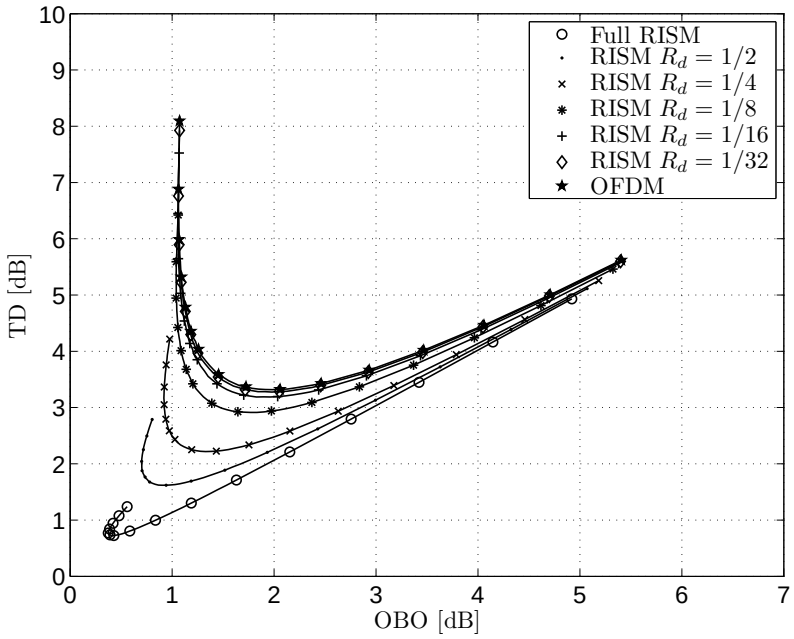

Figure 2.30: Hybrid RISM Total Degradation performance using Saleh model, $SNR_{req} = 4$ dB.

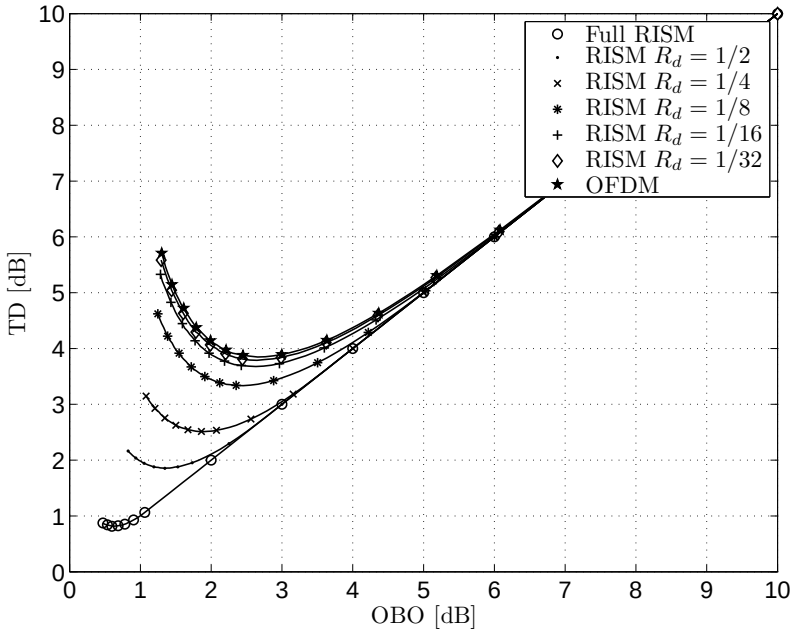

Figure 2.31: Hybrid RISM Total Degradation performance using Ideal Clipping model, $SNR_{req} = 8$ dB.

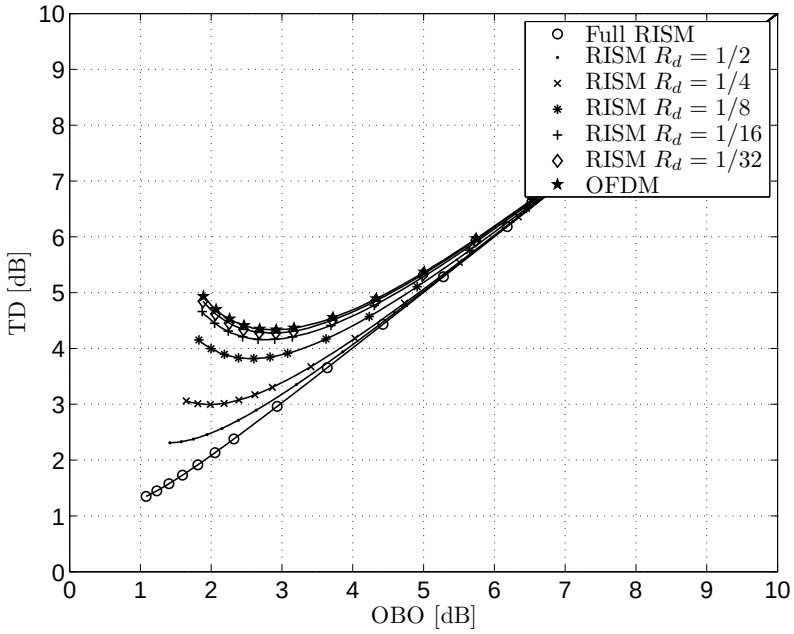

Figure 2.32: Hybrid RISM Total Degradation performance using Rapp model, $SNR_{req} = 8$ dB.

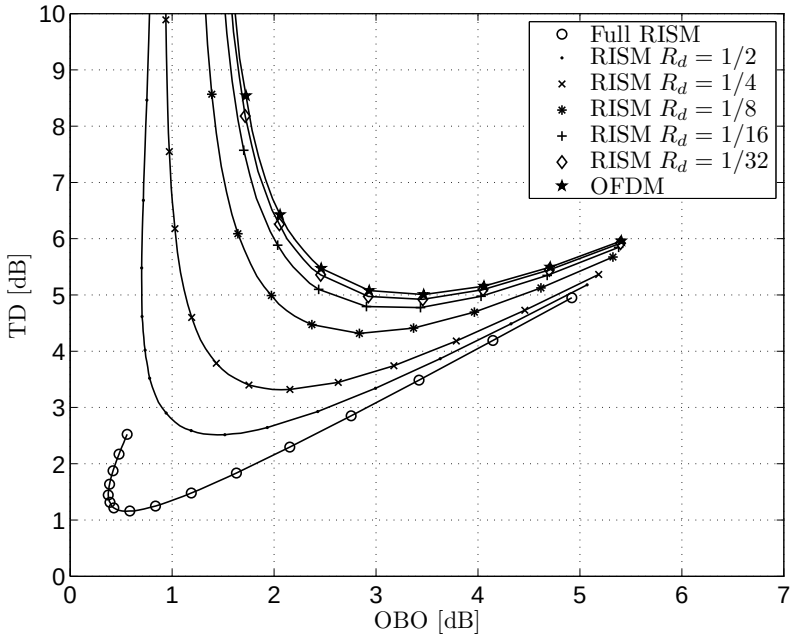

Figure 2.33: Hybrid RISM Total Degradation performance using Saleh model, $SNR_{req} = 8$ dB.

This page intentionally contains only this sentence.

CHAPTER 3

TIME AND FREQUENCY SYNCHRONIZATION

When Charles V retired in weariness from the greatest throne in the world to the solitude of this monastery at Yuste, he occupied his leisure for some weeks in trying to regulate two clocks. It proved very difficult. One day, it is recorded, he turned to his assistant and said: To think that I attempted to force the reason and conscience of thousands of men into one mold, and I cannot make two clocks agree![1]

The Task of Social Hygiene, Havelock Ellis

IN SECTION 1.5, we have considered the ideal case where the transmission between transmitter and receiver is perfectly aligned in time and frequency. However, in real-world systems perfect synchronization is impossible to achieve, and the following aspects must to be addressed in order to design the receiver:

- The receiver is not aware of the **timing** at the transmitter. Therefore, the receiver must estimate the position of the OFDM symbols in order to remove the CP and correctly position the FFT window. We indicate the timing offset with Δ_t.

[1] This citation is reported in a famous paper by Scholtz [44]

- The **frequency** oscillators used for modulating and demodulating the signal are never perfectly aligned. Thus, the receiver must estimate the carrier frequency offset Δ_f, and adjust it accordingly.
- To shift down the received signal from RF to baseband non-ideal frequency oscillators are used. They will introduce **phase noise** on the received signal.

3.1 Effects of time and frequency offsets and phase noise

In order to provide a realistic model, the effects of the aforementioned disturbances shall be taken into account in the system model. Firstly the timing offset Δ_t can be incorporated into the channel model in (1.14):

$$h(t,\tau) = \sum_j h_j(t) \cdot \delta\left(\tau - \tau_j - \Delta_t\right) \tag{3.1}$$

At the same time, the carrier frequency offset Δ_f can be interpreted as a time-variant phase offset of the received signal:

$$r(t) = \mathrm{e}^{2\pi\Delta_f t}\left(h(t,\tau) * s(t)\right) + n(t) \tag{3.2}$$

In addition, the phase noise process, $\phi(t)$, is typically characterized by a single-side-band phase noise power density function, which is also known as Phase Noise Mask (PNM). PNM represents the ratio in dBc (dB carrier) between the single-side-band noise power in a 1 Hz bandwidth at a given distance from the carrier, and the carrier power [45]. In figure 3.1, we report a practical example of PNM which has been specified during the DVB-RCS standardization [22]. At the receiver, the phase noise process, $\phi(t)$, can be modelled as a undesired phase modulation:

$$r(t) = \mathrm{e}^{\jmath\phi(t)}\left(h(t) * s(t)\right) + n(t) \tag{3.3}$$

Summarizing, in order to incorporate the mentioned effects, we modify Eq.(1.16) as follows:

$$r(iT) = \mathrm{e}^{\jmath\phi(t)}\mathrm{e}^{\jmath 2\pi\Delta_f T_u}\sum_j h_j(uT)s(uT - \tau_j - \Delta_t) + n(uT) \tag{3.4}$$

In order to highlight these effects in the OFDM signal we express:

- The timing offset normalized to the sampling time as the sum of two contributions: an integer multiple of T, and a fractional part:

$$\frac{\Delta_t}{T} = m + \upsilon \tag{3.5}$$

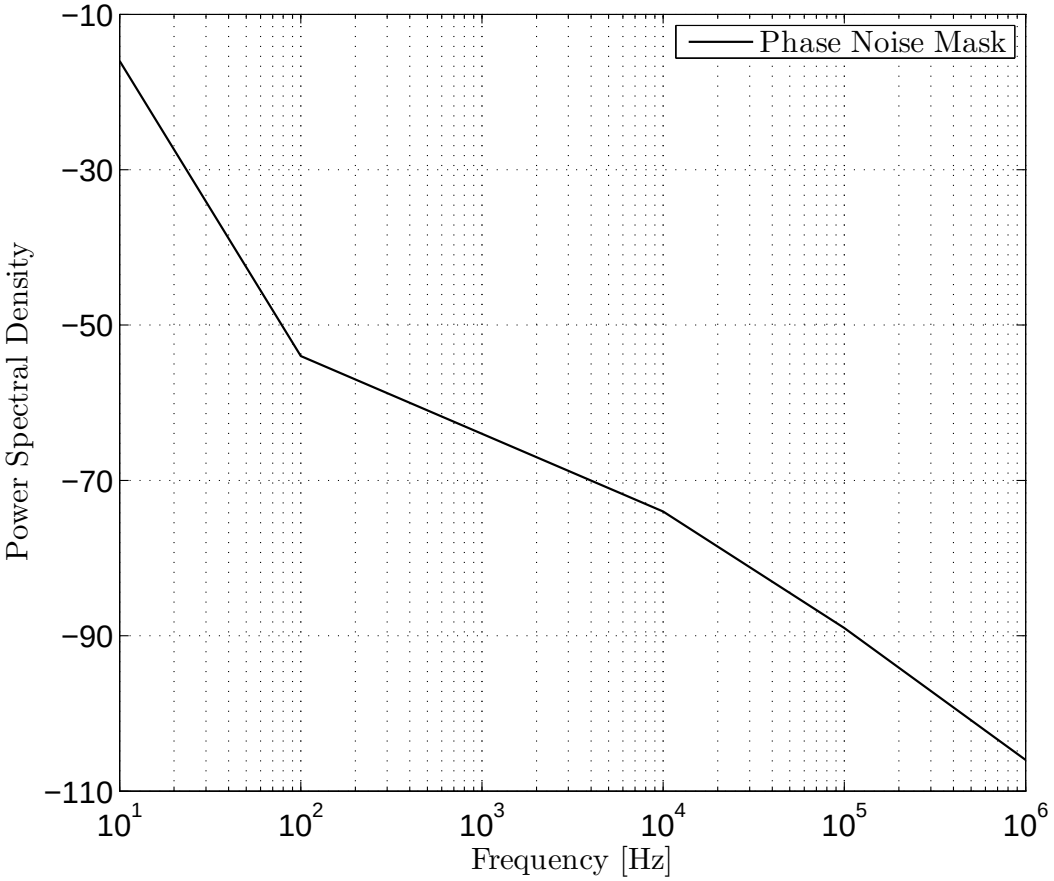

Figure 3.1: DVB-RCS Phase Noise Mask

where $m \in \mathbb{Z}$ and $\upsilon \in [-0.5; 0.5[$. Without loss of generality, we can assume $\upsilon = 0$ [11].

- The frequency offset normalized to the subcarrier spacing as the sum of two contributions: an integer part, and a fractional part:

$$\frac{\Delta f}{f_u} = n + \varepsilon \tag{3.6}$$

where $m \in \mathbb{Z}$ and $\varepsilon \in [-0.5; 0.5[$.

- The phase noise process as the sum of two terms: the mean-value of $\phi(t)$ computed within a OFDM symbol duration, ϕ_ℓ^{cpe} , and the remaining fluctuating component $\phi^{ici}(t)$ that is time-variant inside the OFDM symbol.

$$\phi(t) = \phi_\ell^{cpe} + \phi^{ici}(t) \tag{3.7}$$

Note that ϕ_ℓ^{cpe}, depends on only on the OFDM symbol index.

Substituting, (3.5), (3.6), and (3.7) in (3.4) we obtain:

$$r(iT) = \mathrm{e}^{\phi_\ell^{cpe}}\ \mathrm{e}^{\phi^{ici}(iT)}\ \mathrm{e}^{\jmath 2\pi n}\ \mathrm{e}^{\jmath 2\pi\varepsilon} \sum_j h_j(uT)s(uT - mT - \upsilon T - \tau_j) + n(uT) \quad (3.8)$$

Let us consider a OFDM signal afflicted by a timing offset mT, it will maintain the orthogonality between the subcarriers if and only if the time domain samples at the receiver, $\bar{r}_\ell$, are composed only by samples belonging to the same OFDM transmitted symbol [11]. In other words, to avoid ICI, the receiver must integrate over an integer number of sinusoid cycles for each of the received multipaths when it performs OFDM demodulation with the FFT. Therefore, both ICI and ISI caused by timing offeset are avoided if and only if the following condition is satisfied:

$$\lfloor \frac{\tau_{max}}{T} - N_g \rfloor \leq m \leq 0 \quad (3.9)$$

However, even if the condition in Eq.(3.9) is satisfied, as a consequence of the timing offset, the received signal in the frequency domain will be afflicted by a phase rotation, $\mathrm{e}^{2\pi mk/N}$, that will be compensated afterwards, during the channel estimation.

Regarding the frequency offset, two different effects on the OFDM signal can be distinguished. The fractional part of the normalized frequency offset, ε, introduces a phase rotation (phase ramp) in the time domain which breaks the subcarrier orthogonality introducing ICI. On the other hand, the integer part of the normalized frequency offset, n, is responsible of a spectral shift in the received symbols in the frequency domain (after the FFT operation), while preserving the subcarrier orthogonality.

Similarly to the frequency offset, also the phase noise is responsible of two different effects [46] [47]. Firstly, the constant component, ϕ_ℓ^{cpe} introduces a Common Phase Error (CPE), which consists in a constant phase rotation equal to ϕ_ℓ^{cpe} over all the subcarriers. Secondly, the fluctuating component causes ICI, which can be treated as a growth of the Additive Gaussian Noise.

Under the assumption that the subcarrier orthogonality is preserved[2] the expression of the received signal in the frequency domain in Eq.(1.18) becomes:

$$y_{k,\ell} = \mathrm{e}^{\jmath\left(\frac{2\pi mk}{N} + \phi_\ell^{cpe}\right)} x_{k-n,\ell}\, H_{k-n,\ell} + n_{k,\ell} \qquad k = 0, \ldots, N-1 \quad (3.10)$$

[2] Eq.(3.9) is satisfied, $\phi^{ici}(t) = 0$, and $\varepsilon = 0$

3.2 OFDM Synchronization strategy

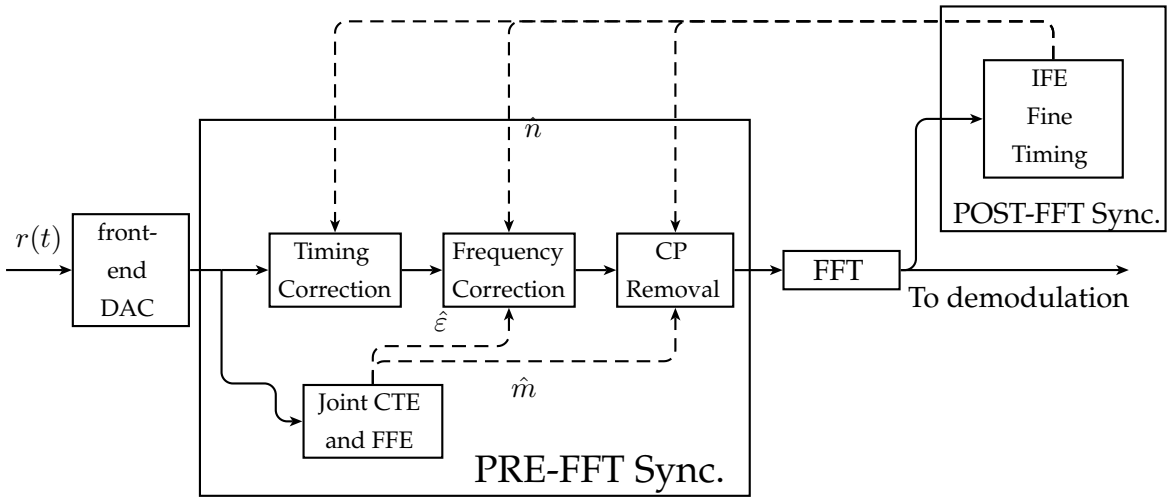

Figure 3.2: Generic synchronization steps for OFDM systems.

In general, symbol timing and carrier frequency offsets are recovered in two separate phases called PRE-FFT and POST-FFT synchronization, as shown in Fig. 3.2. In the PRE-FFT phase, the estimation algorithms operate in the time domain, while in POST-FFT, the algorithms operate in the frequency domain. As illustrate in Fig. 3.2, The PRE-FFT synchronization algorithms must accomplish two tasks: Coarse Timing Estimation (CTE) and Fractional Frequency Estimation (FFE). The aim of CTE is to detect the beginning of the OFDM symbol, in order to remove the CP and correctly position the OFDM symbol within the FFT window, in order to satisfy the condition in Eq.(3.9), and then avoid ICI and ISI. On the other hand, the goal of FFE is to estimate the fractional part of the carrier frequency offset, in order to maintain the mutual orthogonality among the subcarriers. The PRE-FFT synchronization can be either Data-Aided (DA) or Not-Data-Aided (NDA). The PRE-FFT NDA synchronization methods exploit the redundancy introduced by the CP to performed the estimation. On the other hand, in the PRE-FFT DA approach, synchronization methods make use of a known preamble inserted into the frame to facilitate the synchronization. Although some DA methods try to estimate the also integer part of carrier frequency offset in the PRE-FFT stage, the resulting achievable acquisition range is too limited to be applied to realistic scenarios. Therefore,

the estimation of carrier frequency offset must to be finalized during the POST-FFT synchronization phase.

The following POST-FFT synchronization acts to refine the PRE-FFT estimates. Firstly the integer part of the normalized frequency offset is estimated to complete frequency offset recovery. As detailed in following, the POST-FFT Integer Frequency Estimation (IFE) typically to exploits part of the pilot tones which are included in the OFDM comb in order to recover the correct frequency alignment. As as second task, the symbol timing estimation is refined by exploiting the pilot tones to improve the CTE performed in the PRE-FFT stage. Afterwards, some others minor task can be performed at the POST-FFT stage depending on the scenario, on the requirements, and, on the provided pilot tones. For example, in case of DVB-T/H/SH, it is needed to detect the position of the scattered pilot tones [48].

3.3 PRE-FFT Synchronization

Many possible approaches which have been presented in the scientific literature make use of the redundancy introduced by the CP in order to accomplish the PRE-FFT synchronization. Among the most relevant ones we consider: the Maximum Likelihood (ML) algorithm proposed in [49]; the approaches proposed in [50] and in [51] based on simplification of the ML algorithm; the double correlator algorithm proposed in [52], which has been designed to work in presence of multipath propagation; the Exponential Weighted Average (EWA) algorithms proposed in [53] and [54] that present a very low implementation complexity. EWA algorithms is based on the substitution of the moving sum, used in the previous algorithms, with an Exponential Weighted Sum (EWS). Furthermore, we present an original technique named Enhanced EWS (EEWS) which has been presented in by the authors in [55]. This algorithm drastically decreases the implementation complexity having a estimation accuracy comparable to with the high complexity algorithms.

3.3.1 Existing algorithms for CTE and FFE

The CP based PRE-FFT algorithms exploit the correlation between the final part of the useful symbol and the CP. The simplest method is the Maximum Correlation (MC) algorithm [50], that computes the correlation between the received samples and the complex conjugate of received samples delayed by N samples. we can

write the following metric as,

$$F_{MC}(m) = \left| \sum_{i=m}^{m+N_g-1} r^* \left((i-N)T\right)\ r(iT) \right| \tag{3.11}$$

The observation of $2N + N_g$ received samples in the time domain, ensures that one complete OFDM symbol and its guard interval are actually observed. The term $F_{MC}(m)$ reaches its maximum value when all the sampled $r(iT)$ correspond to the last N_g samples of the current OFDM symbol, and consequently $r((i-N)T)$ falls into the guard interval. The value of m for which this occurs will give the correct position for centering the FFT window in the receiver. Hence, it is possible to estimate the correct position of the FFT window by maximizing the function $F_{MC}(m)$. In addition, we can estimate ε by extracting the phase offset between the last N_g samples of a OFDM symbol and the CP samples:

$$\hat{\epsilon} = \frac{1}{2\pi} \arctan \left\{ \sum_{i=\hat{m}}^{\hat{m}+N_g-1} r^* \left((i-N)T\right)\ r(iT) \right\} \tag{3.12}$$

where:

$$\hat{m} = arg \left(\max_m \{F(m)\} \right) \tag{3.13}$$

In the following, we name as *metric* of an algorithm the function to be maximized. Hence, we can summarize the known algorithms by reporting their metrics, i.e.,

$$F_{ML}(m) = F_{MC}(m) - \frac{\gamma}{2(\gamma+1)} \sum_{i=m}^{m+N_g-1} \left|r\left((i-N)T\right)\right|^2 + \left|r\left(iT\right)\right|^2 \tag{3.14}$$

$$F_{MMSE}(m) = F_{MC}(m) - \frac{1}{2} \sum_{i=m}^{m+N_g-1} \left|r\left((i-N)T\right)\right|^2 + \left|r\left(iT\right)\right|^2 \tag{3.15}$$

$$F_{DC}(m) = \left| \sum_{i=m}^{m+N_g-1} F^*\left(m+i-N-N_g\right) F\left(m+i\right) \right| \tag{3.16}$$

where:

$$F(m) = \sum_{i=m}^{m+N_g-1} r^*\left((i-N)T\right) r\left(iT\right) \tag{3.17}$$

Eq. (3.14) shows the *metric* of ML estimator [49]. It can be noted that the MC algorithm can be derived from the ML algorithm by neglecting the energy part.

On the other hand, the ML estimator requires the a priori knowledge of the signal-to-noise ratio (SNR), γ. In the algorithm proposed in [51], the *metric* reported in Eq. (3.15) is equal to the *metric* of ML neglecting the γ factor. This algorithm is also known as Minimum Mean Square Error (MMSE) estimator. It is worthwhile observing that for high SNR, (3.15) and (3.14) converge to the same *metric*. On the other hand, when the SNR decreases, the terms $|r\,(iT)|^2$ are corrupted by noise, therefore in the ML approach the energy part is weighted by γ. Hence, for low SNR value (3.11) and (3.14) are similar. Eq. (3.16) shows the *metric* proposed in [52]. This solution is designed to achieve the PRE-FFT tasks in case of multipath channel using two correlators in cascade. In the following, we name this algorithm as Double Correlator (DC) estimator.

3.3.2 Low-complexity PRE-FFT algorithms

Let us define z_i as the product between the received samples and the complex conjugate of received sampled delayed by N samples, that is $z_i = r^*\,((i-N)T)\,r\,(iT)$. Observing Eq. (3.11), we notice that the MC method implements a Moving Sum (MS) having length N_g over the sequence z_i. Similarly to MC, the methods proposed in [49], [51], [52] use a MS in order to obtain their metrics. The main idea of low-complexity techniques is to substitute the MS block with an Exponential Weighted Sum (EWS) in order to reduce the computational complexity. The use of EWS is proposed in [53] and [54] [3], where the *metric* is:

$$F_{EWS}(m) = \left| \sum_{i=0}^{m} z_i\ \lambda^{m-i} \right| \tag{3.18}$$

where $\lambda = 1 - 2^{-M}$ is the weighing factor and M is a positive number. The choice of the appropriate weighting factor, and thus, the choice of M, is fundamental for the right functioning of this estimator. In Section 3.3.4 we mathematically deduce the value of M that minimizes the standard deviation of error estimation.

3.3.3 EEWS algorithm

Now we present an original contribution to PRE-FFT synchronization named Enhanced EWS [55] (EEWS) algorithm that drastically increases the estimation accuracy with respect to the EWA without significantly increasing the implementation complexity. The proposed algorithm is based on the introduction of an ad-

[3] In [53] and in [54] the authors called this approach Exponential Weighted Average (EWA)

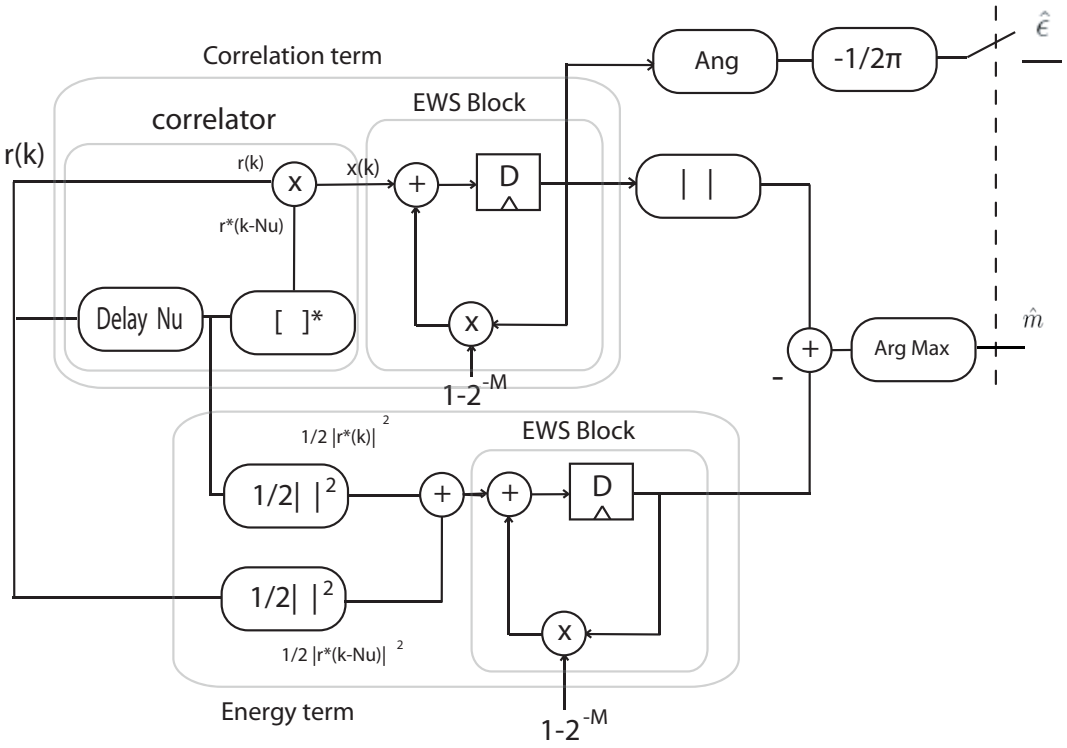

Figure 3.3: Block diagram of the proposed EEWS algorithm.

ditional energy correcting factor in the EWA scheme. Differently from [53] and [54], the EEWS algorithm takes into account also the energy term. The key idea is to starts from the *metric* in Eq. (3.15), and then substitute the two MSs with two EWSs, with the aim to exploit the benefits from both approaches. Hence, the resulting *metric* is:

$$F_{EEWS}(m) = \left| \sum_{i=0}^{m} z_i \lambda^{m-i} \right| - \frac{1}{2} \sum_{i=0}^{m} \left(|r_i|^2 + |r(i-N_g)|^2 \right) \lambda^{m-i} \tag{3.19}$$

The estimation of m is still computed according to Eq. (3.13), i.e., maximizing the F_{EEWS} function, while ϵ can be estimated as:

$$\hat{\epsilon} = \frac{1}{2\pi} \arctan \left\{ \sum_{i=0}^{\hat{m}} z_i \ \lambda^{\hat{m}-i} \right\} \tag{3.20}$$

In figure 3.3 the block scheme of the EEWS algorithm is illustrated.

3.3.4 EEWS Optimization

In the MS scheme, all N_g past samples are summed with weigh equal to one, while in the EWS scheme all past samples are summed with a weight that decrease

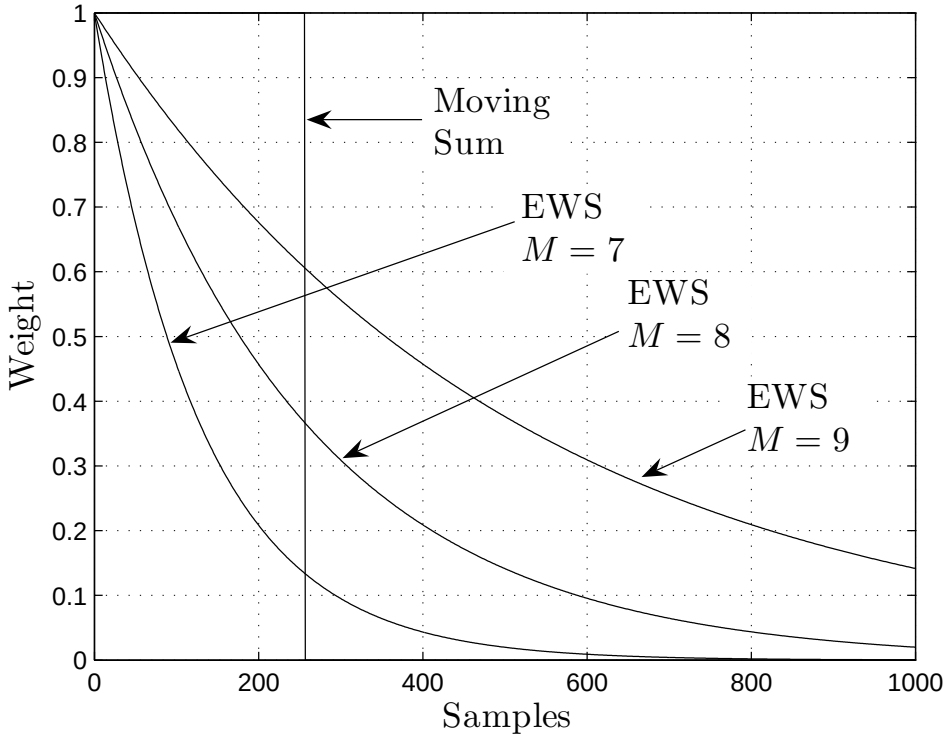

Figure 3.4: Several shapes of EWS weighting windows for different values of M.

exponentially as λ^{m-i}. The choice of the appropriate weighting factor depends on N_g, because if λ is too small, the weights decrease too rapidly and it does not take in account all samples belonging to the guard interval. On the other hand, if λ is too close to 1, the weights decrease too slowly and extend way beyond the guard interval. In figure 3.4 several shapes of EWS windows are depicted for different values of M.

Let us define the function $\Upsilon(M, j)$ as the sum of all weights of samples z_i belonging to the guard interval, when the weighting factor is $\lambda = 1 - 2^{-M}$. The index j indicates the misalignment between the begin of the EWS window and the first sample belonging to the guard interval.

$$\Upsilon(M, j) \doteq \sum_{t=\max(0,j)}^{N_g+j-1} \left(1 - 2^{-M}\right)^t \tag{3.21}$$

Let us consider the case $j = 0$, in which the start of EWS window coincides with

the last sample of guard interval. This yields to:

$$\Upsilon(M,0) = \sum_{t=0}^{N_g-1}(1-2^{-M})^t = \frac{1-(1-2^{-M})^{N_g}}{2^{-M}} \tag{3.22}$$

Now we consider the cases $j=-1$ and $j=1$:

$$\Upsilon(M,-1) = \sum_{t=0}^{N_g-2}(1-2^{-M})^t = \frac{1-(1-2^{-M})^{N_g-1}}{2^{-M}} \tag{3.23}$$

$$\Upsilon(M,1) = \sum_{t=1}^{N_g}(1-2^{-M})^t = \frac{(1-2^{-M})-(1-2^{-M})^{N_g+1}}{2^{-M}} \tag{3.24}$$

Our goal is to obtain M such that the minimum distance between $\Upsilon(M,0)$ and $\Upsilon(M,j)$ with $j \neq 0$ is maximized. Obviously $\Upsilon(M,0) > \Upsilon(M,j)$ with $j \neq 0$:

$$M_{op} = arg\left(\max_M\left(\min_{j\neq 0}(\Upsilon(M,0)-\Upsilon(M,i))\right)\right) \tag{3.25}$$

The minimum distance is achieved in case of minimum misalignment between the begin of EWS window and the first sample belonging to the guard interval, hence when $j=1$ or $j=-1$.

$$M_{op} = arg\left(\max_M\left(\min_{j\in\{-1,1\}}(\Upsilon(M,0)-\Upsilon(M,j))\right)\right) \tag{3.26}$$

In figure 3.5 is shown the plot of $\Upsilon(M,0)-\Upsilon(M,-1)$ and $\Upsilon(M,0)-\Upsilon(M,1)$ as a function of M and N_g. The minimum distance is maximized when $\Upsilon(M,1) = \Upsilon(M,-1)$. Moreover, in this case we achieve the symmetry of the PDF of probability of error.

$$M_{op} = \{M : \Upsilon(M,-1) = \Upsilon(M,1)\} \tag{3.27}$$

The search of M_{op} is the root of the following equation obtained by the substitution of (3.21) in (3.27):

$$\left(1-2^{-M}\right)^{N_g+1} - \left(1-2^{-M}\right)^{N_g-1} + 2^{-M} = 0 \tag{3.28}$$

In table 3.1, several values of M_{op} are shown for values of N_g compliant with the DVB-SH standard.

3.3.5 Complexity and Performance Comparison

For practical applications, the hardware complexity of an algorithm is of great importance. In this Section, we evaluate the complexity of the EEWS algorithm and we compare it with respect to the other discussed algorithms.

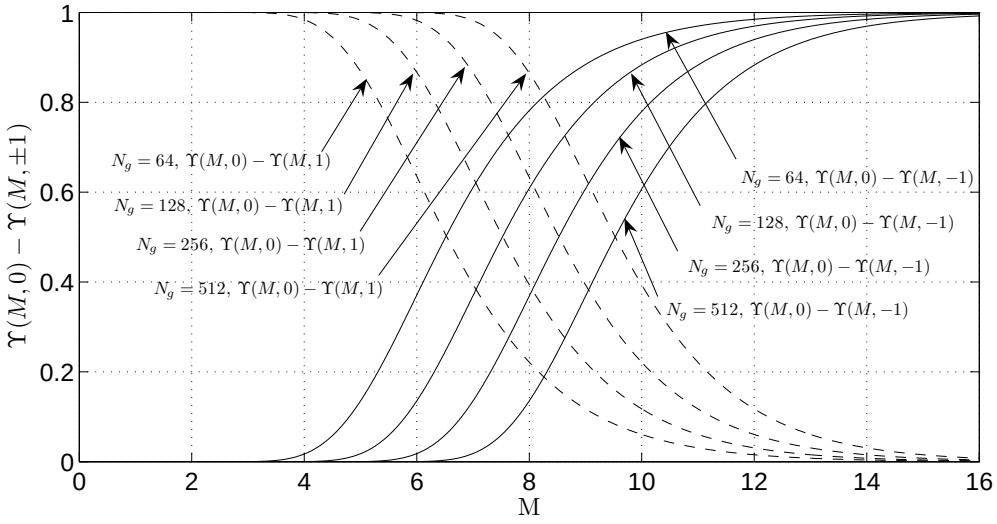

Figure 3.5: The plot of $\Upsilon(M,0) - \Upsilon(M,-1)$ and $\Upsilon(M,0) - \Upsilon(M,1)$ as a function of M, with several N_g values.

Table 3.1: Several values of M_{op} for DVB-SH value of N_g

N_g	M_{op}
64	6.527
128	7.527
256	8.5278
512	9.528
1024	10.528

As shown in figure 3.3, the EWS block can be implemented by an adder and a shift register. On the other hand, the MC algorithm, which is based on MS block, requires N_g shift registers and N_g adders. In addition, the algorithms that take into account the energy term in addition to the correlation term require two additional adders for the sum between the two terms. Hence, the MMSE algorithm, which is based on a MS scheme and takes in account the energy term, requires $2N_g$ shift registers and $2N_g + 2$ adders. On the other hand, the novel EEWS algorithm, which is based on EWS scheme requires only 2 shift registers and 4 adders, for whichever value of N_g.

In table 3.2, the number of required shift register and adder in case of $N_g = 256$ is summarized. It can be easily observed that the EWS based techniques reduce the computational complexity by more than 99% compared to the algorithms using the

Table 3.2: Required shift register and adder in case of $N_g = 256$

Algorithm	Shift registers	Adders	shift registers $N_g = 256$	Adders $N_g = 256$
MC	N_g	N_g	256	256
MMSE	$2N_g$	$2N_g + 2$	512	514
EWS	1	1	1	1
EEWS	2	4	2	4

Table 3.3: Power delay profile of multipath channel

Path	Sat	#1	#2	#3	#4
K[dB]	7	-100	-100	-100	-100
Delay[μs]	0.0	8.203	9.179	10.87	11.01
Power[dB]	-91.7	74.4	-86.3	-85.4	-86.8
Path	#5	#6	#7	#8	#9
K[dB]	-100	-100	-100	-100	-100
Delay[μs]	12.63	18.09	18.24	18.48	22.91
Power[dB]	-86.4	-89.2	73.6	-88.6	-89.3

MS block.

We use Monte Carlo simulations to evaluate the performance of each estimator. We consider a DVB-SH system using $N = 4096$ carriers with QPSK modulation, $T_g = T_u/8$, and Bandwidth $5MHz$. The frequency offset inserted before the estimator was uniform distributed between $-0.5\ f_u$ and $0.5\ f_u$, while the timing offset was uniform distributed between $-20\ T$ and $20\ T$. The estimator performance is compared in terms of error standard deviation.

Concerning the CTE task, the MS based algorithms have better performance in term of error standard deviation in AWGN channel. In particular, the ML estimator achieves the best performance. Moreover, simulation results show a cross between the performance of the MC estimator and the MMSE estimator, as predicted in Section 3.3.1. The DC algorithm has the worst performance in AWGN channel, due to the shape of the *metric* function is smoothed due to the structure of the double correlator, thus it is harder to maximize. Concerning the low-complexity algorithms, the EEWS approach achieves an evident performance improvement compared to the algorithm discussed in [54]. In multipath propagation conditions, a significant performance degradation is visible for all techniques except the DC,

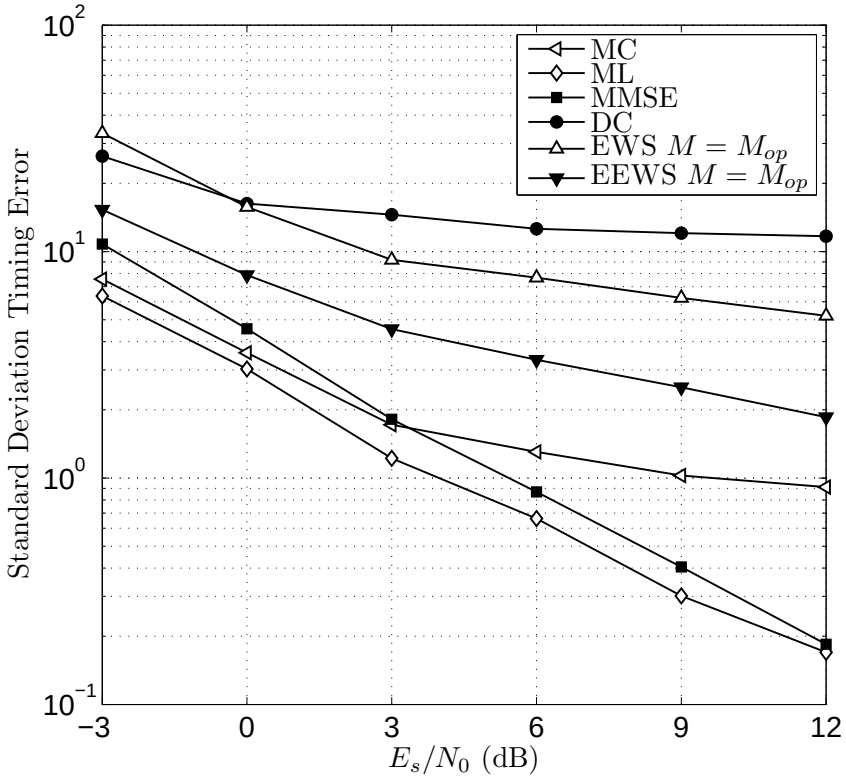

(a) AWGN channel.

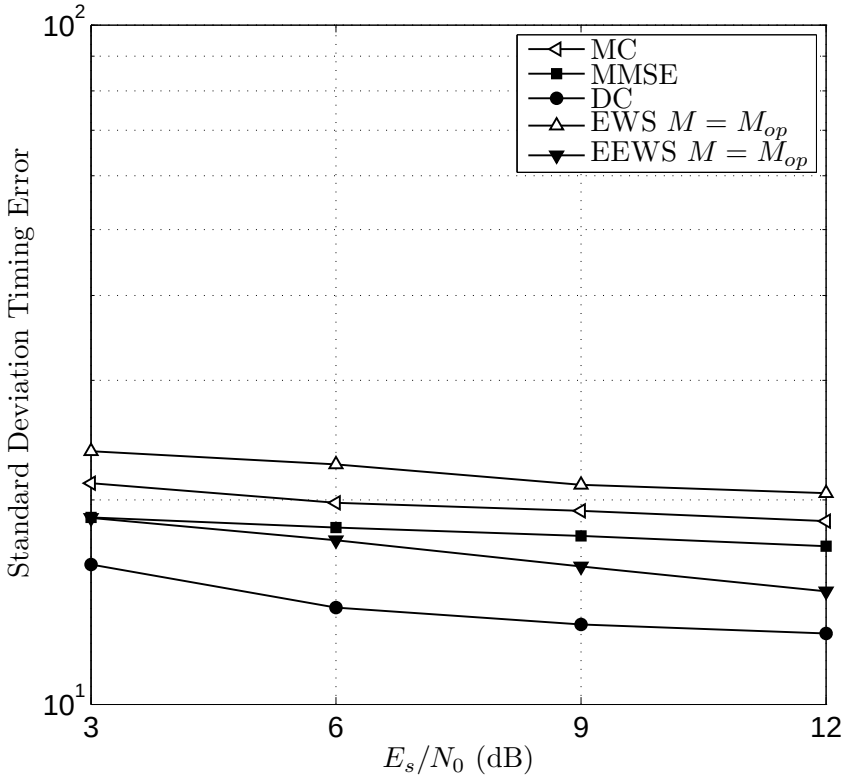

(b) Multipath fading channel.

Figure 3.6: CTE error standard deviation, using DVB-SH 4K, $T_g = T_u/4, QPSK$

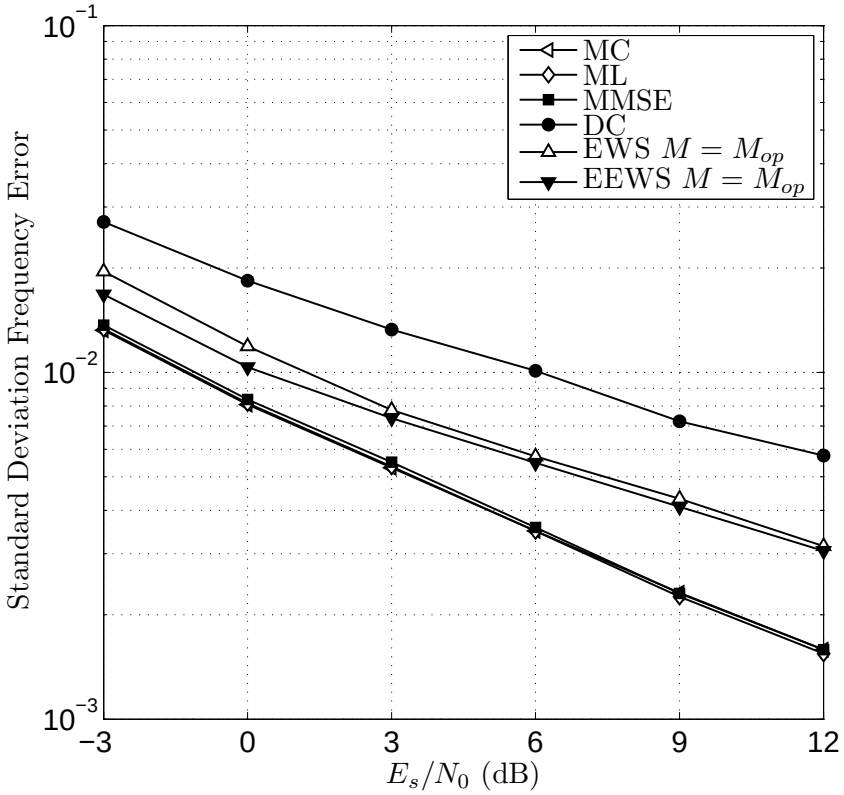

(a) AWGN channel.

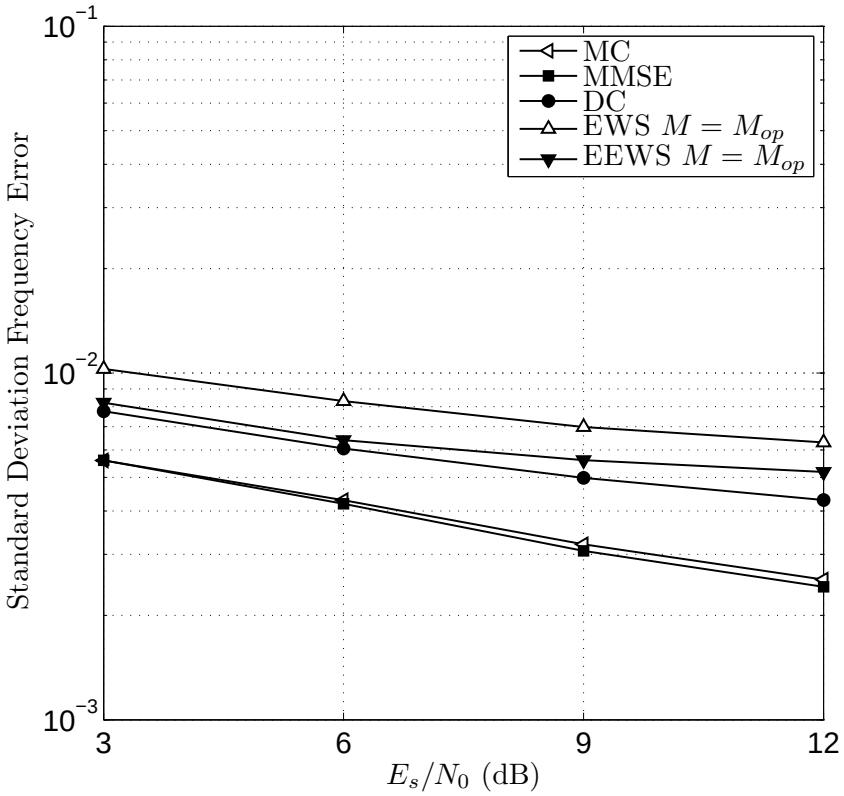

(b) Multipath fading channel.

Figure 3.7: FFE error standard deviation, using DVB-SH 4K, $T_g = T_u/4, QPSK$

that becomes the solution with the best performance, confirming the proper design for this propagation environment. In this case, EEWS is even better than MS based algorithms, because the initial part of the guard interval, which is more affected by ISI, is weighted less that final part. In Table 3.3, the power-delay profile of the considered multipath channel is shown, where the first path is due to the satellite link and the other paths are due to the complementary ground component.

As far as the FFE task is concerned, the MS based algorithms confirm again to obtain better performance, but with a minor gap with respect to the EWS based solutions. The EEWS performance is still positioned in the middle between low-complexity and high-complexity algorithms. The DC algorithm has again the worst performance in AWGN channel, but an improvement in multipath channel.

3.3.6 Considerations

We have analyzed the PRE-FFT synchronization problem keeping into consideration that, since fine tuning is performed by POST-FFT subsystems, the PRE-FFT accuracy shall only meet the minimum requirements for operations, without necessarily seek for the optimum performance at the cost of implementation complexity. We have therefore designed a new PRE-FFT algorithm aiming to strike a good trade-off between performance, robustness, and complexity. Simulation results show that this objective has been completely achieved, since the proposed algorithm places itself among the least complex approaches, while challenges, in terms of estimation accuracy, the most complex methods in both AWGN and multipath scenario, confirming also a very good robustness. Although the analysis has been presented for the DVB-SH standard, it is easily applicable to any OFDM based system.

3.3.7 Preamble based PRE-FFT Synchronization

In the previous Section we have dealt with synchronization methods which exploit the redundancy introduced by the CP in order to accomplish the PRE-FFT synchronization, without any aid from known signals. However, in order to facilitate the synchronization operation a known preamble can be inserted. For example, some standard systems as like DVB-T2 or WiMAX, provide a preamble at the beginning of each frame

In addition to CTE and FFE, a further task that can be performed with the aid of a known preamble is the frame acquisition, which consists in the detection of the

Start of Frame (SoF). This operation can be accomplished either in the time or in the frequency domain according to the strategy foreseen by the standard. Regarding those standards that do not provide any known preamble, like DVB-H and DVB-SH, the Frame acquisition is performed by the means of signalling tones, called TPS (Transmission Parameter Signalling). TPS are also in charge of informing the receiver about frame position, code rate, used modulation, and other parameters necessary to start the demodulation and the decoding operations.

In [56] we studied and assessed the advantage of a preamble insertion in those systems which do not provide one. In particular we focused on DVB-SH scenario. This study leads to a novel joint the SoF and the frequency offset estimator[4]. Numerical results show that the proposed approach can overcome CP based techniques, even for very low SNRs. Especially in systems that have to cope with very challenging scenarios, like hybrid terrestrial-satellite mobile channels.

3.4 POST-FFT Synchronization

As anticipated in Section 3.2 the first task of POST-FFT synchronization is in charge of estimating the integer part n of the carrier frequency offset normalized to f_u in order to complete frequency recovery. This task is identified as Integer Frequency Estimation (IFE). IFE is one of the most critical synchronization phases because it must be completed in the presence of residual timing errors that translates in angular rotations in the frequency domain. This problem is faced in [57], [58] and [59] with the adoption of differential POST-FFT Carrier frequency offset detection that exploits pilots belonging to two adjacent OFDM symbols in the frequency domain. This approach provides very good performance although, as all differential techniques, suffers from fast time varying channels as in wireless mobile communication. To overcome this limitation, we have faced this problem from both the point of view of signal design and receiver algorithms. In fact, in [60] we have proposed:

- A fully non-coherent approach that results from the adoption of the technique proposed in [61] and in [62] to the OFDM system. In particular, silent pilots with an ad-hoc distribution pattern are introduced substituting the conventional boosted pilots. The acquisition is then performed by a non coherent detector that, as proved in [61], is optimal and leads to performance improve-

[4] the complete scheme and results are provided in [56]

ments in POST-FFT frequency synchronization and is characterized, at the same time, by very limited complexity.

- A novel pilot pattern design aiming at avoiding overlapping positions between its pilots and pilots belonging to any of the possible replica shifted by $|n| \leq N_{max}$ positions.

Interestingly, the idea of replacing pilot symbols with nulls has already been proposed in the context of OFDM synchronization systems in [63], although applied to CFO recovery in PRE-FFT synchronization, thus leading to completely different conclusions.

The proposed solution is analytically characterized is presented in the presence of Rayleigh multipath fading channels, providing original results with respect to the literature, and is contrasted with the classical approach in a realistic scenario showing an interesting performance improvement in AWGN, and especially in Rayleigh multipath channels.

3.4.1 Pilot Pattern Design

The design of pattern P that characterizes the pilot position inside OFDM symbols is a crucial aspect for this problem. In Table 3.4(a) the pattern used in DVB-H and DVB-SH are shown as a reference. As discussed in [61], the adoption of silent pilots necessarily goes along with a special pilot pattern design, which aims at avoiding overlapping positions between pilots when matching two patterns shifted by $j > 1$ positions. In this way, the autocorrelation properties necessary to achieve good synchronization are guaranteed by the pilot positions rather than the value they assume. To adapt the design procedure presented in [61] to OFDM, it is helpful to introduce the binary sequence defining the pilot positions in the OFDM symbol as

$$\psi_k = \begin{cases} 1 & \text{if } k\text{-th subcarrier is a pilot,} \\ 0 & \text{otherwise,} \end{cases} \tag{3.29}$$

It results that ψ is a sequence of length N_a which is composed by N_p ones and $N_a - N_p$ zeros. We define the Overlapping Position Function (OPF) of $\mathcal{O}_\psi(j)$ as a function which returns the number of overlaps between a pilot pattern P and its replica shifted by j positions, defined as

$$\mathcal{O}_\psi(j) = \sum_{k=0}^{N-j-1} \psi_k \psi_{k+j} \tag{3.30}$$

In [61], the sequence design has been obtained by considering an overlapping function constrained to respect the condition

$$\begin{cases} \mathcal{O}_\psi(j) = N_p & \text{if } j = 0 \\ \mathcal{O}_\psi(j) \leq 1 & \text{otherwise} \end{cases} \tag{3.31}$$

leading to the pattern reported in table 3.4(b). This pattern can be straightforwardly applied to the problem at hand, but it is not optimal because the uncertainty region for frequency synchronization is typically smaller than the entire symbol duration, and the guard bands of the OFDM symbol have to be considered for accurate design. Therefore, a new pilot pattern sequence has been obtained applying the algorithm described in [61] with a different OPF to create a zero-overlap interval throughout $|j| < n_{max}$ with $j \neq 0$:

$$\begin{cases} \mathcal{O}_\psi(j) = N_p & \text{if } j = 0 \\ \mathcal{O}_\psi(j) = 0 & \text{if } 0 < |j| \leq n_{max} \end{cases} \tag{3.32}$$

The optimum pattern is then obtained by selecting n_{max} large enough to cover the entire uncertainty region, irrespectively of the number of overlaps out of the uncertainty region.It is worthwhile to note that, increasing n_{max}, the resulting pilot pattern which satisfies the condition in eq. (3.32) will become less dense. Since the quality of estimation depends on the number of pilots utilized, it is helpful to extend the design criterion of eq. (3.32) with a more general staircase OPF as

$$\begin{cases} \mathcal{O}_\psi(j) = N_p & \text{if } j = 0 \\ \mathcal{O}_\psi(j) = 0 & \text{if } 0 < |j| \leq n'_{max} \\ \mathcal{O}_\psi(j) \leq 1 & \text{if } n'_{max} < |j| \leq n''_{max} \\ \mathcal{O}_\psi(j) \leq 2 & \text{if } n''_{max} < |j| \leq n'''_{max} \\ \vdots & \vdots \end{cases} \tag{3.33}$$

that gives better control over the pilot distribution. The resulting pilot patterns, called Minimum Overlap Pattern (MOP), are reported in Table 3.4, considering $N_p = 25$ and $N_a = 853$, according to the DVB-SH standard. In particular, Table 3.4(d) reports the pilot pattern that satisfies a two-steps condition on OPF with $n'_{max} = 20$ and $n''_{max} = 40$. The OPF for the DVB pattern and the pattern of table 3.4(d) are graphically reported in figures 3.8 and 3.9, respectively, showing clearly the zero-overlap region for the proposed pattern.

Table 3.4: Presented Pilot patterns.

(a) Pattern used in DVB-H and DVB-SH for continual pilots.

0,48,54,87,141,156,192,201,255,279,282,333,432,450,
483,525,531,618,636,714,759,765,786,813,852

(b) Pattern presented in [62] that satisfies the condition in eq. (3.31).

0,1,3,7,12,20,30,44,65,80,96,122,147,181,
203,251,289,360,400,474,564,592,661,774,821, $\cdots$

(c) Pattern that satisfies the condition in eq.(3.32).

0,21,43,66,90,115,141,168,196,225,255,287,
318,351,386,425,463,513,549,634,705,763,839, $\cdots$

(d) Pattern that satisfies the condition in eq. (3.33).

0,21,43,66,90,115,141,168,196,225,255,286,318,351,
385,420,456,493,531,571,612,653,695,737,780, $\cdots$

(e) Pattern that satisfies the condition in eq. (3.33), and that does not allow any pilots in the first and in the last N_{max} sub carriers.

35,56,78,101,125,150,176,203,231,260,290,321,353,
386,420,455,491,528,566,606,647,688,730,772,815

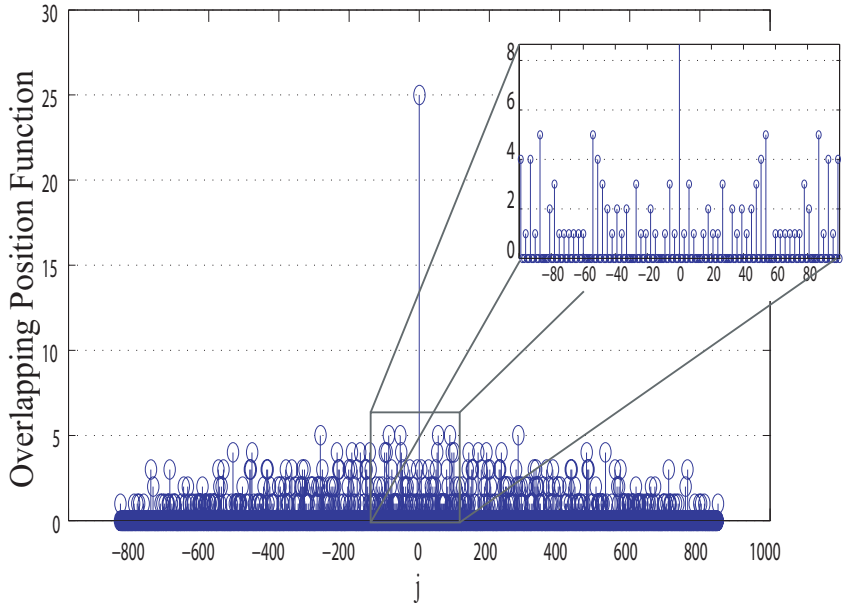

Figure 3.8: Overlapping position function of DVB pattern illustrated in 3.4(a)

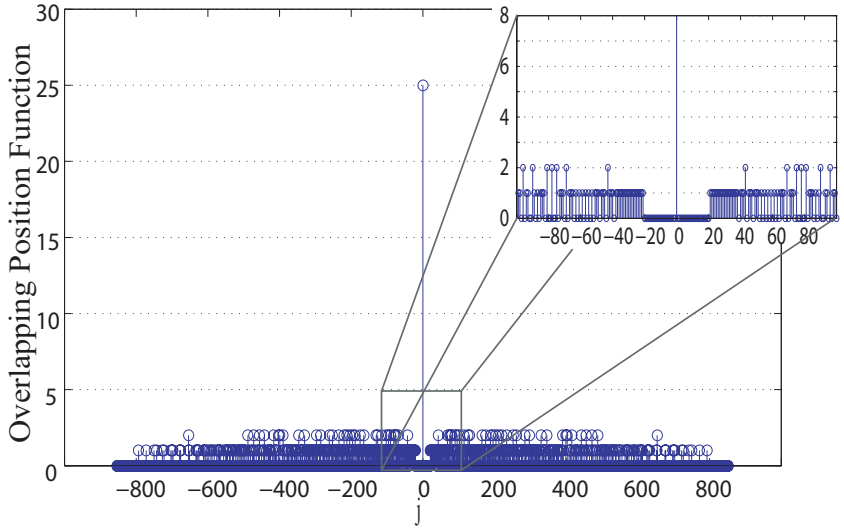

Figure 3.9: Overlapping position function of minimum overlap pattern illustrated in 3.4(d)

The strength of the pattern designed according to the criteria illustrated above is that it is possible to adopt silent pilots, simply defined as

$$p_{k,\ell} = 0, \quad k \in P \tag{3.34}$$

The benefits of silent pilots are discussed in detail in the following section.

3.4.2 Detector Definitions

3.4.2.1 Silent Detector

In [61] it has been proved that the optimal decision statistics for silent pilots according to the Maximum Likelihood approach is provided by

$$S_\ell(i) = \sum_{k \in P} |y_{k+i,\ell}|^2 \tag{3.35}$$

that is the energy evaluated over the observation window according to the pattern P. This is also an intuitive result because having introduced silent pilots distributed according to a pattern that does not overlap with itself when shifted, it is straightforward that the received energy is minimal when the receiver is synchronized. Accordingly, the decision is taken by exploring the uncertainty region and selecting the minimum accumulated variable according to

$$\widehat{n} = \arg\min_i S_\ell(i) \tag{3.36}$$

where $i \in [-N_{max}; N_{max}]$, being N_{max} the maximum frequency shift specification. The main advantage of this detector is its robustness against the angular rotations induced by timing errors, that directly translates in performance improvements as shown in the following. In addition, it is possible to accumulate over several OFDM symbols to make the decision more accurate by simply generalizing the expression of the accumulated metric over u OFDM symbols, as

$$S_\ell^{(u)}(i) = \sum_{j=0}^{u-1} S_{\ell+j}(i) \tag{3.37}$$

Of course, the accumulation over more OFDM symbols comes at the price of increased delay and receiver complexity.

3.4.2.1.1 Analytical Analysis The samples $y_{k,\ell}$ at the output of the FFT are Gaussian random variables (r.v.s) with mean value and variance given by

$$y_{k,\ell} \sim \begin{cases} N(0,\sigma_n^2) & H_1(k \in P) \\ N(0,\sigma_\rho^2) & H_0(k \notin P) \end{cases} \tag{3.38}$$

where $\sigma_\rho^2 = \sigma_H^2 \frac{E_s}{2} + \sigma_n^2$, $\sigma_n^2 = N_0/2$, and we have indicated with H_1 and H_0 the hypotheses of correct and incorrect alignment, respectively. In general, operating in the frequency domain it results

$$R_{k,j}(\ell) = E[y_{k,\ell} y_{j,\ell}^*] \neq 0 \tag{3.39}$$

so that the variables of eq. (3.38) are not independent. However, in the presence of severe multipath and considering that the pattern P does not contain contiguous subcarriers, it is possible to assume that the $y_{k,\ell}$ samples are mutually independent, so that the variable $S_\ell(i)$ of eq. (3.35) results to be a χ^2 r.v. as

$$S_\ell(i) \sim \begin{cases} \chi^2_{2N_p}(0,\sigma_n^2) & H_1(k \in P) \\ \chi^2_{2N_p}(0,\sigma_\rho^2) & H_0(k \notin P) \end{cases} \tag{3.40}$$

which is the statistics for the case of accumulation over a single OFDM symbol, while, in the general case of accumulation over u OFDM symbols, the resulting metric $S_\ell^{(u)}(i)$ is given by

$$S_\ell^{(u)}(i) \sim \begin{cases} p_{S|H_1}(S|H_1) = \chi^2_{2hN_p}(0,\sigma_n^2) & H_1 \\ p_{S|H_0}(S|H_0) = \chi^2_{2hN_p}(0,\sigma_\rho^2) & H_0 \end{cases} \tag{3.41}$$

Accordingly, the probability of correct decision is given by

$$P_d = \text{Prob}(\hat{n} = n) = \text{Prob}(S_n < S_i \quad \forall i \neq n)$$

that can be expressed as

$$P_d = \int_0^\infty \left(\int_t^\infty p_{S|H_1}(r|H_1) dr \right)^{2N_{max}} p_{S|H_0}(t|H_0) dt \tag{3.42}$$

thus, the probability of false acquisition, is gives by

$$P_{fa} = 1 - P_d \tag{3.43}$$

3.4.2.2 Differential Detector

In the case of traditional pilots, a differential detector can be adopted in order to cope with the effect of the unknown timing offset m and the unknown CTF $H_{k,\ell}$, as described in [59]. This means that the detector needs two OFDM symbols to perform the estimation. We define the metric $M_\ell(i)$ as correlation of FFT output samples of two consecutive OFDM symbols as

$$M_\ell(i) = \sum_{k \in P} y_{k+i,\ell} \cdot y^*_{k+i,\ell+1} \tag{3.44}$$

where $i \in [-N_{max}; N_{max}]$. The frequency translation n can be detected, by searching the index i which maximizes the energy of the metric $M_\ell(i)$: [5]

$$\widehat{n} = \arg\max_i |M_\ell(i)|^2 \tag{3.45}$$

Alternatively to detect n it possible to search the search the index i that maximize the real part of metric $M_\ell(i)$

$$\widehat{n} = \arg\max_i Re M_\ell(i) \tag{3.46}$$

This solution has better performance compared to (3.45), but is very weak in case of misalignment of differential detector.

3.4.3 Performance Comparison

Monte Carlo simulations are presented in the following to validate the proposed analytical model and evaluate the detector performance in terms of probability of false acquisition, P_{fa}. The simulation scenario considers a DVB-SH system using $N = 1024$ carriers, with QPSK modulation, $T_g = T_u/8$,uniform frequency offset in $[-20\ f_u, 20\ f_u]$, uniform residual timing offset in $[-10\ T, 10\ T]$.

The proposed approach is contrasted with the Differential Detector defined in section 3.4.2.2 that exploits pilots boosted in power by a factor $\beta^2 = 16/9$ according to standard DVB-H and DVB-SH. Two different pilot patterns are considered: the original DVB Pattern, reported in table 3.4(a), and the proposed MOP reported in table 3.4(d). In order to obtain a fair comparison the number of pilots is equal to $N_p = 25$ for both patterns. For the silent detector of eq. (3.36), pilots are inserted according to the original DVB Pattern, and the proposed MOP reported in table

[5] It is also possible to search for the index i which maximizes the absolute value of metric as proposed in [58]

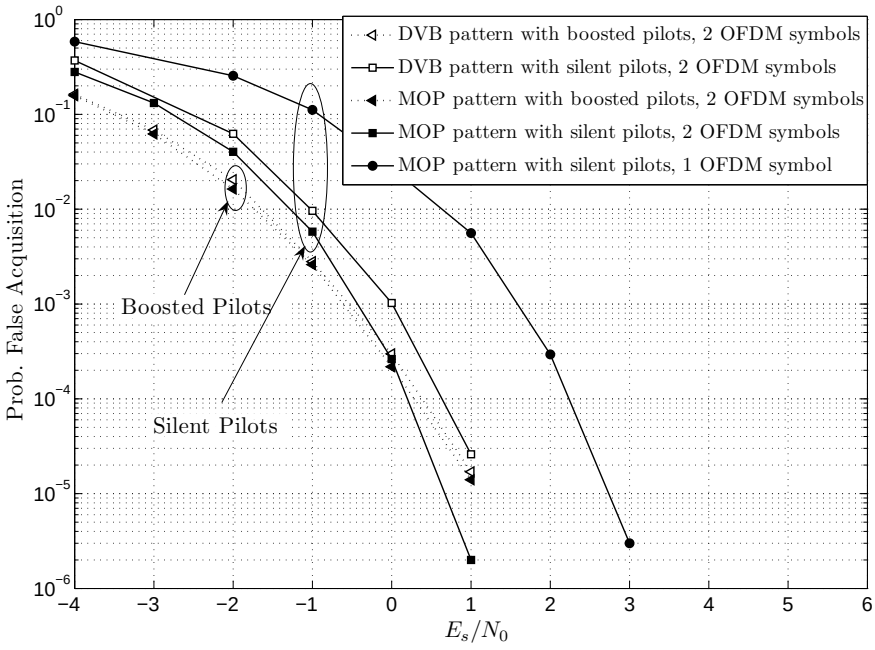

Figure 3.10: Numerical results in AWGN channel

3.4(e), which is a slight variation of the pattern 3.4(d) to prevent to insert pilots close to the guard bands. The silent detector metric is accumulated over a single symbol OFDM and over 2 OFDM symbols, i.e. eq. (3.37) with $u = 2$, in order to obtain a fair comparison with the differential detector of eq. (3.45).

The performance is evaluated in AWGN, and in two different frequency-selective channels. The first, identified as *multipath 1*, is ideally-uncorrelated in frequency, and the second, *multipath 2*, is characterized by seven equi-spaced and equi-energy paths.

Figure 3.10 reports P_{fa} versus the signal to noise ratio E_s/N_0 in AWGN, and it shows that the performance is close, even though the Silent Detector has a steeper characteristic curve that crosses the Differential Detector curve at P_{fa} equal to $3 \cdot 10^{-4}$. Moreover, while the MOP adoption does not significantly improve the performance of the Differential Detector, in the case of the Silent Detector it brings a gain of 0.5 dB, corresponding to P_{fa} equal to 10^{-4}. As expected, the Silent Detector which use a single OFDM symbol, i.e. eq. (3.37) where $h = 1$ provide inferior performance, losing about 2 dB at P_{fa} equal to $3 \cdot 10^{-4}$.

In multipath scenarios, as shown in figure 3.11, silent pilots lead to more significant improvements. In particular, in *multipath 1* the Silent Detector has better

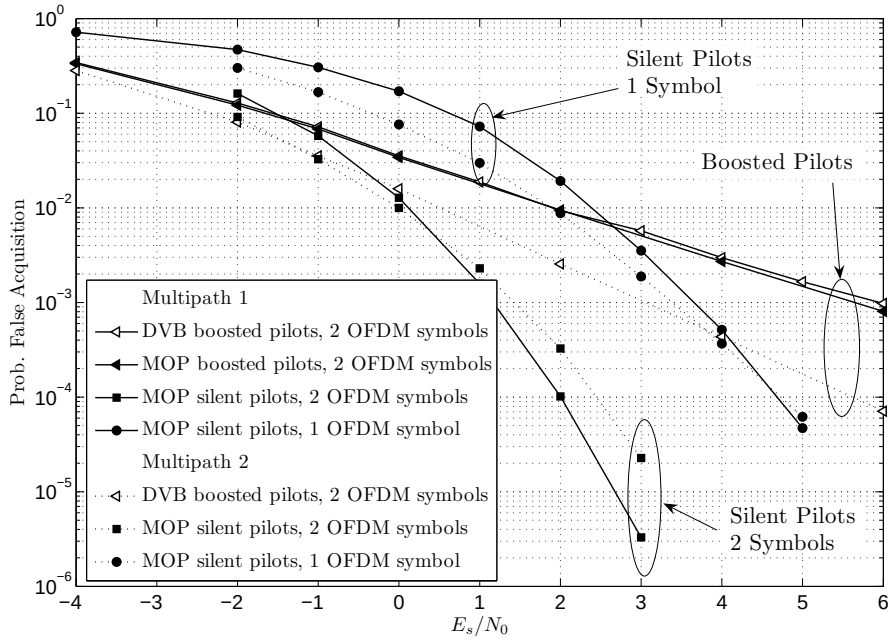

Figure 3.11: Numerical results in multipath fading channel

performance compared to the classic Differential Detector, even when the metric has been accumulated over a single OFDM symbol. Such a dramatic improvement in fading channels are due to the fact that the hypotheses of correct alignment H_1 are not afflicted by an unknown CTF, as shown in (3.40). This trend is confirmed by the analytical model presented in section 3.4.2.1.1 that perfectly matches with simulations.

3.4.4 Considerations

Simulation results show that the Silent Detector used with the proposed pattern has better performance compared to traditional Differential Detector in particular in the case of severe multipath fading channel. On the other hand, it is worthwhile to note that Silent Pilots cannot be used in following data aided synchronization phases, such as channel and timing estimation. However, this can be considered as a second order effect because channel and timing estimation usually exploit scattered pilots which intersect in minimal part with the continuous pilots in which silent symbols are inserted. In any case, to reduce the overhead, it is possible to insert silent pilots only in certain OFDM symbols, typically at the beginning of a frame.

Chapter 4

Channel Estimation

The greatest of all gifts is the power to estimate things at their true worth.

Maximes, François de La Rochefoucauld

As anticipated in Chapter 1 one of the advantage offered by OFDM is its ability to cope with strongly dispersive channels using low-complexity equalizers, with a single tap per subcarrier. This is due to the fact that propagation channels which are frequency selective over the entire OFDM bandwidth may appear non-selective on each narrowband subcarrier. In particular, this is crucial for the case of OFDM single-frequency networks, where in order to achieve seamless radio coverage, identical signals are transmitted from widely separated sites. In this case, signal replicas may come with very large differential delays, giving rise to very sparse channel profiles.

Clearly, the equalizer will perform successfully if and only if accurate estimation of the Channel Transfer Function (CTF), or equivalently of the Channel Impulse Response (CIR), is performed at the receiver. In other words, channel estimation becomes *the* critical function which largely determines the overall receiver performance. For this reason, OFDM channel estimation is normally Data-Aided (DA) whereby known pilots are multiplexed into OFDM symbols, usually drawing a regular pattern of known subcarriers with constant inter-pilot frequency spacing. Using these pilots, channel estimation is performed in two steps: first, the CTF is punctually estimated on pilot subcarriers; then, channel estimates are interpolated over data subcarriers.

4.1 Existing Channel Estimation Methods

In general, DA channel estimation methods differ in the way they interpolate or filter punctual DA Least Squares (DA-LS) channel estimates over data subcarriers. This can be accomplished using two-dimensional (2D) time-frequency Wiener Filtering (WF) [64], which is optimal in the Minimum Mean Square Error sense. Unfortunately, 2D-WF requires perfect knowledge of the channel statistics (KCS) and is burdened by large complexity. Complexity can be reduced if one abandons two-dimensional estimation in favor of a separate time and frequency approach. In [65], Hoeher et al. showed that by applying one-dimensional Wiener filters over time and frequency it is possible to reduce complexity and achieve good performance, if KCS is available. On the other hand, channel estimation can be accomplished by elaborating raw estimates in the time-domain using a DFT based scheme. In [66], the MMSE channel estimator working in the time domain, which also requires complete KCS, has been proposed. In order to reduce computational complexity, using the singular value decomposition, several low-rank approximations to the MMSE estimator have been proposed in [67], [68]. On a more pragmatic basis, methods which require the minimum possible KCS and are applicable to any kind of Power Delay Profile (PDP) and in particular to sparse channels are appealing. In [69], Morelli and Mengali compared the MMSE approach with Maximum Likelihood channel estimation where complete KCS is not required, but only the PDP domain. This latter approach works well with dense multipath channels and quasi-uniform profiles. KCS agnostic channel estimation can be achieved by interpolating the punctual DA-LS estimates using a DFT-based scheme without any elaboration in the time domain. Unfortunately, simplicity here goes along with mediocre performance [68], and much research work is being devoted to improving this approach without increasing complexity in any significant way.

4.1.1 LS Channel Estimation

Starting from the generic system model provided in Section 1.5, let us consider a generic pilot tone positioned at the k-th subcarrier in the ℓ-th OFDM symbol. The punctual LS estimation of the CTF is given by:

$$\hat{H}_{k,\ell}^{LS} = \frac{y_{k,\ell}}{p_{k,\ell}} = H_{k,\ell} + \frac{n_{k,\ell}}{p_{k,\ell}} \qquad k \in P(\ell) \tag{4.1}$$

As discussed previously, DA channel estimation methods differ in the way they interpolate the punctual observations, $\hat{H}_{k,\ell}^{LS}$, over data subcarriers. We consider

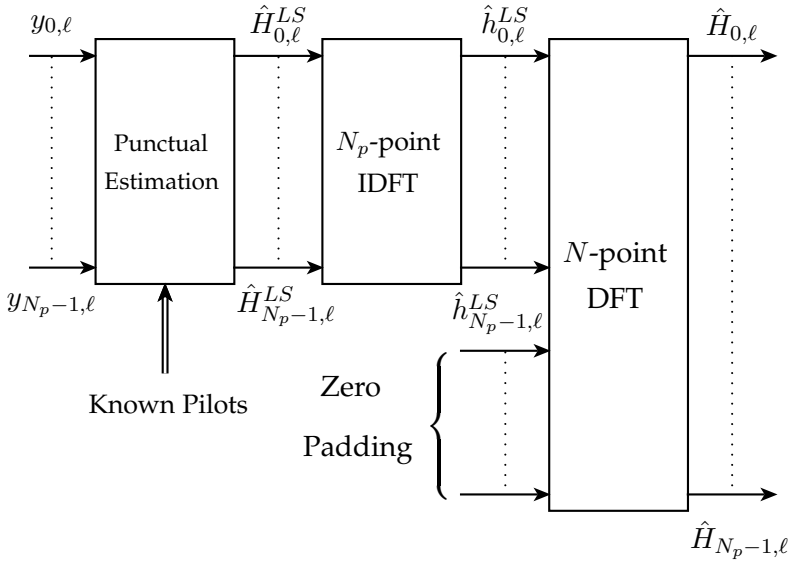

Figure 4.1: Block diagram of Channel Estimator based on DFT interpolation.

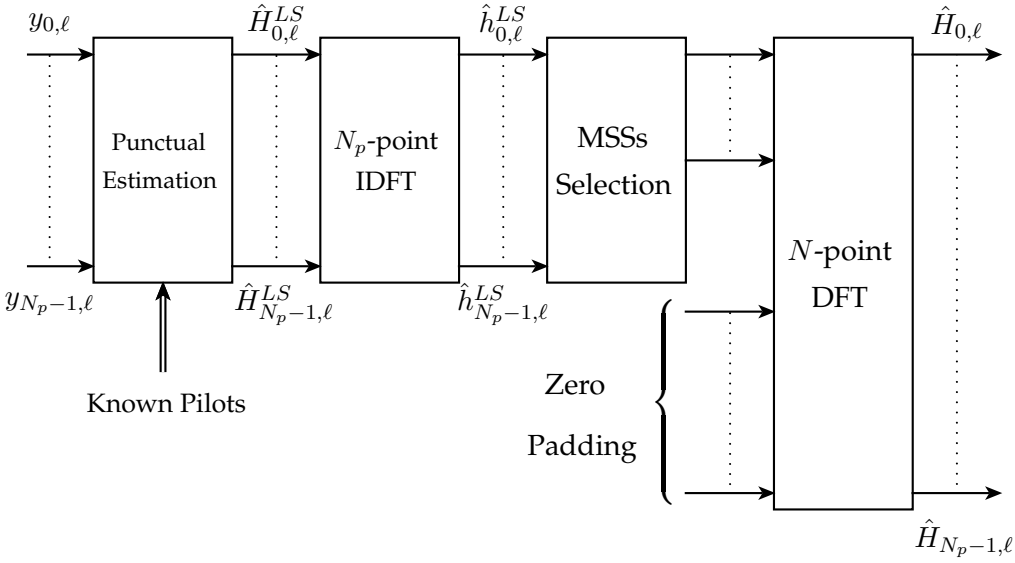

Figure 4.2: Block diagram of Channel Estimator based on Most Significant Sample selection.

here the DFT interpolation approach, which would be optimal in the absence of noise and with sufficient pilot density. Under the assumption that pilot symbols are present in all OFDM symbols, time interpolation is not strictly necessary. Therefore we only focus on frequency-domain interpolation, which is performed in three steps. First, an IDFT is applied to the vector of punctual estimates to produce a CIR estimate, $\hat{h}_{i,\ell}$, as follows

$$\hat{h}_{i,\ell} = \frac{1}{N_p} \sum_{k'=0}^{N_p-1} \hat{H}^{LS}_{k(k'),\ell}\, \mathrm{e}^{-\jmath 2\pi k' i/N_p} \quad i = 0, \ldots, N_p - 1 \tag{4.2}$$

where $k(k')$ is an indexing function introduced to point out the fact that the CTF estimates are now compacted into the first N_p values for k'. Then, assuming that $N_p > L$, CTF estimation over the entire frequency comb can be obtained by zero padding the CIR over the entire OFDM symbol duration:

$$\hat{\tilde{h}}^{ZP}_{\ell} = \{\underbrace{\hat{h}_{0,\ell}, \ldots, \hat{h}_{N_p-1,\ell}}_{N_p} \underbrace{0, \ldots, 0}_{N-N_p}\} \tag{4.3}$$

and finally by applying a DFT:

$$\hat{\tilde{H}}^{LS}_{\ell} = DFT\{\hat{h}^{ZP}_{\ell}\} \tag{4.4}$$

It is possible to compute the MSE associated to this DA estimation/DTF interpolation method in closed form. Let us define the MSE as

$$\mathrm{MSE} \doteq E_\ell \left[\frac{1}{N} \sum_{k=0}^{N-1} \left| H_{k,\ell} - \hat{H}_{k,\ell} \right|^2 \right] \tag{4.5}$$

Following lines similar to [68], and applying the Parseval Theorem, the MSE expression for LS, $\mathrm{MSE}(LS)$, is given by:

$$\mathrm{MSE}(LS) = \frac{1}{N} \sum_{k=0}^{N-1} E\left[\left| H_k - \hat{H}^{LS}_k \right|^2 \right] \overset{\text{Parseval}}{=} \sum_{i=0}^{N_p-1} E\left[|h_i - \hat{h}_i|^2 \right] = \frac{1}{\rho} \tag{4.6}$$

Where $\rho = \beta^2 E_s/N_0$ represents the pilot energy to noise ratio. As we have just shown, here simplicity goes along with mediocre performance [68]. In the next Section we will see how it is possible to notably improve the MSE by adopting a suitable sample selection strategy, without increasing complexity and without require KCS.

4.2 Most Significant Samples Selection

The main idea to achieve this goal is the following: after the IDFT, not all the CIR samples are significant, because many may correspond to delays where no propagation channel paths are actually present. *Therefore, if one can devise a technique to decimate the CIR and retain only the significant samples, performance can be improved without complexity increase.* With this aim, Minn et al. [70] proposed to select only the J strongest samples, identified here as the Most Significant Samples (MSSs) of the CIR estimate, J being obviously a crucial design parameter. It is shown here that in the ideal case where J equals the actual number of non-zero channel taps, N_t, very good performance can be achieved; but when J differs from N_t, performance degrades rapidly. Instead of pre-determining a-priori the total MSS number, Kang et al. [71] proposed to select those samples for which the square module is above a threshold. We refer to this approach as Threshold Crossing Selection (TCS). In this way, a dynamic number of MSSs is selected per OFDM symbol. It is clear that the threshold value is critical to the algorithm performance. While in [71] the threshold was set according to heuristics, in [72] a genie-aided approach was followed, based again on ideal TCS.

Our contribution in this contest is threefold. First, in Section 4.3, by defining the optimal set of selected samples, which minimizes the MSE, in both instantaneous and average senses, we derive lower bounds on the MSE performance for any MSS selection strategy. Comparing the obtained lower bounds with MMSE channel estimation performance, we conclude that MSS-based channel estimation has the potential to reach comparable performance with respect to the optimum MMSE approach, in particular when the number of pilots is significantly larger than the number of channel paths (as customary). Second, in Section 4.4.1 we analytically derive the optimum threshold value for TCS in the minimum MSE sense. We show that, by using the optimum threshold, TCS can tightly approach MMSE at high signal-to-noise ratio values. Unfortunately, the optimal threshold depends on the actual channel PDP. For this reason, in Section 4.4.1.2, we propose a sub-optimal approach for threshold setting, which we show to yield comparable performance to the optimal threshold case with robustness against PDP variations. Third, in Section 4.4.2, we propose two novel MSS selection strategies, identified as Instantaneous Energy Selection (IES) and Average Energy Selection (AES), which do not require KCS, but only estimation of the received SNR. In particular, IES, as well as TCS, aims to decimate CIR estimate samples considering only their instantaneous

energy, hence both IES and TCS are oriented towards instantaneous selection of MSSs. On the other hand, AES, which is oriented towards a windowed selection of MSSs, extends the observation window over several OFDM symbols, and, as a consequence of noise reduction, it closely approaches the MMSE performance, even for low SNR.

4.3 MSE Lower Bounds

As anticipated in previous Section, not all CIR estimate samples are significant; in fact, many samples may correspond to delays where no propagation channel paths are actually present, and consequently they only contain noise. Therefore, it is possible to reduce drastically the noise presence, especially when the CIR is very sparse, by decimating the impulse response into the subset $\mathcal{S}(\ell)$ of *most significant samples* after the IDFT:

$$\hat{h}_{i,\ell}^{MSS} = \begin{cases} \hat{h}_{i,\ell} & \text{if } i \in \mathcal{S}(\ell) \\ 0 & \text{if } i \notin \mathcal{S}(\ell) \end{cases} \tag{4.7}$$

The complete block diagram is shown in Fig. 4.2. Obviously, the critical aspect of this method is the strategy used in forming $\mathcal{S}(\ell)$, upon which the MSE is completely dependent. It is both interesting and essential to obtain a lower bound on the MSE for DA channel estimation based on MSS selection, defined as the value obtained for the optimal set of samples, $S_{opt}(\ell)$. The first step towards the achievement of this goal is to model statistically the CIR estimates, $\hat{h}_{i,\ell}$. Substituting (4.1) in (4.2), we obtain

$$\hat{h}_{i,\ell} = \frac{1}{N_p}\left(\sum_{k'=0}^{N_p-1} H_{k(k'),\ell}\, \mathrm{e}^{-\jmath 2\pi k' i/N_p} + \sum_{k'=0}^{N_p-1} \frac{n_{k(k'),\ell}}{p_{k(k'),\ell}}\, \mathrm{e}^{-\jmath 2\pi k' i/N_p}\right) \quad i = 0, \ldots, N_p - 1 \tag{4.8}$$

Thus, we can write the CIR estimate as the sum of the correct value, $h_{i,\ell}$, and a noise component, $\nu_{i,\ell}$:

$$\hat{h}_{i,\ell} = h_{i,\ell} + \nu_{i,\ell} \tag{4.9}$$

where:

$$\nu_{i,\ell} = \frac{1}{N_p} \sum_{k'=0}^{N_p-1} \frac{n_{k(k'),\ell}}{p_{k(k'),\ell}} \mathrm{e}^{-\jmath 2\pi k' i/N_p} \tag{4.10}$$

Due to the statistical independence of the $n_{k,\ell}$ samples, the noise components are distributed as zero-mean complex Gaussian random variables with variance $1/\rho N_p$:

$$\nu_{i,\ell} \sim \mathcal{N}_c\left(0, \frac{1}{\rho N_p}\right) \tag{4.11}$$

where $\rho = \beta^2 E_s/N_0$ represents the pilot energy to noise ratio, and $\mathcal{N}_c\left(\mu, \sigma^2\right)$ represents the probability density function of a complex Gaussian random variable with mean μ and variance σ^2. Therefore, the CIR estimate samples, $\hat{h}_{i,\ell}$, are also complex Gaussian random variables distributed as:

$$\hat{h}_{i,\ell} \sim \begin{cases} \mathcal{N}_c\left(0, \frac{1}{\rho N_p} + \gamma_i^2\right) & \text{if } i \in \mathcal{C} \\ \mathcal{N}_c\left(0, \frac{1}{\rho N_p}\right) & \text{if } i \notin \mathcal{C} \end{cases} \quad i = 0, \ldots, N_p - 1 \tag{4.12}$$

where $\mathcal{C}$ is the set of indices corresponding to those time samples where propagation paths are actually present, i.e. $i \in \mathcal{C}$ iff $\gamma_{\mathrm{i}}^2 \neq 0$.

In selecting or rejecting any CIR estimate sample, four events are possible:

Noise Excision (NE): A CIR estimate sample, corresponding to a delay where no propagation channel path is present, is correctly rejected. This corresponds to the very reason at the heart of MSS, and occurs with probability P^{NE}.

Noise Holding (NH): A CIR estimate sample, corresponding to a delay where no propagation channel path is present, is reckoned as significant. This case contributes to the MSE with the noise component contained in the CIR estimate, and occurs with probability $P^{\mathrm{NH}} = 1 - P^{\mathrm{NE}}$.

Path Excision (PE): A CIR estimate sample, corresponding to a delay where a propagation channel path is present, is rejected. This case contributes to the MSE with the neglected path energy, and occurs with probability P^{PE}.

Path Holding (PH): A CIR estimate sample, corresponding to a delay where a propagation channel path is present, is reckoned as significant. This case contributes to the MSE with the noise component contained in the CIR estimate, and occurs with probability $P^{\mathrm{PH}} = 1 - P^{\mathrm{PE}}$.

Considering (4.7) and (4.9), the estimation square errors $|\varepsilon_{i,\ell}|^2 = |h_{i,\ell} - \hat{h}_{i,\ell}^{MSS}|^2$ corresponding to the four events are given by:

$$|\varepsilon_{i,\ell}|^2 = \begin{cases} 0 & \text{if } i \notin \mathcal{C} \wedge i \notin \mathcal{S}(\ell) \quad \text{Noise Excision} \\ |\nu_{i,\ell}|^2 & \text{if } i \notin \mathcal{C} \wedge i \in \mathcal{S}(\ell) \quad \text{Noise Holding} \\ |h_{i,\ell}|^2 & \text{if } i \in \mathcal{C} \wedge i \notin \mathcal{S}(\ell) \quad \text{Path Excision} \\ |\nu_{i,\ell}|^2 & \text{if } i \in \mathcal{C} \wedge i \in \mathcal{S}(\ell) \quad \text{Path Holding} \end{cases} \tag{4.13}$$

The overall Square Error (SE) for the ℓ-th OFDM symbol can therefore be written as the sum of three contributions from, respectively, noise holding, path excision, and path holding:

$$\mathrm{SE}(\ell) = \sum_{i=0}^{N_p-1} |\varepsilon_{i,\ell}|^2 = \sum_{i \in \mathcal{S}(\ell) \setminus \mathcal{C}} |\nu_{i,\ell}|^2 + \sum_{i \in \mathcal{C} \setminus \mathcal{S}(\ell)} |h_{i,\ell}|^2 + \sum_{i \in \mathcal{S}(\ell) \cap \mathcal{C}} |\nu_{i,\ell}|^2 \tag{4.14}$$

where $B \setminus A$ represents the relative complement of A in B (i.e. $B \setminus A = \{x \in B \,|\, x \notin A\}$). Note that, if $\mathcal{S}(\ell)$ is a subset of $\mathcal{C}$, $\mathcal{S}(\ell) \subseteq \mathcal{C}$, then NH is always avoided. However, the latter is necessary but not sufficient for the optimality of $\mathcal{S}(\ell)$ in the minimum SE sense. In fact, it is interesting to note that $S_{opt}(\ell)$ can be strictly smaller than $\mathcal{C}$. Intuitively, if a sample contains an actual CIR tap, but this is overcome by noise, it pays off to decimated it out of the estimation comb. The necessary and sufficient condition on the optimality of $\mathcal{S}(\ell)$ is that $i \in \mathcal{S}(\ell)$ iff $|h_{i,\ell}|^2 > |\nu_{i,\ell}|^2$, therefore

$$\mathcal{S}_{opt}(\ell) \equiv \left\{\text{all } i \text{ such that } |h_{i,\ell}|^2 > |\nu_{i,\ell}|^2 \,, \quad i = 0, \ldots, N_p - 1\right\} \tag{4.15}$$

Proof. $\mathrm{SE}(\ell)$ is the sum of N_p non-negative terms, $\mathrm{SE}(\ell) = \sum_{i=0}^{N_p-1} |\varepsilon_{i,\ell}|^2$. For each i we can actually have two cases, obtained by grouping holding and excision[1] events:

$$|\varepsilon_{i,\ell}|^2 = \begin{cases} |\nu_{i,\ell}|^2 & \text{if } i \in \mathcal{S}(\ell) \qquad \text{Holding} \\ |h_{i,\ell}|^2 & \text{if } i \notin \mathcal{S}(\ell) \qquad \text{Excision} \end{cases} \quad \forall \quad i = 0, \ldots, N_p - 1 \tag{4.16}$$

Therefore, the minimum $\mathrm{SE}(\ell)$ is obtained by minimizing each term of the above sum separately:

$$\mathrm{SE}_{min}(\ell) = \min \mathrm{SE}(\ell) = \sum_{i=0}^{N_p-1} \min\left\{|\nu_{i,\ell}|^2, |h_{i,\ell}|^2\right\} \tag{4.17}$$

Hence, if and only if $|h_{i,\ell}|^2 > |\nu_{i,\ell}|^2$ for all $i \in \mathcal{S}(\ell)$, and $|h_{i,\ell}|^2 < |\nu_{i,\ell}|^2$ for all $i \notin \mathcal{S}(\ell)$, then $\mathrm{SE}(\ell) = \mathrm{SE}_{min}(\ell)$. Considering that both $|h_{i,\ell}|^2$ and $|\nu_{i,\ell}|^2$ are continuous random variables, and thus, the probability to have $|h_{i,\ell}|^2 = |\nu_{i,\ell}|^2$ is null, the above conditions can be can expressed as in (4.15).

□

Although it is clear that only a genie-aided receiver could find the $S_{opt}(\ell)$ as defined above, this is still a very useful objective even for practical receivers, as

[1] Note that in case $i \notin \mathcal{C}$ it holds $|h_{i,\ell}|^2 = 0$

discussed in Sections 4.4.1 and 4.4.2. Here, it is important to derive the performance limits that correspond to the use of $S_{opt}(\ell)$. In this case, the SE for the ℓ-th OFDM symbol reduces to

$$\mathrm{SE}_{min}(\ell) = \sum_{i \in \mathcal{C} \setminus \mathcal{S}_{opt}(\ell)} |h_{i,\ell}|^2 + \sum_{i \in \mathcal{S}_{opt}(\ell)} |\nu_{i,\ell}|^2 \tag{4.18}$$

By averaging over the channel and noise statistics, it can be shown that the resulting lower bound on MSE, achievable by using instantaneously the optimum set of samples $S_{opt}(\ell)$, and identified as $\mathrm{MSE}(opt)$, is given by:

$$\mathrm{MSE}(opt) = E[\mathrm{SE}_{min}(\ell)] = \sum_{i \in \mathcal{C}} \frac{\gamma_i^2}{1 + \rho N_p \gamma_i^2} \tag{4.19}$$

The analytical derivation of Eq. (4.19) is provided in following. Let's consider the Rayleigh random variables $\alpha_{h_i} = |h_{i,\ell}|$ and $\alpha_{\nu_i} = |\nu_{i,\ell}|$. The MSE achievable by using the optimum set of samples $S_{opt}(\ell)$, after considerable algebra, can be expressed by:

$$\begin{aligned} \mathrm{MSE}(opt) &= E\left[\mathrm{SE}_{min}(\ell)\right] = \\ &= \sum_{i \in \mathcal{C}} \left\{ \int_0^{\infty} \left(\int_0^{\alpha_{\nu_i}} \alpha_{h_i}^2 p_{\alpha_{h_i}}(\alpha_{h_i})\, d\alpha_{h_i} \right) p_{\alpha_{\nu_i}}(\alpha_{\nu_i})\, d\alpha_{\nu_i} + \right. \\ &\qquad \left. + \int_0^{\infty} \left(\int_0^{\alpha_{h_i}} \alpha_{\nu_i}^2 p_{\alpha_{\nu_i}}(\alpha_{\nu_i})\, d\alpha_{\nu_i} \right) p_{\alpha_{h_i}}(\alpha_{h_i})\, d\alpha_{h_i} \right\} \end{aligned} \tag{4.20}$$

where the corresponding p.d.f. of which are given by:

$$\begin{aligned} p_{\alpha_{h_i}}(\alpha_{h_i}) &= \frac{2\alpha_{h_i}}{\gamma_i^2} \mathrm{e}^{-\frac{\alpha_{h_i}^2}{\gamma_i^2}} \\ p_{\alpha_{\nu_i}}(\alpha_{\nu_i}) &= 2\rho N_p \alpha_{\nu_i} \mathrm{e}^{-\rho N_p \alpha_{\nu_i}^2} \end{aligned} \tag{4.21}$$

Substituting (4.21) in (4.20), and, after simple calculus and considerable algebra, it can be found that:

$$\mathrm{MSE}(opt) = \sum_{i \in \mathcal{C}} \left[\frac{\gamma_i^2}{(1 + \gamma_i^2 \rho N_p)^2} + \frac{\gamma_i^4 \rho N_p}{(1 + \gamma_i^2 \rho N_p)^2} \right] = \sum_{i \in \mathcal{C}} \frac{\gamma_i^2}{1 + \rho N_p \gamma_i^2} \tag{4.22}$$

It is very interesting to note that the result coincides with the MMSE expression derived in [68], [69].

It is hard to presume a-priori that the average performance associated to instantaneous optimal selection, $\mathrm{MSE}(opt)$, corresponds to the MMSE even if they come from very different assumptions: the MMSE approach requires ideal KCS,

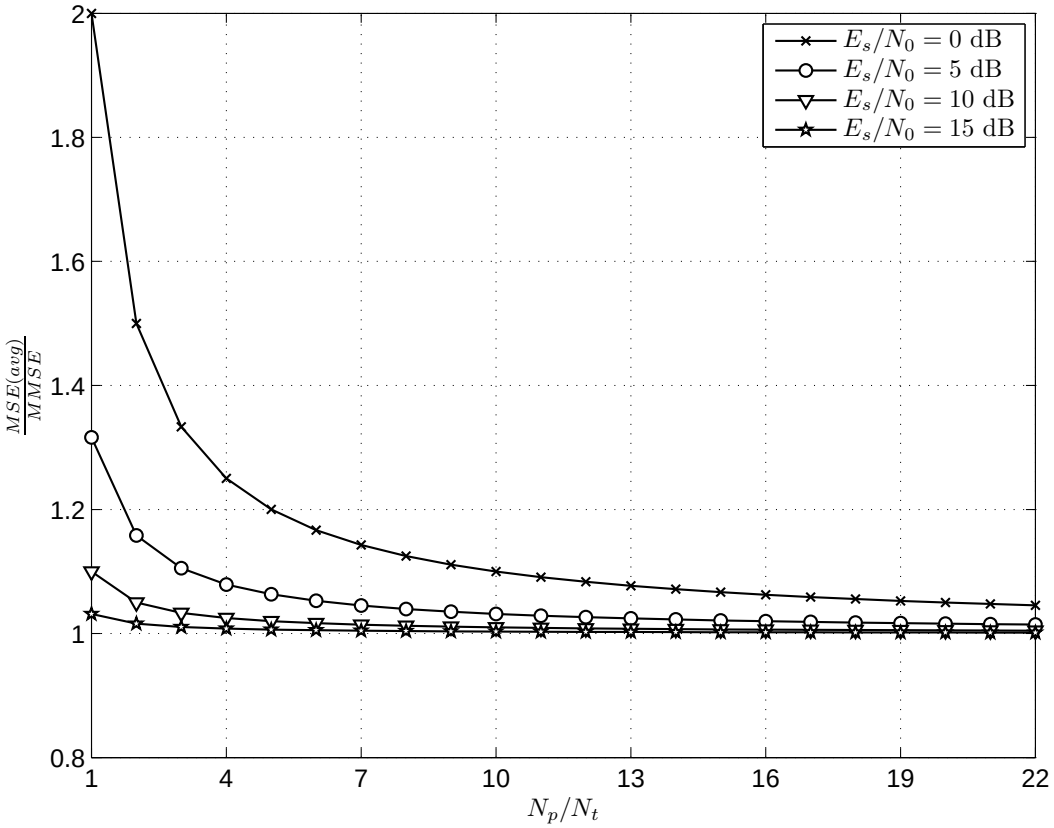

Figure 4.3: $\mathrm{MSE}(avg)$ normalized to the MMSE as a function of the ratio between number of pilots over number of taps, for several values of SNR. Using uniform channel and $\beta^2 = 1$.

while the instantaneous optimal selection requires the knowledge on the specific realizations of the channel response and thermal noise. This may lead to presume that $\mathrm{MSE}(opt)$ is lower than MMSE, on the other hand, the instantaneous optimal selection needs just a minimum information (a binary information) on the specific realizations, it is sufficient to know if $|h_{i,\ell}|$ is greater or smaller than $|\nu_{i,\ell}|$, while the MMSE approach requires full and ideal KCS.

However, since finding the exact $\mathcal{S}_{opt}(\ell)$ requires aid from a genie, we investigate also an alternative approach. The idea is to make decisions based on average rather than instantaneous quantities, the advantage being that estimation becomes possible. Assuming wide-sense stationarity, which eliminates the dependence on ℓ, we define the optimal set in the average sense, $\mathcal{S}_{avg}$, as:

$$\mathcal{S}_{avg} \equiv \left\{\text{all } i \text{ such that } E\left[|h_i|^2\right] > E\left[|\nu_i|^2\right] \ , \quad i = 0, \ldots, N_p - 1\right\} \tag{4.23}$$

The above is general and can be applied to any channel conditions. Specifying it for our channel model, it becomes

$$i \in \mathcal{S}_{avg} \Longleftrightarrow \gamma_i^2 > \frac{1}{\rho N_p} \tag{4.24}$$

Therefore, the $\mathrm{MSE}(avg)$, corresponding to the use of $\mathcal{S}_{avg}$ can be written as:

$$\mathrm{MSE}(avg) = \sum_{i \in \mathcal{C} \setminus \mathcal{S}_{avg}} E\left[|h_i|^2\right] + \sum_{i \in \mathcal{S}_{avg}} E\left[|\nu_i|^2\right] = \sum_{i \in \mathcal{C} \setminus \mathcal{S}_{avg}} \gamma_i^2 + \sum_{i \in \mathcal{S}_{avg}} \frac{1}{\rho N_p} \tag{4.25}$$

As a particular case, when ρN_p is large enough to ensure that $(\rho N_p)^{-1} < \gamma_i^2$, $\forall i \in \mathcal{C}$, then $\mathcal{S}_{avg} \equiv \mathcal{C}$, and it holds:

$$\mathrm{MSE}(avg) = \sum_{i \in \mathcal{C}} E\left[|\nu_i|^2\right] = \frac{N_t}{\rho N_p} \tag{4.26}$$

It is interesting to compare the $\mathrm{MSE}(avg)$ to LS provided in Eq. (4.6) and MMSE performance. We observe that, for $\mathcal{S}_{avg} \equiv \mathcal{C}$, $\mathrm{MSE}(avg)$ improves over $\mathrm{MSE}(LS)$ by a factor equal to $N_t/N_p < 1$. In practice, N_t is much smaller than N_p, yielding a much lower MSE value. Regarding MMSE estimation, as anticipated previously, under the assumption of uniformly scattered pilots the MMSE is given by:

$$\mathrm{MMSE} = \sum_{i \in \mathcal{C}} \frac{\gamma_i^2}{1 + \rho N_p \gamma_i^2} \tag{4.27}$$

Assuming a uniform power delay profile, where all the N_t taps have equal energy:

$$\gamma_i^2 = \begin{cases} \frac{1}{N_t} & i \in \mathcal{C} \\ 0 & i \notin \mathcal{C} \end{cases} \tag{4.28}$$

the MMSE becomes:

$$\mathrm{MMSE} = \frac{1}{1 + \frac{\rho N_p}{N_t}} = \frac{1}{1 + \frac{1}{\mathrm{MSE}(avg)}} \tag{4.29}$$

We observe that $\lim_{\frac{\rho N_p}{N_t} \to \infty} \mathrm{MMSE} = \mathrm{MSE}(avg)$, which confirms that *the average approach is asymptotically optimum*. In practice, $\mathrm{MSE}(avg)$ approaches MMSE performance rapidly. As an example, Fig. 4.3 shows the ratio between $\mathrm{MSE}(avg)$ and MMSE in the case of uniform power delay profile, for several values of SNR, and of the ratio between number of pilots over number of taps. In the end, *MMSE is the ultimate performance limit for both instantaneous and average strategies*.

4.4 Novel Algorithms

Our purpose is now to investigate selection strategies which can nearly achieve the MMSE performance without KCS. As anticipated in the Section 4.2, we deal with three different strategies: Threshold Crossing Selection (TCS), Instantaneous Energy Selection (IES), and Average Energy Selection (AES). TCS and IES, which decimate CIR samples without using memory from previous OFDM symbols, are oriented towards the use of $S_{opt}(\ell)$. On the other hand, AES, which decimates CIR samples by extending the observation window over several OFDM symbols, is oriented towards the use of S_{avg}.

4.4.1 Threshold Crossing Selection

The TCS strategy for identifying the MSS set, which has been treated in [70], [71], [72], [73], [74], is based on the concept that only those samples which overcome a threshold ξ in absolute value are retained:

$$\mathcal{S}_{\mathrm{TCS}}(\ell) \equiv \left\{ \text{all } i \text{ such that } |\hat{h}_{i,\ell}| > \xi \ , \quad i = 0, \ldots, N_p - 1 \right\} \tag{4.30}$$

In [71, eq. (21)] the threshold ξ has been empirically set equal to the square root of twice the noise level (which should be estimated):

$$\xi = \sqrt{\frac{2}{\rho N_p}} \tag{4.31}$$

In [72, eq. (6)], a criterion is proposed for establishing a set of threshold values that requires the knowledge of the entire CIR power profile:

$$\xi_i = \sqrt{\frac{1}{\rho N_p} \ln\left(2 + \rho N_p \gamma_i^2\right)} \qquad i = 0, \ldots, N_p - 1 \tag{4.32}$$

In [73] we proposed a pragmatic approach to set the threshold without KCS, based on a specification for the overall NH probability:

$$\xi = \sqrt{\frac{\ln\left(N_p / \overline{P^{\mathrm{ONH}}}\right)}{\rho N_p}} \tag{4.33}$$

where $\overline{P^{\mathrm{ONH}}}$ is a design parameter. In [74] the same threshold setting has been applied to OFDM time-frequency synchronization problems.

These methods are reasonable but based on heuristics. Here, we find the optimal threshold by deriving the closed form expression for the TCS MSE performance, and then by minimizing it with respect to ξ.

4.4.1.1 TCS MSE: Analytical Expression

Adopting TCS with a threshold ξ, and considering (4.12) and (4.30), we can write the PH probability in the i-th sample, as:

$$P_i^{\mathrm{PH}} = \mathrm{Prob}\left[|\hat{h}_i| > \xi \,\middle|\, i \in \mathcal{C}\right] = \mathrm{e}^{-\frac{\rho N_p \xi^2}{1+\gamma_i^2 \rho N_p}} \quad \forall\, i \in \mathcal{C} \tag{4.34}$$

Similarly, the NH probability is given by:

$$P_i^{\mathrm{NH}} = \mathrm{Prob}\left[|\hat{h}_i| > \xi \,\middle|\, i \notin \mathcal{C}\right] = \mathrm{e}^{-\rho N_p \xi^2} \quad \forall\, i \notin \mathcal{C} \tag{4.35}$$

Notably the NH probability does not depend on i, hence we will refer to it as P^{NH}. In summary, adopting TCS, the MSE can be found to be [73]:

$$\begin{aligned}
\mathrm{MSE}^{\mathrm{TCS}} &= \sum_{i=0}^{N_p-1} E\left[|\varepsilon_i|^2\right] = \\
&= \sum_{i\in\mathcal{C}} \left(P_i^{\mathrm{PH}} E\left[|\nu_i|^2|\mathrm{PH}\right] + P_i^{\mathrm{PE}} E\left[|h_i|^2|\mathrm{PE}\right] \right) + \sum_{i\notin\mathcal{C}} P^{\mathrm{NH}} E\left[|\nu_i|^2|\mathrm{NH}\right] = \\
&= \sum_{i\in\mathcal{C}} \left[\frac{\mathrm{e}^{-\frac{\rho N_p \xi^2}{1+\gamma_i^2\rho N_p}}}{\rho N_p} + \left(1 - e^{-\frac{\rho N_p \xi^2}{1+\gamma_i^2\rho N_p}}\right)\left(\gamma_i^2 - \frac{\xi^2}{e^{\xi^2/\gamma_i^2}-1}\right) \right] + \\
&\quad + \ (N_p - N_t)\frac{\mathrm{e}^{-\rho N_p \xi^2}\left(1+\rho N_p \xi^2\right)}{\rho N_p}
\end{aligned} \tag{4.36}$$

Our aim here is to derive analytically the optimal threshold ξ_{opt} which minimizes the MSE:

$$\xi_{opt} = \arg\min_{\xi} \mathrm{MSE}^{\mathrm{TCS}}(\xi) \tag{4.37}$$

A necessary condition is obtained by setting the first derivative of (4.36) to zero:

$$\begin{aligned}
\sum_{i\in\mathcal{C}} 2\xi \Bigg\{ & \frac{e^{-\frac{\rho N_p \xi^2}{1+\gamma_i^2\rho N_p}}}{1+\gamma_i^2\rho N_p} \left[\rho N_p \left(\gamma_i^2 - \frac{\xi^2}{e^{\frac{\xi^2}{\gamma_i^2}}-1} \right) - 1 \right] + \\
& + \frac{1 + e^{\frac{\xi^2}{\gamma_i^2}}\left(\frac{\xi^2}{\gamma_i^2}-1\right)}{\left(e^{\frac{\xi^2}{\gamma_i^2}}-1\right)^2} \left(1 - e^{-\frac{\rho N_p \xi^2}{1+\gamma_i^2\rho N_p}}\right) \Bigg\} + \\
& - 2\rho N_p \xi^3 \mathrm{e}^{-\rho N_p \xi^2}(N_p - N_t) = 0
\end{aligned} \tag{4.38}$$

Equation (4.38) is in an implicit form, and can only be solved numerically, with knowledge of the channel power profile γ_i^2, $i \in \mathcal{C}$, and pilot energy to noise ratio ρ. We therefore proceed as follows.

4.4.1.2 Sub-Optimal Threshold

In order to achieve an explicit solution, as well as to avoid the required KCS, let's introduce a few assumptions and approximations. First, we assume a uniform power profile as in (4.28), so that (4.38) becomes:

$$2N_t\xi \left\{ \frac{e^{-\frac{\rho N_t N_p \xi^2}{N_t+\rho N_p}} N_t}{N_t+\rho N_p} \left[\rho N_p \left(\frac{1}{N_t} - \frac{\xi^2}{\mathrm{e}^{N_t\xi^2}-1} \right) - 1 \right] + \right.$$
$$\left. + \frac{1+e^{N_t\xi^2}\left(N_t\xi^2-1\right)}{\left(e^{N_t\xi^2}-1\right)^2} \left(1 - \mathrm{e}^{-\frac{\rho N_t N_p \xi^2}{N_t+\rho N_p}} \right) \right\} +$$
$$- 2\rho N_p \xi^3 \mathrm{e}^{-\rho N_p \xi^2}(N_p - N_t) = 0 \quad (4.39)$$

Second, note that $N_t + \rho N_p \approx \rho N_p$, which is justified even in low SNR regions, since the number of pilots N_p is typically large enough to ensure that $\rho N_p >> N_t$. Using this approximation, after considerable algebra, we obtain:

$$\mathrm{e}^{(\rho N_p - N_t)\xi^2} = \frac{N_p - N_t}{\rho N_p \xi^2 - 1} \left(\frac{\rho N_p \xi}{N_t} \right)^2 \quad (4.40)$$

Finally, exploiting the fact that $\rho N_p \xi^2 >> 1$, we have

$$\frac{N_p - N_t}{\rho N_p \xi^2 - 1} \left(\frac{\rho N_p \xi}{N_t} \right)^2 \approx \frac{(N_p - N_t)\rho N_p}{N_t^2} \quad (4.41)$$

and we can find the following explicit solution for the sub-optimal threshold:

$$\xi_{so} = \sqrt{\frac{\ln\left(\frac{(N_p - \hat{N}_t)\rho N_p}{\hat{N}_t^2}\right)}{\rho N_p - \hat{N}_t}} \quad (4.42)$$

Where $\hat{N}_t$ is a algorithm parameter assuming the number of taps of the CIR. Of course, the best performance is obtained in case of $\hat{N}_t = N_t$, however, as shown in the numerical results, Sub-Optimal Threshold (SOT) approach appear to be very robust even in case of large mismatch between N_t and $\hat{N}_t$. Furthermore, the SOT values obtained using expression (4.42), and those obtained by solving numerically (4.39) are very close for all SNR values, and thus the approximations are justified and practically useful.

4.4.2 Energy-based MSS Selection Strategies

We now discuss two approaches based on received energy. The first, IES, presented in Section 4.4.2.1, pursues instantaneous decimation and therefore seeks to approach $S_{opt}(\ell)$. The second, AES, presented in Section 4.4.2.2, works with averages over a window of several OFDM symbols, and thus goes after S_{avg}. Neither of two methods require KCS, but only the estimation of the received SNR.

4.4.2.1 Instantaneous Energy Selection

The idea is to orderly select the strongest CIR estimate samples until the collected energy reaches the estimate of the total received useful power. The selection is performed in each OFDM symbol, independently. We identify this strategy as Instantaneous Energy Selection (IES). Firstly, we sort the vector of CIR estimate samples in descending order of absolute values:

$$|\hat{h}_{i(0),\ell}| \geq |\hat{h}_{i(1),\ell}| \geq \ldots \geq |\hat{h}_{i(j),\ell}| \geq \ldots \geq |\hat{h}_{i(N_p-1),\ell}| \tag{4.43}$$

where $i(j)$ is an indexing function introduced to represent the sorting function applied to the CIR estimates samples, in descending order. Then, we keep accumulating the MSS as long as the total energy remains below the target T:

$$\mathcal{S}_{\text{IES}}(\ell) \equiv \left\{ \text{all } i(j) \text{ such that } \sum_{v=0}^{j-1} |\hat{h}_{i(v),\ell}|^2 \leq T \ , \quad j = 0, \ldots, N_p - 1 \right\} \tag{4.44}$$

The target T corresponds to the estimate of the total received useful power:

$$T = \sum_{i=0}^{N_p-1} |\hat{h}_i|^2 - \sum_{i=0}^{N_p-1} E[|\nu_i|^2] = \sum_{i=0}^{N_p-1} |\hat{h}_i|^2 - \frac{1}{\rho} \tag{4.45}$$

4.4.2.2 Average Energy Selection

All selection strategies described so far, were pointing at finding $S_{opt}(\ell)$. Unfortunately, their instantaneous nature makes them vulnerable to noise sparks which are erroneously reckoned as channel paths. As an alternative, it may be more efficient to point at S_{avg} by extending the observation window over several OFDM symbols, which allows filtering. As a consequence, higher reliability of the MSS selection and therefore better estimation performance are expected, especially in low SNR conditions. In particular, we select as MSSs those samples whose CIR estimate sample energy, measured in an observation window of W OFDM symbols,

overcomes a threshold, ζ:

$$\mathcal{S}_{\mathrm{AES}}(\ell) \equiv \left\{ \text{all } i \text{ such that } \hat{E}_{i,\ell} > \zeta \ , \quad i = 0, \ldots, N_p - 1 \right\} \tag{4.46}$$

where:

$$\hat{E}_{i,\ell} = \frac{1}{W} \sum_{v=\ell-W+1}^{\ell} |\hat{h}_{i,v}|^2 \tag{4.47}$$

The observation window length, W, is an important parameter upon which estimation performance is strongly dependent. In the case of wide-sense stationary channels, the larger W the more accurate the energy estimation, but the larger is the latency and the required memory at the receiver. On the other hand, in the case of non-stationary channels, it is necessary to limit W in order to track time varying channel statistics.

We derive the noise and path holding probabilities. Since for $i \notin \mathcal{C}$ the samples $\hat{h}_{i,\ell}$ are mutually statistically independent complex Gaussian variables, with zero mean and variance $(2\rho N_p)^{-1}$ per branch, P^{NH} for AES with observation window length W and threshold ζ is given by:

$$P^{\mathrm{NH}} = \mathrm{Prob}\left[\hat{E}_{i,\ell} > \zeta \middle| \, i \notin \mathcal{C} \right] = \mathrm{e}^{-W\rho N_p \zeta} \sum_{v=0}^{W-1} \frac{(W\rho N_p \zeta)^v}{v!} \qquad \forall i \notin \mathcal{C} \tag{4.48}$$

The analytical derivation is provided in Section 4.4.2.2.

On the other hand, considering the case $i \in \mathcal{C}$, the samples $\hat{h}_{i,\ell}$ are statistically correlated from symbol to symbol. In particular, the time correlation depends on the ratio between the channel coherence time, which depends on the terminal speed, and the OFDM symbol duration. In the following, we analyze two extreme cases, considering a very rapid and very slow channel respectively. In the first case, we assume that the Doppler spread is large enough to break the time correlation of the CIR estimate samples, belonging to different received OFDM symbols[2]. The $\hat{h}_{i,\ell}$ samples result to be again mutually statistically independent complex Gaussian variables, with zero mean and branch variance $\gamma_i^2/2 + (2\rho N_p)^{-1}$. Consequently, the PH probability is given by:

$$P_i^{\mathrm{PH}} = \mathrm{Prob}\left[\hat{E}_{i,\ell} > \zeta \, \middle| \, i \in \mathcal{C} \right] = \mathrm{e}^{-\frac{W\rho N_p \zeta}{1+\gamma_i^2 \rho N_p}} \sum_{v=0}^{W-1} \frac{1}{v!} \left(\frac{W\rho N_p \zeta}{1+\gamma_i^2 \rho N_p} \right)^v \ \forall\, i \in \mathcal{C} \tag{4.49}$$

In the second case, we assume that the Doppler spread is small enough to guarantee a quasi-static channel within the observation window length; therefore, the CIR

[2]Since we assumed that $h_j(t)$ is constant over a single OFDM symbol, this corresponds to a block fading channel model.

sample estimates, $\hat{h}_{i,\ell}$, can be seen as the sum of a static channel complex coefficient $h_{i,\ell} = \tilde{h}_i$, and noise. The $\hat{h}_{i,\ell}$ are again mutually statistically independent complex Gaussian variables (because noise is white), with mean $\tilde{h}_i$ and variance per branch $(\rho N_p)^{-1}$. In this case, $\hat{E}_i$ is distributed as a non-central chi-square distribution with non-centrality parameter $\lambda_i = |\tilde{h}_i|^2$. The corresponding PH probability is given by:

$$P_i^{\mathrm{PH}} = \mathrm{Prob}\left[\hat{E}_{i,\ell} > \zeta\right] = 1 - \frac{(\rho N_p)^W}{\gamma_i^2 \Gamma(W)} \int_0^{\zeta} \int_0^{\infty} x^{W-1} \mathrm{e}^{-(\lambda_i \gamma_i^2 + \rho N_p (x + W\lambda_i))} {}_0F_1\left(W; (\rho N_p)^2 W \lambda_i x\right) \, d\lambda_i \, dx \quad (4.50)$$

The analytical derivation is provided in Section 4.4.2.2. Similarly to the TCS case, the appropriate ζ setting depends on channel statistics, as well as on W. Since the analytical derivation of the optimal threshold ζ in this case is unfeasible, due to the fact that several integral forms are involved, we propose an alternative strategy which, as we show in the following, achieves performance very close to the $\mathrm{MSE}(avg)$ lower bound. Assuming that W is large enough to eliminate noise holding events, we can set the threshold ζ according to the definition $\mathcal{S}_{avg}$, here rewritten in terms of E_i:

$$i \in \mathcal{S}_{avg} \Longleftrightarrow E_i > \frac{2}{N_p \rho} = \zeta \quad (4.51)$$

Substituting (4.51) into (4.48), we obtain a very simple and intuitive expression:

$$P^{\mathrm{NH}} = \mathrm{e}^{-2W} \sum_{v=0}^{W-1} \frac{(2W)^v}{v!} \quad (4.52)$$

It is interesting to note that, in this case, the noise holding probability depends only on the observation window length. The performance of this method is very good for large W, as can be expected, while it reduces to TCS for $W = 1$, in which case other threshold setting strategies are more appropriate.

Path and Noise Holding Probabilities Let's consider the vector $\mathbf{h}_i = \{h_{i,\ell-W+1}, h_{i,\ell-W+2}, \ldots, h_{i,\ell}\}$ containing the W complex Gaussian random variables representing the complex path gains at the ℓ-th OFDM symbol for a given delay i. According to the Rayleigh fading assumption, vector $\mathbf{h}_i$ can be modelled as a W-variate zero mean complex Gaussian variable with covariance matrix Σ, i.e. $\mathbf{h}_i \sim \mathcal{N}_{cW}(0, \Sigma)$. The measured CIR sample energy $\hat{E}_{i,\ell}$ reported in (4.47), conditioned on $\mathbf{h}_i$, can be modelled as a non-central chi-square distribution, $\chi^2_{2W}(\lambda)$,

with $2W$ degrees of freedom, non-centrality parameter $\lambda = \frac{1}{W}\sum_{v=\ell-W+1}^{\ell}|h_{i,v}|^2$, and $\sigma^2 = (2\rho N_p W)^{-1}$,

$$p_{\hat{E}_{i,\ell}|\mathbf{h}_i}(x|\mathbf{h}_i) = \frac{x^{W-1}}{(2\sigma^2)^W\Gamma(W)}\mathrm{e}^{-\frac{x+\lambda}{2\sigma^2}}{}_0F_1\left(W;\frac{\lambda x}{(2\sigma^2)^2}\right) \tag{4.53}$$

where $\Gamma(W) = (W-1)!$ and ${}_0F_1(b;z)$ is a particular case of the generalized hypergeometric function ${}_mF_n(a_1,\dots a_m;b_1,\dots b_n;z)$ [39]. We start from the non-central chi-square definition based on the hypergeometric function in order to treat in the following the central chi-square as a particular case of non-central case [75, Appendix I].

Noise Holding Case: $i \notin \mathcal{C}$ Let's consider the case where $i \notin \mathcal{C}$. In this case $\mathbf{h}_i = \bar{0}$ with probability 1, and consequently $\lambda = 0$. Therefore, $\hat{E}_{i,\ell}$ can be modelled as a central chi-square random variable $\chi^2_{2W}(0)$ with $\sigma^2 = (2\rho N_p W)^{-1}$:

$$p_{\hat{E}_{i,\ell}}(x) = \frac{x^{W-1}(\rho N_p W)^W}{\Gamma(W)}\mathrm{e}^{-x\rho N_p W} \qquad \forall i \notin \mathcal{C} \tag{4.54}$$

Thus P^{NH} is given by:

$$P^{\mathrm{NH}} = \mathrm{Prob}\left[\hat{E}_{i,\ell} > \zeta \,\middle|\, i \notin \mathcal{C}\right] = \mathrm{e}^{-W\rho N_p\zeta}\sum_{v=0}^{W-1}\frac{(W\rho N_p\zeta)^v}{v!} \qquad \forall i \notin \mathcal{C} \tag{4.55}$$

Setting ζ according to (4.51), it follows:

$$P^{\mathrm{NH}} = \mathrm{e}^{-2W}\sum_{v=0}^{W-1}\frac{(2W)^v}{v!} \qquad \forall i \notin \mathcal{C} \tag{4.56}$$

Path Holding with Uncorrelated Fading: $i \in \mathcal{C}$ **and** $\Sigma = Diag(\gamma_i^2)$ Let's consider the particular case where $i \in \mathcal{C}$, and the elements of $\mathbf{h}_i$ are zero-mean complex Gaussian variables i.i.d. with variance γ_i^2 (i.e. the covariance matrix Σ is diagonal). In this case $\hat{E}_{i,\ell}$ can be modelled as a central chi-square random variable $\chi^2_{2W}(0)$ with $\sigma^2 = (\gamma_i^2/2 + 1/(2\rho N_p))/W$. Therefore, similarly to the previous case, P_i^{PH} is given by:

$$P_i^{\mathrm{PH}} = \mathrm{Prob}\left[\hat{E}_{i,\ell} > \zeta \,\middle|\, i \in \mathcal{C}\right] = \mathrm{e}^{-\frac{W\rho N_p\zeta}{1+\gamma_i^2\rho N_p}}\sum_{v=0}^{W-1}\frac{1}{v!}\left(\frac{W\rho N_p\zeta}{1+\gamma_i^2\rho N_p}\right)^v \quad \forall\, i \in \mathcal{C} \tag{4.57}$$

Path Holding with Perfectly Correlated Fading: $i \in \mathcal{C}$ **and** $\mathbf{h}_i = \tilde{h}_i$ Let's consider the particular case where $i \in \mathcal{C}$, and all the elements of $\mathbf{h}_i$ are equal to $\tilde{h}_i$. In this case, $\hat{E}_{i,\ell}$ can be modelled as a non-central $\chi^2_{2W}(\lambda_i)$, with non-centrality parameter $\lambda_i = |\tilde{h}_i|^2$, and $\sigma^2 = (2\rho N_p W)^{-1}$:

$$p_{\hat{E}_{i,\ell}}(x|\lambda_i) = \frac{x^{W-1}(\rho N_p W)^W}{\Gamma(W)} \mathrm{e}^{-\rho N_p W^2 (x+\lambda_i)} {}_0F_1\left(W; (\rho N_p W)^2 \lambda_i x\right) \tag{4.58}$$

The non-centrality parameter λ_i is itself distributed as a $\chi^2_2(0)$ with branch variance equal to $\gamma_i^2/2$. After removing the conditioning on λ_i the holding path probability is given by:

$$P_i^{\mathrm{PH}} = \frac{2(\rho N_p W)^W}{\gamma_i^2 \Gamma(W)} \int_\zeta^\infty \int_0^\infty \lambda_i x^{W-1} \mathrm{e}^{-(\lambda_i/\gamma_i^2 + \rho N_p W(x+\lambda_i))} \\ {}_0F_1\left(W; (\rho N_p W)^2 \lambda_i x\right)\, d\lambda_i\, dx \qquad \forall\, i \in \mathcal{C} \tag{4.59}$$

4.5 Numerical Results and Discussions

The purpose of this Section is twofold: first, we assess pure channel estimation performance in terms of MSE and validate our analytical models; second, we evaluate the impact of using the proposed channel estimators in terms of BER at the output of the channel decoder. In order to have practically significant results, we consider the standardized coded OFDM system, DVB-SH [20]. DVB-SH foresees the 3GPP2 turbo code and a convolutional interleaver. In order to set the system dynamics, we assume that the DVB-SH system is operating in S-band (2 GHz) with 5 MHz of bandwidth, and the terminal speed is 50 km/h. We used Monte Carlo simulations to evaluate both MSE and BER. Two different channel models are used: a 6-taps uniform channel and the ITU-TU6 channel, the power delay profiles of which are reported in Table 4.1. As outlined in Section 1.5, in the analysis we have assumed a uniformly scattered pilot pattern over the entire frequency comb, which, as shown in [76], is the best pilot arrangement in terms of channel estimation MMSE. However, DVB-SH, as well as other standards, does not provide a perfectly uniform scattered pilot pattern because of the insertion of guardbands. In fact this standard uses $N = 1024$ carriers, with $N_p = 71$ scattered pilots distributed over the first $N_a = 852$ active subcarriers. As a consequence, the resulting pilot pattern is not optimal in terms of MSE, and the CIR samples become correlated [69]. To the end of assessing the impact on the performance of our proposed algorithms we also report simulation results in the presence of CIR correlation.

Table 4.1: Normalized power delay profile of the considered multipath channels

	Taps	#1	#2	#3	#4	#5	#6
Uniform	Delay[μs]	0.0	1.05	2.1	3.15	4.2	5.25
Channel	Power[dB]	-7.78	-7.78	-7.78	-7.78	-7.78	-7.78
ITU	Delay[μs]	0.0	0.2	0.5	1.6	2.3	5.0
TU6	Power[dB]	-7.22	-4.22	-6.22	-10.22	-12.22	-14.22

4.5.1 MSE performance

Our intent here is first to validate our analytical models through numerical results obtained by simulation and second to assess the performance and robustness of the proposed MSS algorithms against channels with different power delay profiles, and non-uniform pilot pattern.

In Fig. 4.4, we report the results for the proposed TCS algorithms (with optimal and sub-optimal thresholds) and for the state-of-art alternatives over the uniform channel using a uniformly scattered pilot patterns. We observe that the $\mathrm{MSE}^{\mathrm{TCS}}$ computed with (4.36) and the appropriate threshold value, is in perfect agreement with the numerical performance of all TCS algorithms. Comparing TCS methods, SOT reaches the best results among the practical algorithms, and is also very close to the optimum threshold results. At MSE $= 10^{-2}$ the gain is larger than 10 dB and 6 dB with respect to the LS and TCS [71] methods, respectively. Even the criterion proposed in [72], which takes advantage of the KCS, is outperformed by SOT. Moreover, SOT is also close to MMSE at high SNR.

Clearly the uniform channel is the best match for our SOT strategy. Therefore, it is important to verify the performance in non-uniform channels. In Fig. 4.5, the numerical results using both uniform and ITU-TU6 channels are illustrated. It is important to note that the SOT performance for the ITU-TU6 channel is only slightly worse than the a uniform channel case. Furthermore, comparing TCS methods, SOT has the best performance for both considered channels, and for high SNR it approaches MMSE.

In Fig. 4.6, we report the comparison between SOT and the MSS-J selection strategy proposed in [70] using the ITU-TU6 channel and uniform pilot pattern. Since both methods require the knowledge of the number of the channel taps, N_t, we tested the robustness to a mismatch on this parameter. Even in the case of no mismatch, SOT outperforms MSS-J. When J differs from N_t, MSS-J performance

degrades rapidly. On the other hand, SOT has good performance even in the case of a large mismatch. Furthermore, in Fig. 4.6, we also report the comparison between SOT and TCS proposed in [73] considering two indicated values of the parameter P^{ONH}. SOT outperforms TCS proposed in [73], even in the case of a mismatch.

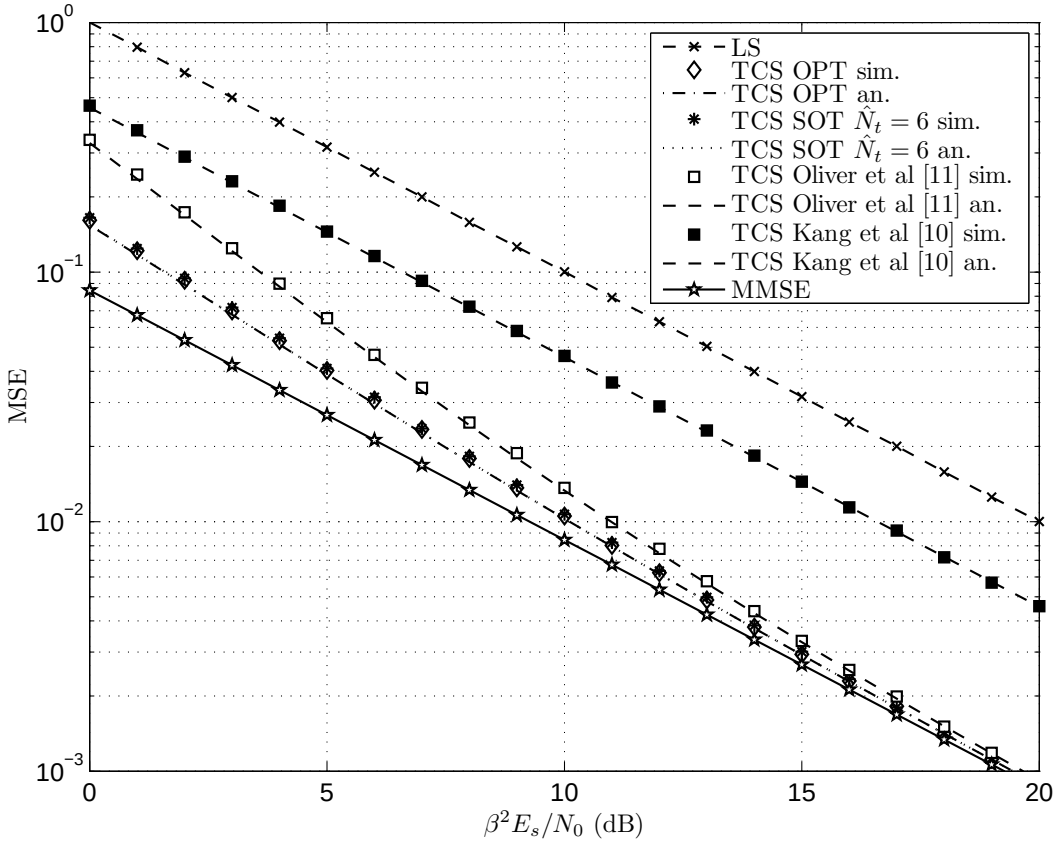

Figure 4.4: Comparison between analytical, obtained from eq. (4.36), and simulated performance of several TCS selection strategies with uniform channel with $N_t = 6$.

Fig. 4.7 shows the numerical results considering the ITU-TU6 channel, for the proposed IES and AES strategies. Regarding the AES method, the threshold ζ has been set according to (4.51). Numerical results show that, by using an observation window equal or greater than 10 OFDM symbols ($W \geq 10$), AES approaches very closely MMSE outperforming all other considered methods (not reported in this Figure). Even in the case of $W = 5$, AES outperforms the other selection strategies in the low SNR region. Using smaller W, AES performance degrades.

As discussed before, it is necessary to verify the estimation performance of the

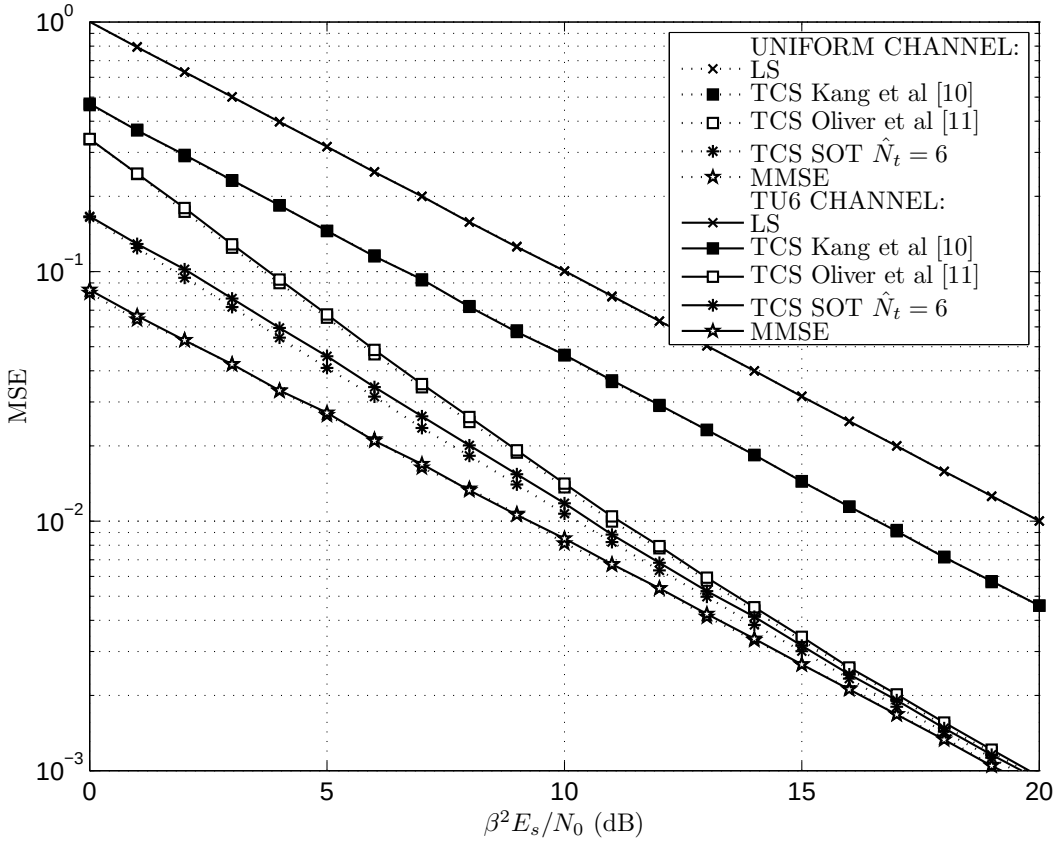

Figure 4.5: Comparison between the performance of several threshold based MSS selection strategies with TU6 and uniform channel.

proposed algorithms when the condition of uncorrelated CIR samples is violated. In Figs. 4.8 and 4.9, we compare the proposed schemes (SOT, IES and AES) with the state-of-art alternatives using both uniform and non-uniform pilot patterns (as standardized by DVB-SH), with the same number of pilots, $N_p = 71$. As a consequence of correlation among CIR estimates, MSE performance deteriorates with respect to uniform pilot pattern case. Nevertheless, the proposed SOT and AES with $W \geq 10$ are still the best solutions among the practical channel estimation methods.

Summarizing, numerical results show that AES with $W \geq 10$ outperforms all other methods, especially in the low SNR region, closely approaching MMSE. This holds true even when the condition of uncorrelated CIR estimated samples is not verified, due to non-uniform pilot pattern. On the other hand, SOT is a strong

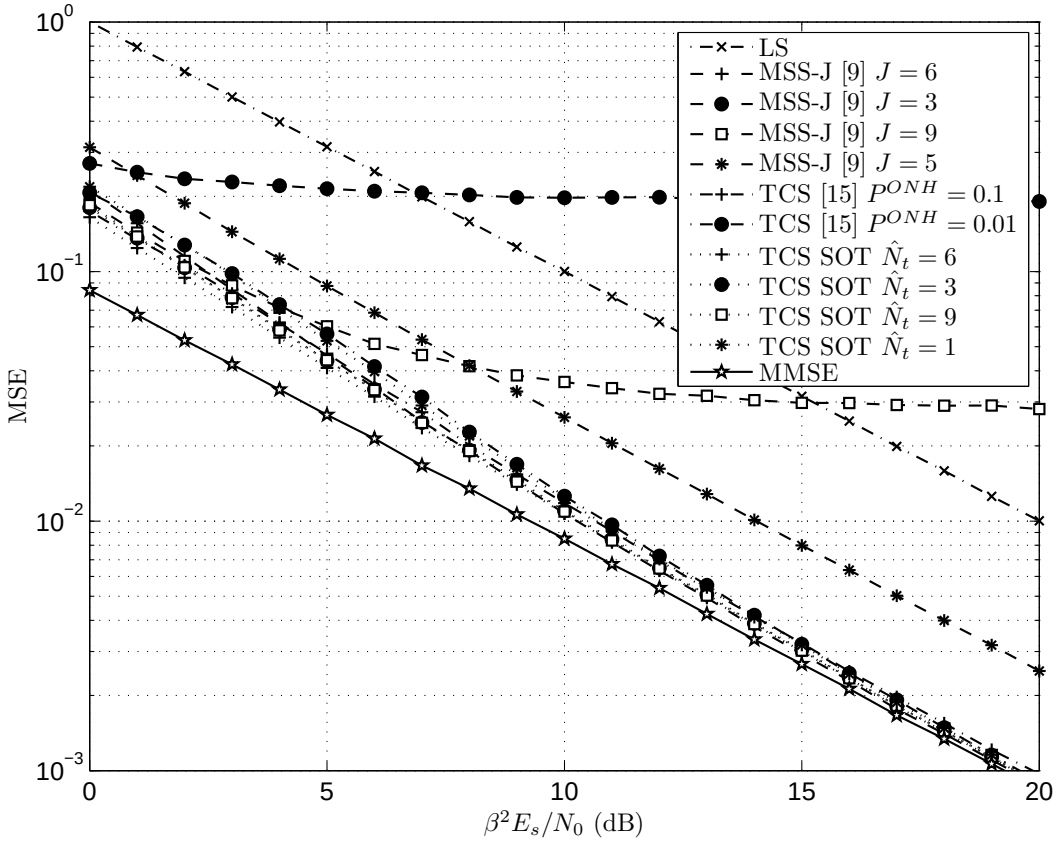

Figure 4.6: Comparison between TCS with Sub-Optimal threshold, TCS [73], and the method proposed in [70] using TU6 channel ($N_t = 6$). Different mismatch levels between the actual and the assumed number of taps.

alternative, especially in the high SNR region, considering its lower latency. Concerning the IES strategy, numerical results show that this method achieves good performance, even if it is outperformed by SOT and AES.

4.5.2 BER performance

Here we consider the impact of using different channel estimation methods on the DVB-SH BER. In Figs. 4.10 and 4.11, we report BER for QPSK modulation and turbo code rate 1/4 and 1/2 respectively, and in Fig. 4.12 we report BER for 16QAM modulation and turbo code rate 1/2. we consider TU6 channel and with terminal speed equal to 50 km/h. In order to make a complete comparison we present the results for both uniform and non-uniform pilot patterns. In the uniform pilot pattern

case, the numerical results confirm the trend observed in MSE performance assessments: BER using AES is very close to the case of using MMSE channel estimation for all the considered modulations and coding rates. Using SOT for QPSK and coding rate $1/4$, we observe performance gaps of 0.5 dB with respect to MMSE, and 1 dB with respect to ideal channel estimation. These gaps become smaller when using QPSK and 16QAM with coding rate $1/2$. In particular, considering 16QAM, both AES and SOT methods converge to the MMSE case, and are close to ideal channel estimation performance.

In the non-uniform pilot pattern case, a BER increase can be observed performance decreases because of the correlation between CIR estimates samples. In particular, with respect to Wiener Filtering case at $\mathrm{BER} = 10^{-3}$ we observe performance gaps of: 0.3 dB for AES, and 1 dB for SOT, using QPSK and coding rate $1/4$; 0.9 dB for AES, and 1.4 dB for SOT, using QPSK and coding rate $1/2$; and finally, 2 dB for AES, and of 2.4 dB for SOT, using 16QAM and coding rate $1/2$.

Summarizing, comparing the ideal and real channel estimation cases, using a uniform pilot pattern, the performance loss due to the estimation error is smaller for higher modulation order and coding rate. In fact, in this case, the SNR working point is higher, thus the channel estimation MSE lowers. On the other hand, using a non-uniform pilot pattern, the performance loss is greater for higher modulation order and coding rate. In fact, in this case, the required channel estimation quality is higher but as a consequence of the MSE error floor due to the CIR estimates correlation, channel estimation MSE is bounded.

In conclusion, numerical results confirm that the proposed algorithms based on MSS selection of CIR estimate guarantee a significant gain even in those practical cases where correlation among CIR estimate samples occurs. Moreover, using lower modulation order and coding rate, the proposed algorithms approach the MMSE case in terms of BER performance.

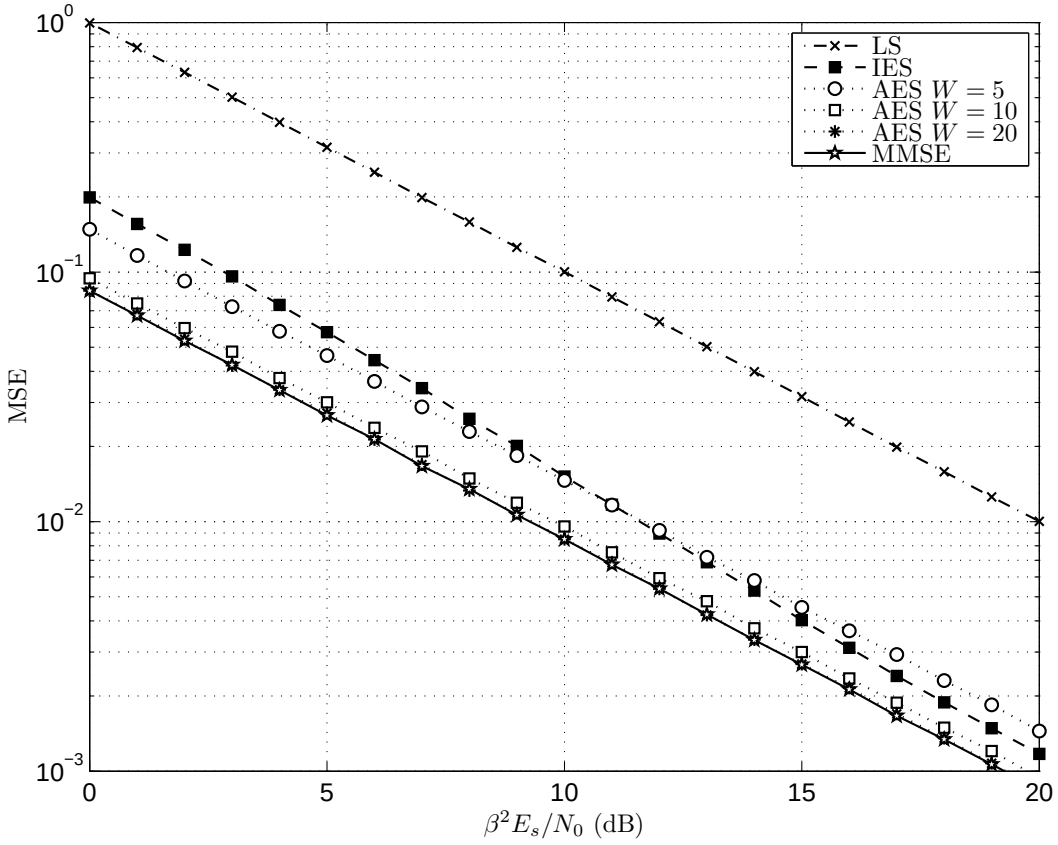

Figure 4.7: Comparison between the proposed MMS selection strategies based on energy estimation, using TU6, 50 km/h.

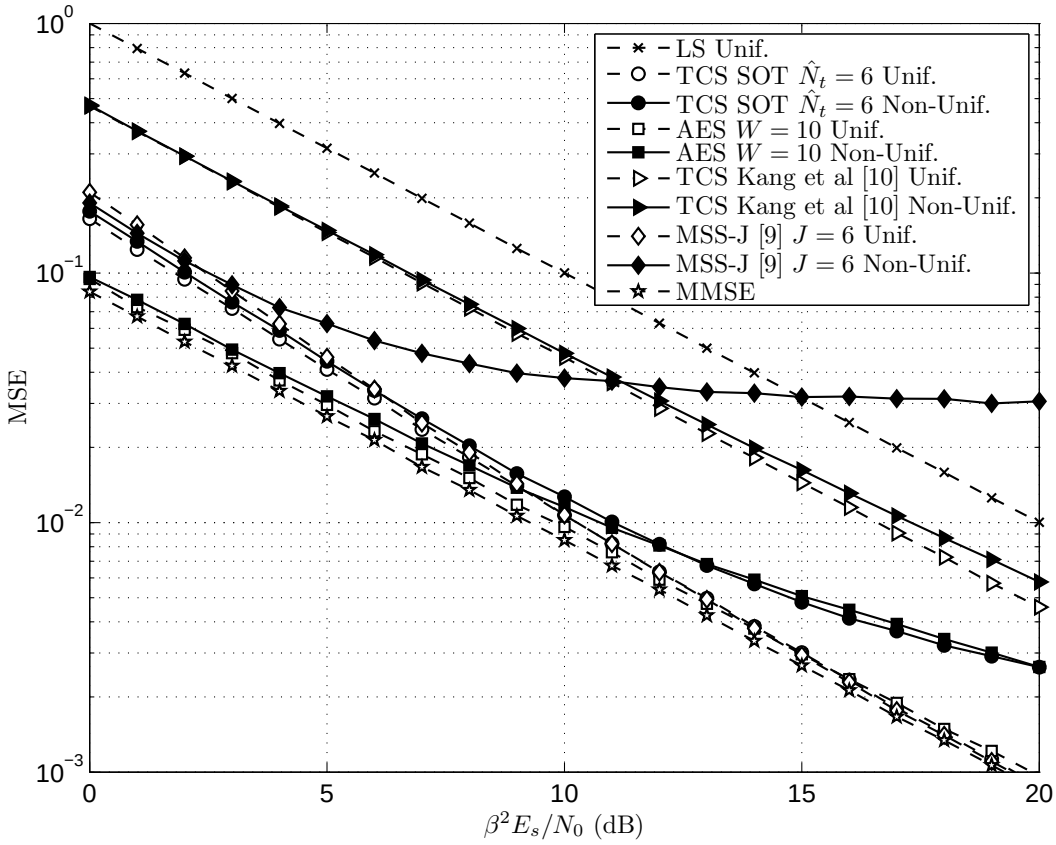

Figure 4.8: Channel estimation performance of the proposed algorithms, SOT and AES with $W = 10$, compared with the state-of-art alternatives, considering both the cases of uniform and non-uniform pilot pattern with the same number of pilots, $N_p = 71$.

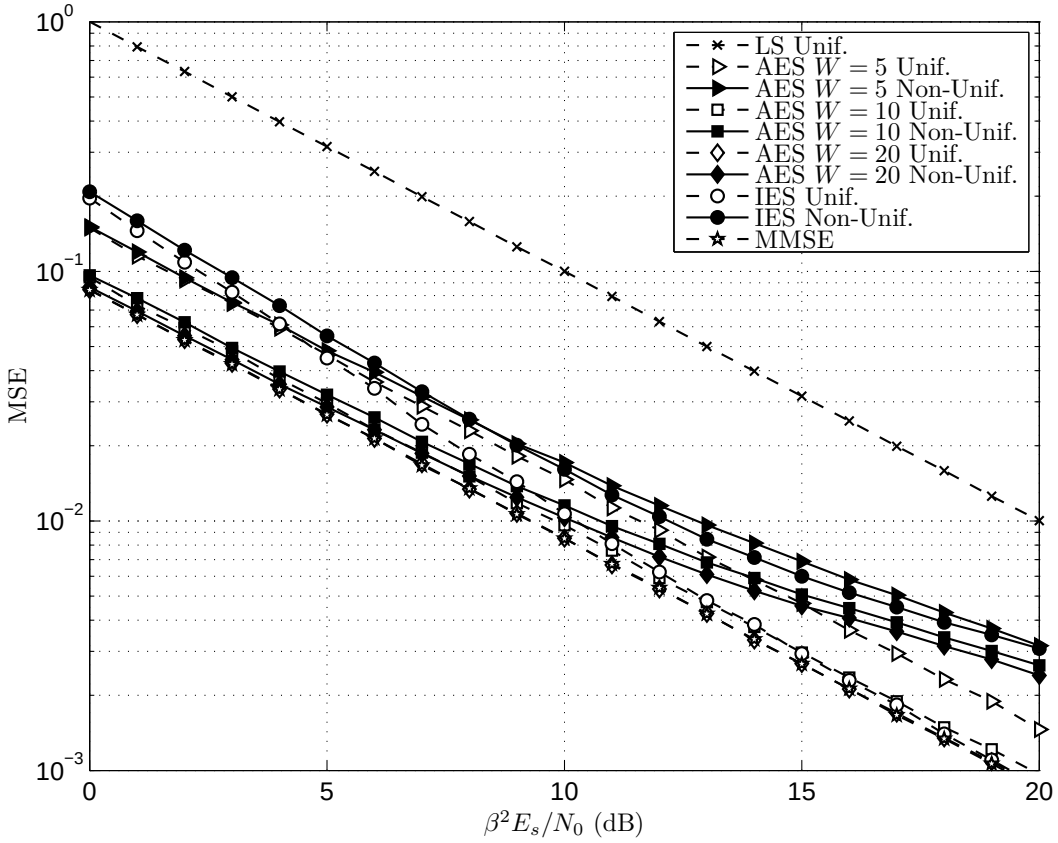

Figure 4.9: Channel estimation performance of the proposed algorithms, IES and AES with several values of W, considering both the cases of uniform and non-uniform pilot pattern with the same number of pilots, $N_p = 71$.

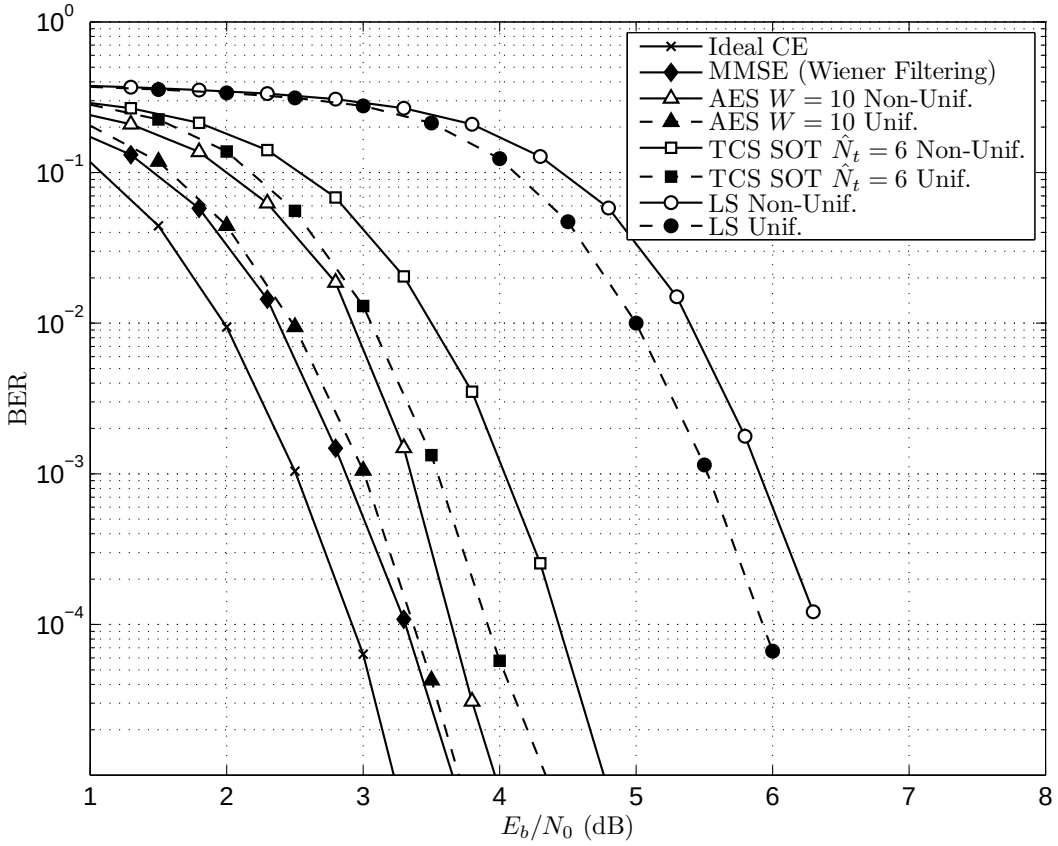

Figure 4.10: Coded DVB-SH BER performance, QPSK,turbo code rate 1/4, considering both the cases of uniform and non-uniform pilot pattern with the same number of pilots, TU6, 50 km/h.

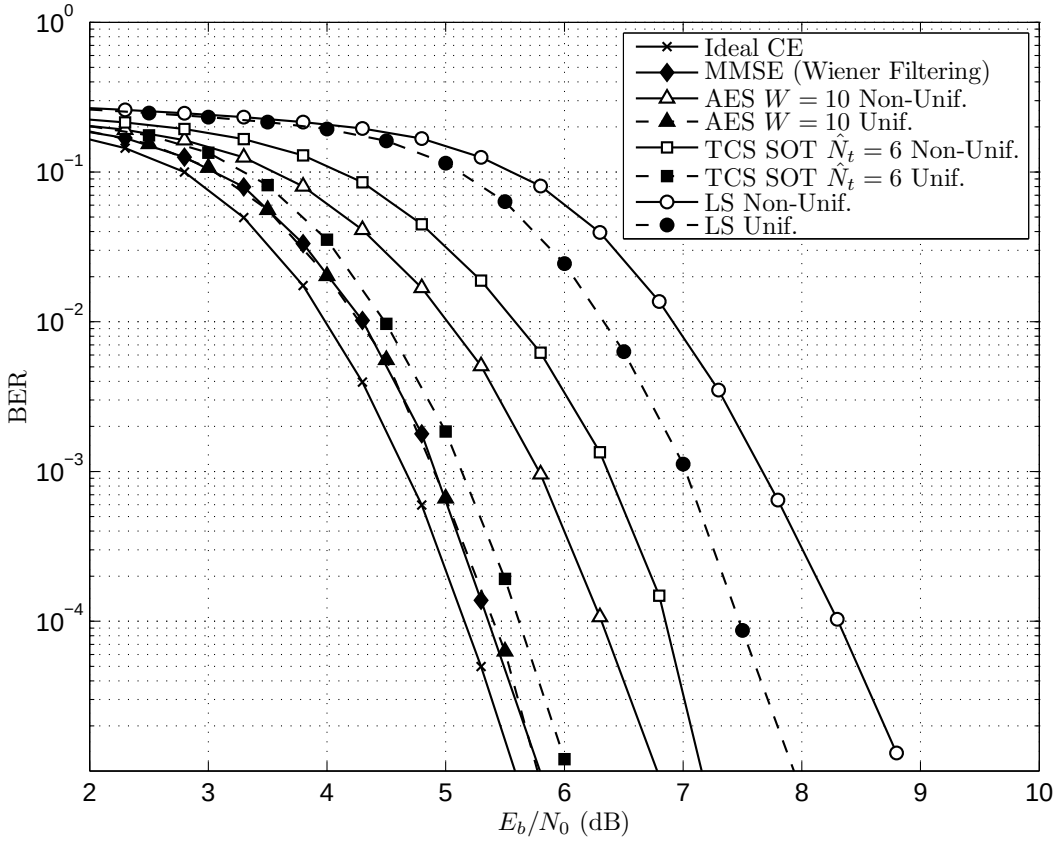

Figure 4.11: Coded DVB-SH BER performance, QPSK,turbo code rate 1/2, considering both the cases of uniform and non-uniform pilot pattern with the same number of pilots, using TU6 , 50 km/h.

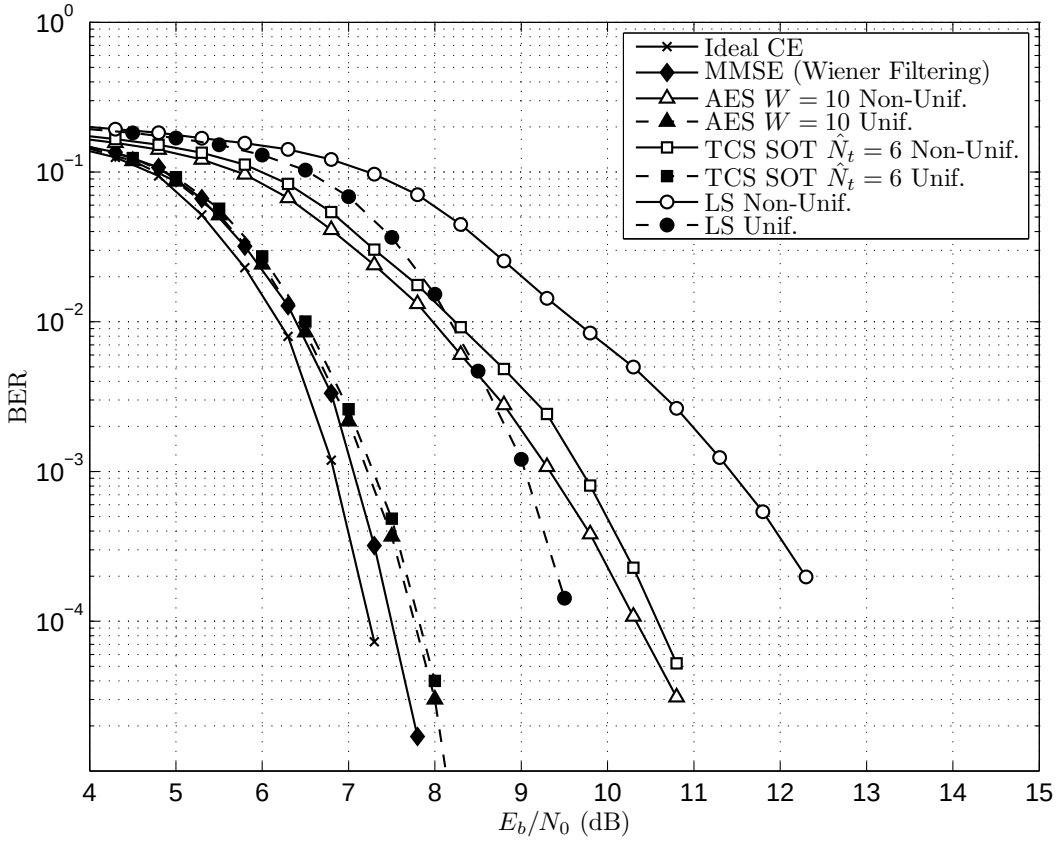

Figure 4.12: Coded DVB-SH BER performance, 16QAM, turbo code rate 1/2, considering both the cases of uniform and non-uniform pilot pattern with the same number of pilots, using TU6, 50 km/h.

Chapter 5

SC-FDMA in Broadband Satellite Return Channel: Joint Multi-User Synchronization

A connecting principle linked to the invisible
almost imperceptible something inexpressible
science insusceptible logic so inflexible
causally connectible nothing is invincible

Synchronicity I, The Police

In this Chapter we asses the use of Single Carrier Frequency Division Multiple Access (SC-FDMA) in the Broadband Satellite Return Channel, with particular reference to the DVB Return Channel via Satellite (DVB-RCS) Standard [22]. In Section 5.1 we describe the return channel via satellite and the possibility to use a orthogonal multicarriers solution instead of the single carrier solutions, which are typically employed in this scenario. Then in Section 5.1.1, we provide a detailed SC-FDMA system model tailored to the addressed scenario. Since, SC-FDMA requires a strict synchronization, in Section 5.2.1, we present an appropriate pilot pattern design, and, in Sections 5.2.2 and 5.2.3, we present a novel joint Multi-User Estimation method which, by exploiting the inserted pilot tones, aims to jointly estimate both the CPE and the inter-arrival timing offset for each user. Finally in Section 5.3, we report the numerical results

showing that the proposed algorithm is able to guarantee the proper demodulation of the received signal.

5.1 SC-FDMA in Return Satellite Channel

DVB-RCS is the specification for an interactive on-demand multimedia satellite communication system [22]. In November 2008, a Call-for-Technology to improve the DVB-RCS standard has been opened. This Call-for-Technology was aimed at providing competitive enhancements to DVB-RCS in order to expand its current market and to follow emerging technology trends, such as mobile and mesh networks. In particular, the low cost of the user equipment and efficient bandwidth management have been identified as crucial targets.

According to these requirements we have assessed the possibility to use SC-FDMA in the Broadband Satellite Return Channel Scenario. The main results of this work are reported in [23]. Even if the SC-FDMA solution has not been included in the baseline version of the DVB-RCS Next Generation (NG), approved in December 2010, at the time of writing, it is still considered for the mesh, and the mobile versions of the standard.

In brief, the main advantage of the SC-FDMA over the single carrier systems, which has been used so far in the standard, is its higher physical layer spectral efficiency. However, it is particularly sensitive to phase noise and timing offset, thus it requires an enhanced synchronization scheme. In the RCS scenario any terminal user which intents to transmit in the satellite return link, shall be already fully synchronized with the satellite forward link. For this reason, the residual frequency and timing offsets can be considered negligible. However, due to different geographical locations of the user terminals, the signals transmitted by each terminal will reach the satellite component with a different delay. Therefore, in case of SC-FDMA, the signal from different users should arrive within the CP duration in order to maintain the orthogonality between subcarriers. Clearly, a larger CP reduces the network synchronization requirements at the expense of the spectral efficiency. Furthermore, in order to obtain realistic results we must also take into account the effect introduced by the phase noise on the received signal.

5.1.1 SC-FDMA System Model

SC-FDMA is an effecting multicarrier technique for high data rate wireless communication especially for uplink communication. In fact, recently, SC-FDMA has been chosen by the 3GPP forum as uplink multiple access scheme in the 4G cellular system: LTE [77]. This is because SC-FDMA not only provides a very efficient bandwidth usage which yields a similar throughput compared with OFDMA access scheme, but also it is able to guarantee a lower PAPR which allows the use of more efficient and thus more distorting HPA. As illustrated in Figures 5.1 and 5.2, SC-FDMA can been seen as modified form of OFDMA, where each user, firstly transform its time domain data symbols to the frequency domain; then, the complex results are mapped on the assigned subcarriers and transformed again in time domain by IFFT operation.

In this Section we introduce a generic SC-FDMA system model which accurately suits the addressed scenario. In particular the inter-arrival delay and the phase noise are taken into account, while carrier frequency offset is neglected because the user terminal is already fully synchronized with the satellite forward link. Let us consider a SC-FDMA signal with N total subcarrier where M subcarriers are assigned to each user, and $U = N/M$ is the maximum number of users. As depicted in Figures 5.1, the ℓ-th SC-FDMA frequency domain symbol belonging to the u-th user, $\bar{x}_{\ell,u} = (x_{0,\ell,u}, \ldots, x_{M-1,\ell,u})$, is obtained as the M-points DFT of the vector of complex data symbols $\bar{a}_{\ell,u} = (a_{0,\ell,u}, \ldots, a_{M-1,\ell,u})$, as:

$$x_{k',\ell,u} = \frac{1}{\sqrt{M}} \sum_{m=0}^{M-1} a_{m,\ell} \mathrm{e}^{-\jmath 2\pi m k'/M} \qquad k' = 0, \ldots, M-1 \tag{5.1}$$

After having performed the subcarrier mapping operation, which aims to allocate subcarriers among users, the corresponding time domain symbol, $\bar{s}_{\ell,u} = (s_{0,\ell,u}, \ldots, s_{N-1,\ell,u})$, is computed by apply the N points IDFT:

$$s_{i,\ell,u} = \frac{1}{\sqrt{N}} \sum_{k'=0}^{M-1} x_{k',\ell} \mathrm{e}^{\jmath 2\pi m \frac{k(k')}{N}} \quad i = 0, \ldots, N-1 \tag{5.2}$$

where $k(k')$ is an indexing function introduced to point out the subcarrier mapping function. Two possible approaches to allocate subcarriers among terminals have been addressed in literature [78]: Localized SC-FDMA, where each user occupies a set of adjacent subcarriers; and the Interleaved SC-FDMA, where each user occupies a set of equidistant subcarriers. In the following, we will refer to the localized approach.

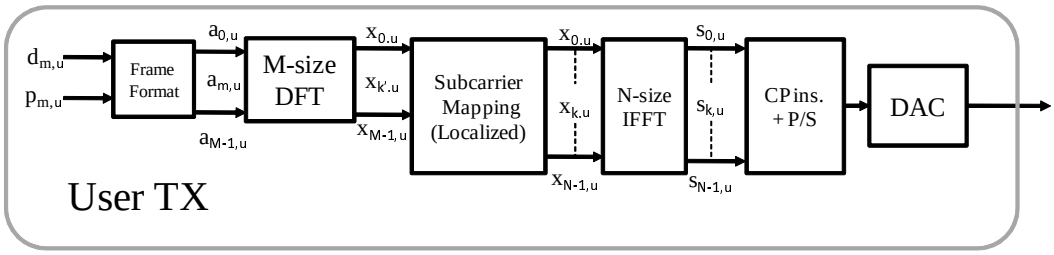

Figure 5.1: Block diagram of the SC-FDMA transmitter

Before performing Digital to Analog Conversion (DAC) at sampling rate $R = 1/T$, the CP of length N_g samples is inserted at the beginning of each symbol, in order to avoid intersymbol interference and maintain subcarrier orthogonality. Therefore, the time continuous signal transmitted by the u-th user can be written as

$$s_u(t) = \frac{1}{\sqrt{T_u}} \sum_{\ell=-\infty}^{\infty} \sum_{k=0}^{M-1} \text{rect}\left(\frac{t}{T_L} - \frac{1}{2} - \ell\right) x_{k',\ell,u} \, \text{e}^{\jmath 2\pi \frac{k(k')(t-T_g)}{T_u}} \tag{5.3}$$

where $T_u = NT$ is the useful symbol duration, $T_g = N_g T$ represents the duration of the cyclic prefix (thus $T_L = T_u + T_g$ is the total symbol duration), and $f_u = 1/T_u$ is the subcarrier spacing.

The SC-FDMA signals from different user are transmitted over a satellite channel, which here we model as AWGN channel. Therefore, taking into account the mentioned effect, as well as the inter-arrival timing offset among the users, the received signal can be written as

$$r(t) = \sum_{u=0}^{U-1} s_u(t - \tau_u T) \, \text{e}^{\jmath\phi(t)} + n(t) \tag{5.4}$$

where τ_u represent the inter-arrival timing offset of the u-th user normalized to sampling time T, $\phi(t)$ represent the phase noise process, $n(t)$ represents a complex Additive White Gaussian Noise (AWGN) random process, with two-sided power spectral density equal to N_0.

At the receiver, after filtering, sampling the received signal every T seconds, and removing the CP, the samples belonging to the ℓ-th SC-FDMA symbol can be written as

$$\begin{aligned} r_{i,\ell} &= r(((\ell - 1)(N + N_g) + N_g + i)T) \\ i &= |u|_{N+N_g} - N_g \qquad \ell = \lceil u/(N + N_g) \rceil \end{aligned} \tag{5.5}$$

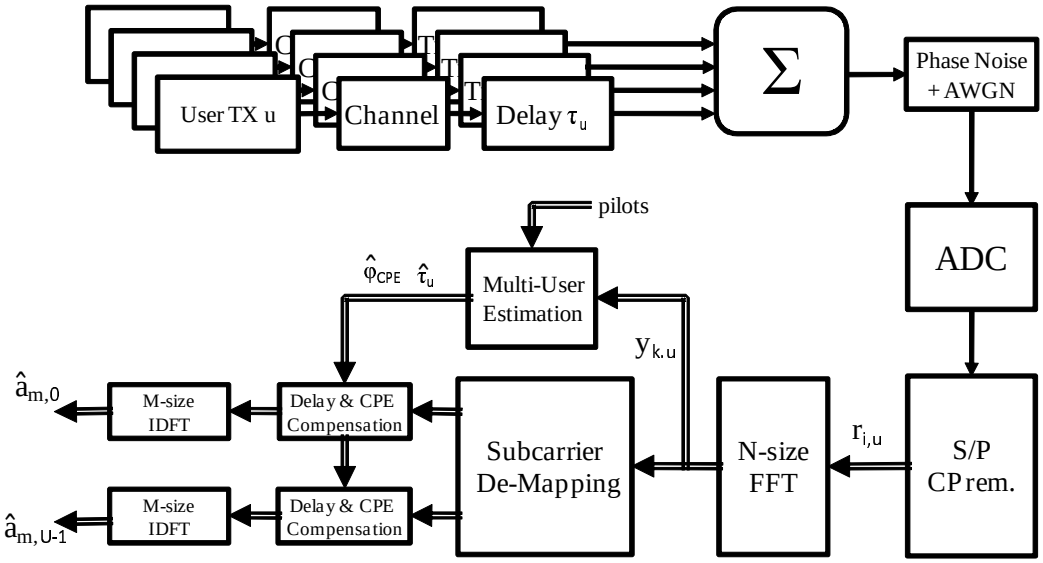

Figure 5.2: Block diagram of the proposed system

At the output of the DFT, the observed samples in the frequency domain are:

$$y_{k,\ell} = \frac{1}{\sqrt{N}} \sum_{i=0}^{N-1} r_{i,\ell}\, \mathrm{e}^{-\jmath\, 2\pi k i/N} \qquad k = 0, \ldots, N-1 \tag{5.6}$$

In [46] and [47] two different effects due to phase noise has been distinguished: first, a CPE which consist in a constant phase rotation of, ϕ^{cpe}, overall the orthogonal subcarriers, and second, a ICI term, d^{ICI}, which can be treated as a growth of the Additive Gaussian Noise. Furthermore, as a consequence of DFT time shift property, the inter-arrival timing offset, even if it is smaller than T_g, causes a phase rotation in the frequency domain of $2\pi k\tau_u/N$. Having assumed that, for all the users τ_u does not exceed CP duration, Eq.(5.6) can be modified in order to incorporate the mentioned effect, yielding:

$$y_{k,\ell,u} = x_{k,\ell,u}\mathrm{e}^{\jmath 2\pi k\tau_u/N}\mathrm{e}^{\jmath\phi^{cpe}} + d^{ICI} + n_{k,\ell,u} \tag{5.7}$$

where $n_{k,\ell}$ is the complex AWGN sample in frequency domain. After having estimated and compensated both ϕ^{cpe} and the vector of inter-arrival timing offset $\bar{\tau} = (\tau_0, \ldots, \tau_{U-1})$, the received data symbols of the u-th are obtained as the M points IDFT of the assigned subcarriers:

$$\hat{a}_{k',\ell,u} = \frac{1}{\sqrt{M}} \sum_{k'=0}^{M-1} y_{k(k'),\ell}\mathrm{e}^{-\jmath\, 2\pi m k'/M} \quad m = 0, \ldots, M-1 \tag{5.8}$$

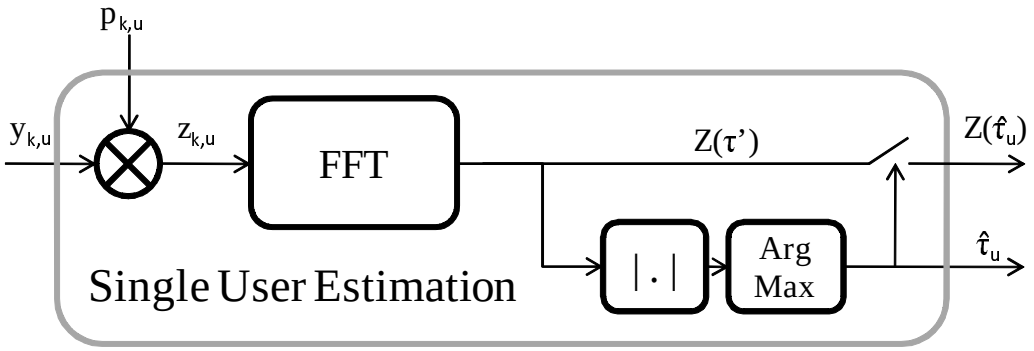

Figure 5.3: Single user estimator

In Figure 5.2 we report the complete block diagram of the proposed SC-FDMA system.

5.2 Joint Multi-User Estimation

In this Section, we present an appropriate design of the pilot tone pattern within the SC-FDMA frame and the proposed joint multi-user estimator.

5.2.1 Pilot Pattern

The complex symbols $a_{k,\ell,u}$ carry either data information, $d_{k,\ell,u}$, or reference tones, $p_{k,\ell,u}$. We chose to gather the pilot tones in a SC-FDMA reference symbol composed only by pilots, and send it every P_s SC-FDMA symbols composed by data. Therefore, we can write

$$a_{k,\ell,u} = \begin{cases} p_{k,\ell,u} & \text{if} \quad \mod(\ell, P_s) = 0 \\ d_{k,\ell,u} & \text{otherwise} \end{cases} \tag{5.9}$$

where $\mod(n, d)$ indicates the remainder of the integer division of n by d. The rationale behind this choice is twofold: first, we can design the SC-FDMA reference symbol in order to keep a low PAPR; second we can use reference tones both before and after the outer DFT. Of course, the higher the density of reference SC-FDMA pilot symbols the easier to track the possible time variation of ϕ^{cpe} and $\bar{\tau}$, but the higher the overhead. To improve synchronization and estimation performance, pilots can be transmitted with energy amplified by a factor β with respect to data symbols (i.e. $E[p^2_{k,\ell,u}] = \beta E_s$, where $E[d^2_{k,\ell,u}] = E_s$).

5.2.2 Timing Offset Estimation

In order estimate the vector $\bar{\tau}$, we exploit the known pilot tones in the frequency domain, i.e. before the outer IDFT, and then we treat this problem as a DA frequency estimation problem in single carrier system. In fact, looking at Eq. (5.6), it is easy to note a strong analogy between this estimation problem and the DA frequency estimation problem in single carrier case. We obtain τ_u estimation as:

$$\hat{\tau}_u = \arg\max_{\tau'} \left| \sum_{k'=0}^{M-1} y_{k',u} x^*_{k'u} \mathrm{e}^{-\jmath 2\pi k(k')\tau'/N} \right| \quad u = 0, \ldots, U-1 \tag{5.10}$$

Where we have considered only the SC-FDMA reference symbols (i.e. $\ell : mod(\ell, P_s) = 0$). Then, for sake of readability, we dropped out the symbol index ℓ, without loss of generality. Using a FFT-Based approach, $\hat{\tau}_u$ can be easily obtained by searching the maximum of the absolute value of part of FFT of the vector $z_{k'u} = y_{k',u} x^*_{k'u}$. Thus,

$$\hat{\tau}_u = \arg\max_{\tau'} |FFT\{z_{k'u}\}| \quad k = 0, \ldots, N-1 \tag{5.11}$$

By enlarging the size of the FFT to N', it is possible to increase the timing resolution of the estimator thus refining estimation results. In general the timing resolution is given by $\frac{N}{N'}T$

5.2.3 CPE Estimation

As anticipated in Section 3.1, the phase rotation ϕ^{cpe} due to phase noise at the receiver is common for all the active subcarriers. Therefore, in order to estimate it, we exploit all the pilot tones composing a SC-FDMA pilot symbol, even if they belong to different users. Similarly to timing estimation, we work in the frequency domain, and we treat this task as a classical DA phase estimation problem. Considering the u-th user, the ML DA phase estimation $\hat{\phi}^{cpe}_u$ is obtained computing the the angle of the cross-correlation $Z_u(\tau_u)$ between the known pilots and the corresponding received tones which has been depurated by the timing offset. In order to adjust the timing offset we use the timing estimates $\hat{\tau}_u$ obtained as illustrated in the previous Section. Hence, ML DA phase estimation is given by:

$$\hat{\phi}^{cpe}_u = \angle\left(Z_u(\hat{\tau}_u)\right) = \angle\left(\sum_{k'=0}^{M-1} y_{k(k'),u} x^*_{k(k'),u} \mathrm{e}^{-\jmath 2\pi \hat{\tau}_u k(k')/N} \right) \tag{5.12}$$

Note that the cross-correlation $Z_u(\hat{\tau}_u)$ coincides with the value of the peak which has been detected in the timing offset estimation for the u-th user, thus it can be

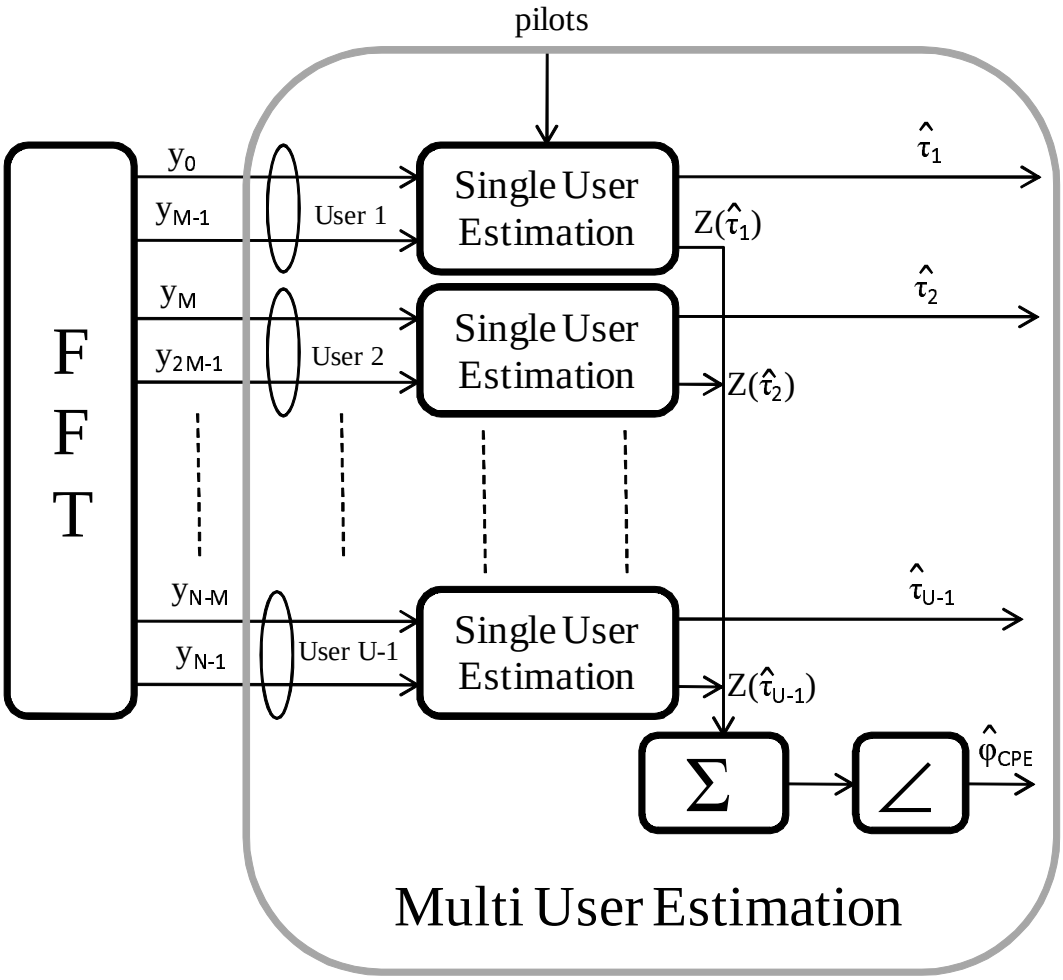

Figure 5.4: Block diagram of the proposed multi user estimator

jointly computed as depicted in Figure 5.3. Since the phase shift ϕ^{cpe} is common for all the users, we can accumulate the single user estimates obtaining a more accurate estimation. In this manner, we obtain a the Multi-user ML DA estimator which is given by:

$$\hat{\phi}_{cpe} = \angle \left(\sum_{u=0}^{U-1} Z_u(\tau_u) \right) \tag{5.13}$$

In Figure 5.4 we report a complete block diagram of the JMU Estimator.

5.3 Numerical Results

In this Section we present the numerical result in terms of Mean Square Error (MSE) of the considered estimators and of un-coded Bit Error Rate (BER) of the end-to-end system. In order to highlight the role of some important parameters such as the sub carrier spacing we consider two different SC-FDMA configuration which are summarized in Table 5.1.

In the Monte Carlo simulations used to evaluate the performance we consider a realistic PNM, reported in Figure 3.1, which has been defined during the RCS Call-for-Technology and mentioned in Section 3.1. The timing offset inserted in the simulation chain has been assumed independent among different users and uniformly distributed between zero and the CP duration (i.,e. $\tau_u \sim U[0, N_g]$ i.i.d. $\forall u = 0, \ldots, U-1$). Moreover we consider the proposed pilot patter with parameters $\beta = 2$ and $P_s = 10$. It has been previously shown in [46], [47], that, the overall phase noise degradation does not depend on the number of subcarriers nor on the phase noise bandwidth. However if we try to compensate the CPE, this does not hold true. For example, if the subcarrier spacing is larger enough than the phase noise bandwidth, then the CPE component dominates over the ICI component. Since, the degradation due to CPE can be compensated, the performance degradation will be smaller. On the other hand, if the subcarrier spacing is comparable with the phase noise bandwidth, then the ICI component becomes significant, and the correction capabilities decrease. As a consequence, the performance leakage will be larger.

In Figure 5.5 we show the performance of timing estimation for all the considered configurations. Of course the higher the number of pilot tones the best the estimation performance. Indeed cases 2A, 2B, 2C, outperform cases 1A, 1B, 1C

Table 5.1: Considered SC-FDMA configuration parameters

Case	1A	1B	1C	2A	2B	2C
T [ns]	31.25					
B [MHz]	32					
M	8			16		
N	64	128	256	64	128	256
U	8	16	32	4	8	16
f_u [kHz]	500	250	128	500	250	128

respectively. Considering the same number of pilots, the case with $N = 64$ has better performance because the ICI due to phase noise is smaller than other cases. The CPE estimation performance is reported in Figure 5.6. Considering the case of Ideal Timing Estimation (ITE), the numerical results show that the higher the number of subcarriers, the better the CPE Estimation performance. In fact case C outperforms case B and A. However, we notice that this estimation is particularly sensible to the residual errors of timing offset. In fact, considering a non-ideal timing estimation, case A outperforms the other cases. This is because its residual timing error is smaller compared with the other cases.

In Figure 5.7 we report the uncoded BER performance considering QPSK modulation. As a benchmark we also report QPSK performance in AWGN, with ideal estimation and without phase noise. We notice that the Case 2A has the best performance. In this case the performance gap with respect to the AWGN can be considered negligible. Using $M = 8$ the performance decreases considerably. Again, this is caused by the higher residual error of both timing and the phase estimation. The uncoded BER performance for 16QAM modulation has been reported in Figure 5.8. As above, we report as a benchmark 16QAM performance in ideal AWGN case. Numerical results show that case 1A 2A and 2B reach the best performance, showing a gap of less than 1 dB at BER=10^{-2} with respect to the AWGN case. Again the configurations with $N = 256$ have the worst performance.

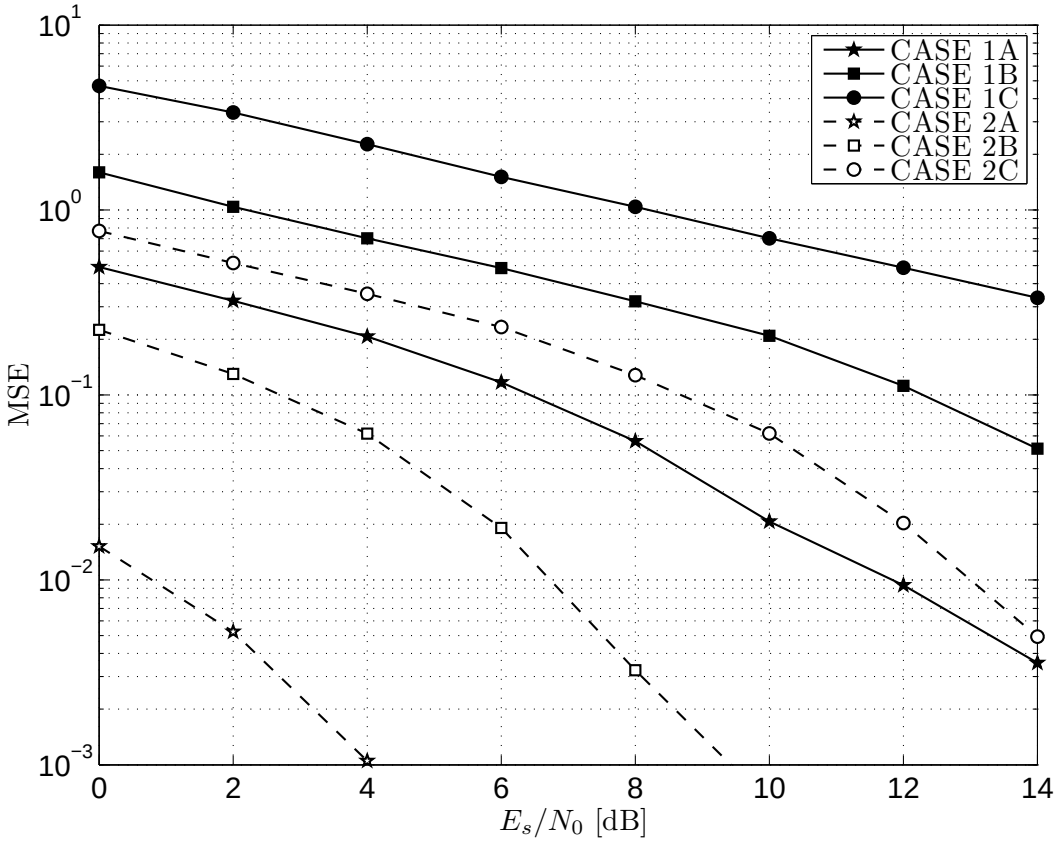

Figure 5.5: Timing Estimation performance

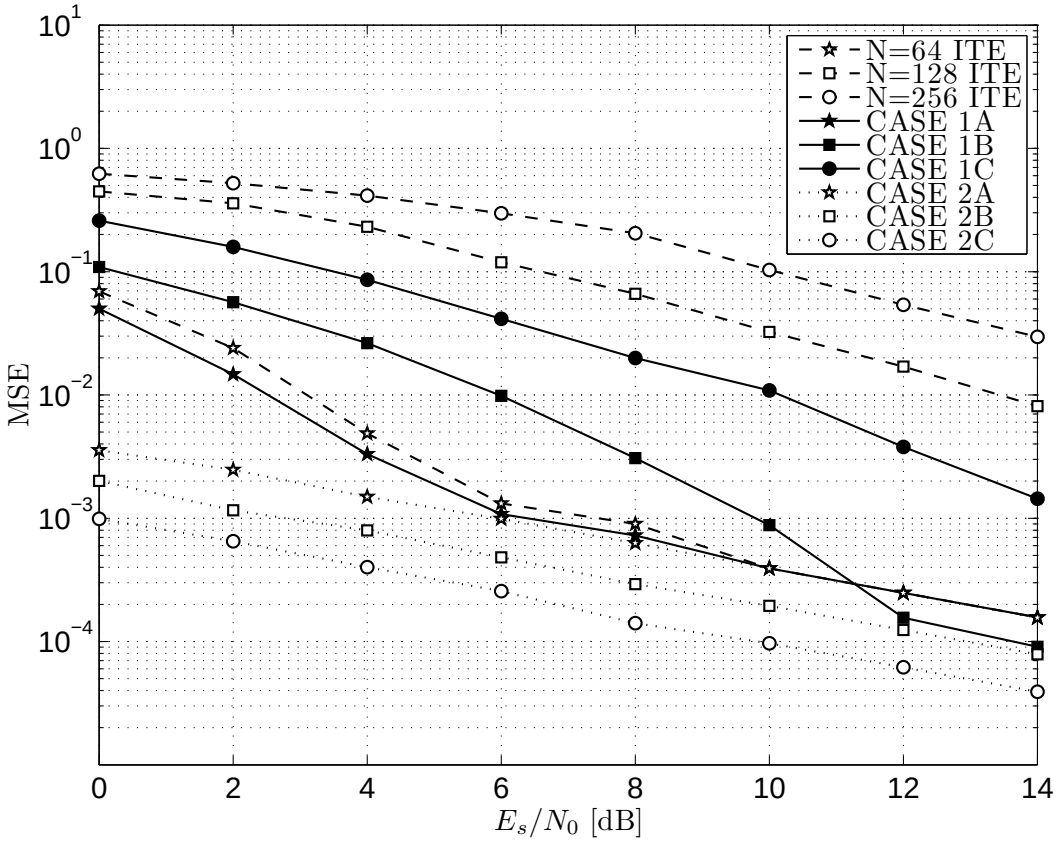

Figure 5.6: CPE Estimation performance

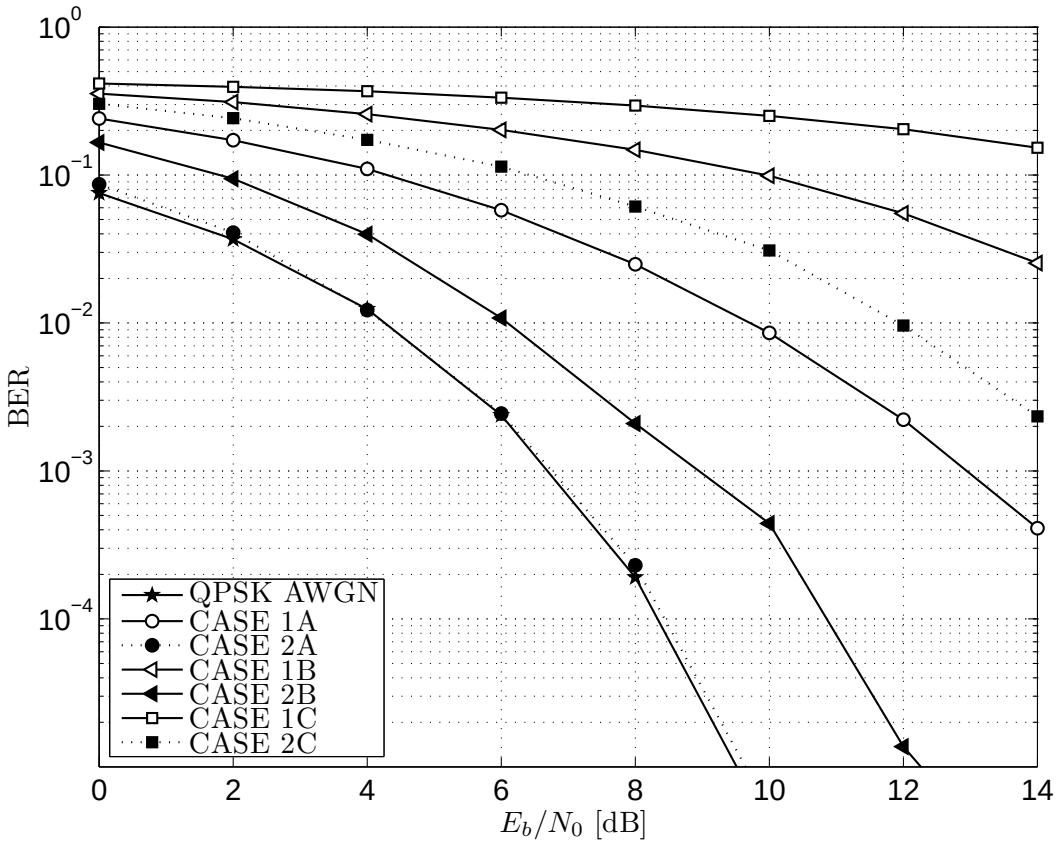

Figure 5.7: QPSK BER performance

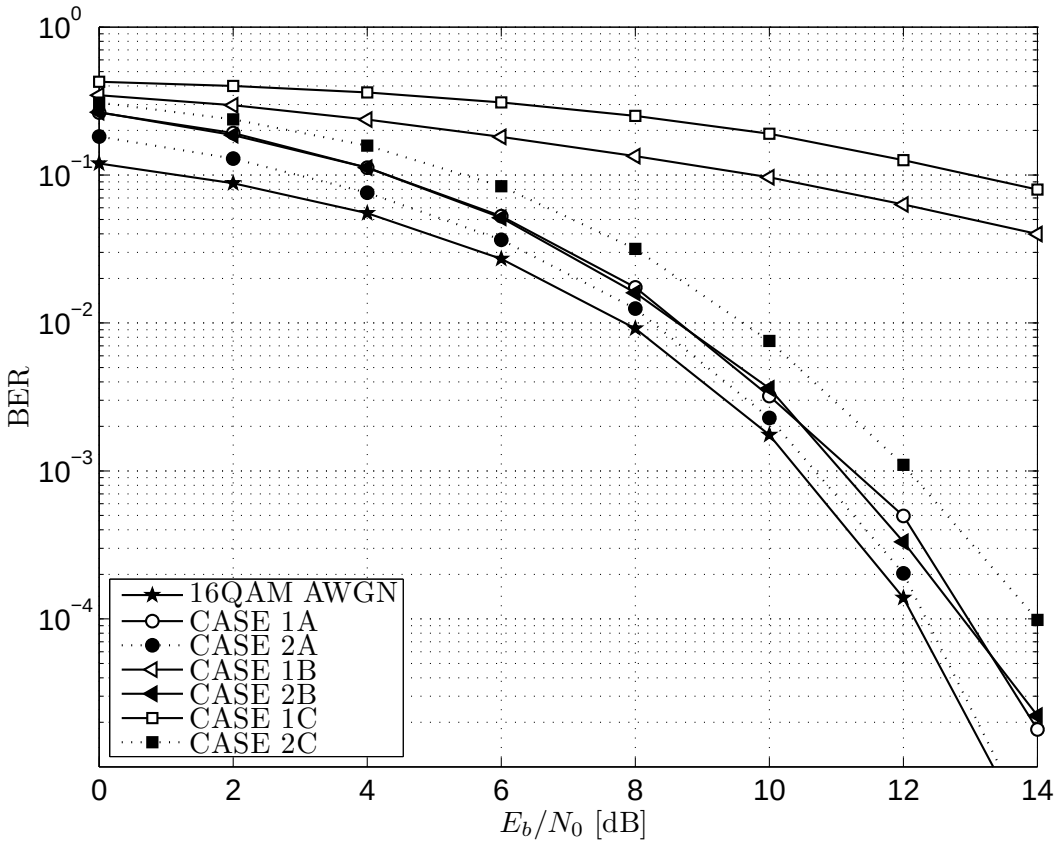

Figure 5.8: 16QAM BER performance

BIBLIOGRAPHY

[1] L. Cimini, "Analysis and Simulation of a Digital Mobile Channel Using Orthogonal Frequency Division Multiplexing," *Communications, IEEE Transactions on [legacy, pre - 1988]*, vol. 33, no. 7, pp. 665–675, 1985.

[2] J. A. C. Bingham, "Multicarrier modulation for data transmission: an idea whose time has come," *Communications Magazine, IEEE*, vol. 28, no. 5, pp. 5–14, 1990.

[3] E. Biglieri, J. Proakis, and S. Shamai, "Fading channels: information-theoretic and communications aspects," *Information Theory, IEEE Transactions on*, vol. 44, no. 6, pp. 2619–2692, 1998.

[4] B. Sklar, "Rayleigh fading channels in mobile digital communication systems .i. characterization," *Communications Magazine, IEEE*, vol. 35, no. 7, pp. 90 –100, Jul. 1997.

[5] S. Weinstein and P. Ebert, "Data Transmission by Frequency-Division Multiplexing Using the Discrete Fourier Transform," *Communications, IEEE Transactions on*, vol. 19, no. 5, pp. 628–634, October 1971.

[6] B. Muquet, Z. Wang, G. Giannakis, M. de Courville, and P. Duhamel, "Cyclic prefixing or zero padding for wireless multicarrier transmissions?" *Communications, IEEE Transactions on*, vol. 50, no. 12, pp. 2136 – 2148, Dec. 2002.

[7] A. Vahlin and N. Holte, "Optimal finite duration pulses for ofdm," *Communications, IEEE Transactions on*, vol. 44, no. 1, pp. 10 –14, Jan. 1996.

[8] N. Baas and D. Taylor, "Pulse shaping for wireless communication over time- or frequency-selective channels," *Communications, IEEE Transactions on*, vol. 52, no. 9, pp. 1477 – 1479, 2004.

[9] P. Siohan and C. Roche, "Cosine-modulated filterbanks based on extended gaussian functions," *Signal Processing, IEEE Transactions on*, vol. 48, no. 11, pp. 3052 –3061, Nov. 2000.

[10] ——, "Derivation of extended gaussian functions based on the zak transform," *Signal Processing Letters, IEEE*, vol. 11, no. 3, pp. 401 – 403, 2004.

[11] M. Speth, S. A. Fechtel, G. Fock, and H. Meyr, "Optimum receiver design for wireless broad-band systems using OFDM. I," *Communications, IEEE Transactions on*, vol. 47, no. 11, pp. 1668–1677, Nov 1999.

[12] D. Tse and P. Viswanath, *Fundamentals of wireless communication*. New York, NY, USA: Cambridge University Press, 2005.

[13] J. J. Bussgang, "Crosscorrelation functions of amplitude-distorted gaussian signals," *Research Laboratory of Electronics, Massachusetts Institute of Technology Technical Report*, 1952.

[14] J. Minkoff, "The role of am-to-pm conversion in memoryless nonlinear systems," *Communications, IEEE Transactions on*, vol. 33, no. 2, pp. 139 – 144, Feb. 1985.

[15] D. Dardari, V. Tralli, and A. Vaccari, "A theoretical characterization of nonlinear distortion effects in OFDM systems," *Communications, IEEE Transactions on*, vol. 48, no. 10, pp. 1755 – 1764, Oct. 2000.

[16] P. Banelli and S. Cacopardi, "Theoretical analysis and performance of OFDM signals in nonlinear awgn channels," *Communications, IEEE Transactions on*, vol. 48, no. 3, pp. 430 –441, Mar. 2000.

[17] P. Banelli, "Theoretical analysis and performance of OFDM signals in nonlinear fading channels," *Wireless Communications, IEEE Transactions on*, vol. 2, no. 2, pp. 284 – 293, Mar. 2003.

[18] H. Ochiai and H. Imai, "Performance of the deliberate clipping with adaptive symbol selection for strictly band-limited OFDM systems," *Selected Areas in Communications, IEEE Journal on*, vol. 18, no. 11, pp. 2270 –2277, Nov. 2000.

[19] "Digital Video Broadcasting (DVB) Second generation framing structure, channel coding and modulation systems for Broadcasting, Interactive Services, News Gathering and other broadband satellite applications (DVB-S2)," no. ETSI EN 302 307 v1.1.1, Jan. 2004.

[20] "Digital Video Broadcasting (DVB); Framing structure, channel coding and modulation for satellite transmission to handheld. (DVB-SH)," no. ETSI EN 302 583, 2007.

[21] "Digital Video Broadcasting (DVB); Transmission System for Handheld Terminals. (DVB-H)," no. ETSI EN 302 583, 2004.

[22] "Digital Video Broadcasting (DVB); Interaction channel for satellite distribution systems (DVB-RCS)," no. ETSI EN 301 790, May 2009.

[23] S. Rosati, S. Cioni, A. Vanelli-Coralli, G. Corazza, G. Gallinaro, and A. Ginesi, "A joint multi-user synchronization method for sc-fdma in broadband satellite return channel," in *GLOBECOM 2010, 2010 IEEE Global Telecommunications Conference*, 2010.

[24] S. Rosati, E. Candreva, and G. Corazza, "Rotation invariant subcarrier mapping: A novel technique enabling quasi-constant OFDM envelope," in *Advanced satellite multimedia systems conference (ASMS) and the 11th signal processing for space communications workshop (SPSC), 2010 5th*, 2010, pp. 436 –443.

[25] P. Zillmann and G. Fettweis, "On the capacity of multicarrier transmission over nonlinear channels," in *Vehicular Technology Conference, 2005. VTC 2005-Spring. 2005 IEEE 61st*, 2005.

[26] A. Saleh, "Frequency-independent and frequency-dependent nonlinear models of twt amplifiers," *Communications, IEEE Transactions on*, vol. 29, no. 11, pp. 1715 – 1720, Nov. 1981.

[27] C. Rapp, "Effects of HPA-nonlinearity on a 4-DPSK/OFDM-signal for a digital sound broadcasting signal," in *ESA Special Publication*, ser. ESA Special Publication, P. S. Weltevreden, Ed., vol. 332, Oct. 1991, pp. 179–184.

[28] P. Salmi, M. Neri, and G. E. Corazza, "Design and performance of predistortion techniques in ka-band satellite networks," in *Proceedings of 22nd AIAA ICSSC-2004*, May 2004.

[29] J. Qiu, D. Abe, J. Antonsen, T.M., B. Danly, B. Levush, and R. Myers, "Linearizability of twtas using predistortion techniques," *Electron Devices, IEEE Transactions on*, vol. 52, no. 5, pp. 718 – 727, May 2005.

[30] J. Kim, C. Park, J. Moon, and B. Kim, "Analysis of adaptive digital feedback linearization techniques," *Circuits and Systems I: Regular Papers, IEEE Transactions on*, vol. 57, no. 2, pp. 345 –354, 2010.

[31] G. E. Corazza, *Digital Satellite Communications*. Springer, New York, NY, 2007.

[32] S. H. Han and J. H. Lee, "An overview of peak-to-average power ratio reduction techniques for multicarrier transmission," *Wireless Communications, IEEE*, vol. 12, no. 2, pp. 56 – 65, 2005.

[33] T. Jiang and Y. Wu, "An overview: Peak-to-average power ratio reduction techniques for OFDM signals," *Broadcasting, IEEE Transactions on*, vol. 54, no. 2, pp. 257 –268, 2008.

[34] B. Krongrold and D. Jones, "PAR reduction in OFDM via active constellation extension," vol. 49, no. 3, pp. 258–268, Sep. 2003.

[35] J. Tellado, "Peak to average power reduction for multicarrier modulation," Ph.D. dissertation, Stanford University, Stanford, CA, USA, 2000.

[36] B. Krongrold and D. Jones, "An active set approach for OFDM PAR reduction via tone reservation," vol. 52, no. 2, pp. 495–509, Feb. 2004.

[37] R. Bäuml, R. Fischer, and J. Huber, "Reducing the peak-to-average power ratio of multicarrier modulation by selected mapping," *Electr. Lett.*, vol. 32, no. 22, pp. 2056–2057, Oct. 1996.

[38] M. Breiling, S. M uller-Weinfurtner, and J. Huber, "Sml peak-power reduction without explicit side information," vol. 5, no. 6, pp. 239–241, Jun. 2001.

[39] M. Abramowitz and I. A. Stegun, *Handbook of Mathematical Functions with Formulas, Graphs, and Mathematical Tables*, ninth dover printing, tenth gpo printing ed. New York: Dover, 1964.

[40] S. Rosati, E. Candreva, and G. Corazza, "Study group report TM-NGH685 (DVB-NGH)," 2011.

[41] ——, "Study group report M-NGH764r1 (DVB-NGH)," 2011.

[42] E. Casini, R. D. Gaudenzi, and A. Ginesi, "Dvb-s2 modem algorithms design and performance over typical satellite channels," *International Journal of Satellite Communications and Networking*, vol. 22, no. 3, pp. 281–318, 2004.

[43] "Study group report TM-RCS1143 (DVB-RCS)," 2010.

[44] R. Scholtz, "Frame synchronization techniques," *Communications, IEEE Transactions on*, vol. 28, no. 8, pp. 1204 – 1213, aug 1980.

[45] W. P. Robins and I. of Electrical Engineers., *Phase noise in signal sources : (theory and applications) / W.P. Robins*. Peregrinus on behalf of the Institution of Electrical Engineers, London, UK. :, 1982.

[46] L. Tomba, "On the effect of wiener phase noise in OFDM systems," *Communications, IEEE Transactions on*, vol. 46, no. 5, pp. 580 –583, May 1998.

[47] A. Armada and M. Calvo, "Phase noise and sub-carrier spacing effects on the performance of an OFDM communication system," *Communications Letters, IEEE*, vol. 2, no. 1, pp. 11 –13, Jan. 1998.

[48] L. Schwoerer and J. Vesma, "Fast scattered pilot synchronization for dvb-t and dvb-h," in *8th International OFDM Workshop,*, 2003.

[49] J. J. van de Beek, M. Sandell, and P. O. Borjesson, "ML estimation of time and frequency offset in OFDM systems," *Signal Processing, IEEE Transactions on [see also Acoustics, Speech, and Signal Processing, IEEE Transactions on]*, vol. 45, no. 7, pp. 1800–1805, 1997.

[50] T. Keller and L. Hanzo, "Orthogonal frequency division multiplex synchronisation techniques for wireless local area networks," *Personal, Indoor and Mobile Radio Communications, 1996. PIMRC'96., Seventh IEEE International Symposium on*, vol. 3, pp. 963–967 vol.3, 1996.

[51] M. Speth, F. Classen, and H. Meyr, "Frame synchronization of OFDM systems in frequency selective fading channels," in *Vehicular Technology Conference, 1997 IEEE 47th*, vol. 3, 1997, pp. 1807–1811 vol.3.

[52] A. Palin and J. Rinne, "Enhanced symbol synchronization method for OFDM system in sfn channels," in *Global Telecommunications Conference, 1998. GLOBECOM 98. The Bridge to Global Integration. IEEE*, 1998.

[53] M.-H. Hsieh and C.-H. Wei, "A low-complexity frame synchronization and frequency offset compensation scheme for OFDM systems over fading channels," *Vehicular Technology, IEEE Transactions on*, vol. 48, no. 5, pp. 1596–1609, 1999.

[54] H. Zheng, J. Tang, and B. Shen, "Low-complexity joint synchronization of symbol timing and carrier frequency for OFDM systems," *Consumer Electronics, IEEE Transactions on*, vol. 51, no. 3, pp. 783 – 789, 2005.

[55] S. Rosati, S. Cioni, M. Neri, A. Vanelli-Coralli, and G. Corazza, "Joint symbol timing and carrier frequency recovery for dvb-sh system," in *Satellite and Space Communications, 2007. IWSSC '07. International Workshop on*, 2007, pp. 79 –83.

[56] F. Bastia, C. Palestini, S. Rosati, M. Neri, and G. Corazza, "Preamble insertion in future satellite-terrestrial OFDM mobile broadcasting standards," *IET Conference Publications*, vol. 2009, no. CP552, pp. 223–223, 2009.

[57] S. Patel, J. Cimini, L.J., and B. McNair, "Comparison of frequency offset estimation techniques for burst ofdm," in *Vehicular Technology Conference, 2002. VTC Spring 2002. IEEE 55th*, 2002.

[58] M. Speth, S. Fechtel, G. Fock, and H. Meyr, "Optimum receiver design for OFDM-based broadband transmission .II. A case study," *Communications, IEEE Transactions on*, vol. 49, no. 4, pp. 571–578, April 2001.

[59] ——, "Broadband transmission using ofdm: system performance and receiver complexity," in *Broadband Communications, 1998. Accessing, Transmission, Networking. Proceedings. 1998 International Zurich Seminar on*, Feb. 1998, pp. 99 – 104.

[60] S. Rosati, M. Villanti, A. Vanelli-Coralli, and G. E. Corazza, "OFDM post-fft frequency recovery based on silent sub-carriers," in *Spread Spectrum Techniques and Applications, 2008. ISSSTA '08. IEEE 10th International Symposium on*, 2008, pp. 452 –457.

[61] M. Villanti, M. Iubatti, A. Vanelli-Coralli, and G. Corazza, "Design of distributed unique words for enhanced frame synchronization," *Communications, IEEE Transactions on*, vol. 57, no. 8, pp. 2430 –2440, 2009.

[62] ——, "Frame synchronization at the sound of silence," in *Global Telecommunications Conference, 2005. GLOBECOM '05. IEEE*, 2005.

[63] M. Ghogho, A. Swami, and G. Giannakis, "Optimized null-subcarrier selection for cfo estimation in OFDM over frequency-selective fading channels," in *Global Telecommunications Conference, 2001. GLOBECOM '01. IEEE*, 2001.

[64] P. Hoeher, S. Kaiser, and P. Robertson, "Two-dimensional pilot-symbol-aided channel estimation by wiener filtering," in *Acoustics, Speech, and Signal Processing, 1997. ICASSP-97., 1997 IEEE International Conference on*, vol. 3, Apr. 1997, pp. 1845 –1848 vol.3.

[65] ——, *Pilot-symbol-aided channel estimation in time and frequency*. Norwell, MA, USA: Kluwer Academic Publishers, 1997, pp. 169–178.

[66] Y. G. Li, J. Cimini, L.J., and N. Sollenberger, "Robust channel estimation for OFDM systems with rapid dispersive fading channels," in *Communications, 1998. ICC 98. Conference Record.1998 IEEE International Conference on*, vol. 3, Jun. 1998, pp. 1320 –1324 vol.3.

[67] O. Edfors, M. Sandell, J.-J. van de Beek, S. Wilson, and P. Borjesson, "OFDM channel estimation by singular value decomposition," *Communications, IEEE Transactions on*, vol. 46, no. 7, pp. 931 –939, Jul. 1998.

[68] O. Edfors, M. Sandell, J.-J. Van De Beek, S. K. Wilson, and P. O. Börjesson, "Analysis of dft-based channel estimators for ofdm," *Wirel. Pers. Commun.*, vol. 12, pp. 55–70, January 2000.

[69] M. Morelli and U. Mengali, "A comparison of pilot-aided channel estimation methods for OFDM systems," *Signal Processing, IEEE Transactions on*, vol. 49, no. 12, pp. 3065 –3073, Dec. 2001.

[70] H. Minn and V. Bhargava, "An investigation into time-domain approach for OFDM channel estimation," *Broadcasting, IEEE Transactions on*, vol. 46, no. 4, pp. 240 –248, Dec. 2000.

[71] Y. Kang, K. Kim, and H. Park, "Efficient dft-based channel estimation for OFDM systems on multipath channels," *Communications, IET*, vol. 1, no. 2, pp. 197 –202, 2007.

[72] J. Oliver, R. Aravind, and K. Prabhu, "Sparse channel estimation in OFDM systems by threshold-based pruning," *Electronics Letters*, vol. 44, no. 13, pp. 830 –832, 19 2008.

[73] S. Rosati, G. Corazza, and A. Vanelli-Coralli, "OFDM channel estimation with optimal threshold-based selection of cir samples," in *Global Telecommunications Conference, 2009. GLOBECOM 2009. IEEE*, 30 2009.

[74] S. Rosati, A. Awoseyila, A. Vanelli-Coralli, C. Kasparis, G. Corazza, and B. Evans, "Threshold detection analysis for OFDM timing and frequency recovery," in *Global Telecommunications Conference, 2009. GLOBECOM 2009. IEEE*, 30 2009.

[75] G. Corazza and R. De Gaudenzi, "Analysis of coded noncoherent transmission in ds-cdma mobile satellite communications," *Communications, IEEE Transactions on*, vol. 46, no. 11, pp. 1525 –1535, Nov. 1998.

[76] R. Negi and J. Cioffi, "Pilot tone selection for channel estimation in a mobile OFDM system," *Consumer Electronics, IEEE Transactions on*, vol. 44, no. 3, pp. 1122 –1128, Aug. 1998.

[77] F. Bastia, C. Bersani, E. A. Candreva, S. Cioni, G. E. Corazza, M. Neri, C. Palestini, M. Papaleo, S. Rosati, and A. Vanelli-Coralli, "Lte adaptation for mobile broadband satellite networks," *EURASIP J. Wirel. Commun. Netw.*, vol. 2009, pp. 12:7–12:7, March 2009.

[78] H. G. Myung, J. Lim, and D. J. Goodman, "Single carrier fdma for uplink wireless transmission," *Vehicular Technology Magazine, IEEE*, vol. 1, no. 3, pp. 30 –38, 2006.